The University of Nottingham

UNITED KINGDOM · CHINA · MALAYSIA

Behaviours of Droplets Interaction with Solid Surfaces and Thermal Performance of a Pulsating Heat Pipe

Xin Wang

Thesis submitted to the University of Nottingham for the degree of Doctor of Philosophy

September 2022

Abstract

Over the past few decades, liquid drops and droplets are the ubiquitous in nature， which have attracted many investigations' attention. Droplets interaction with solid surface plays a crucial role in many industrial applications, such as inkjet printing, spraying cooling, biosensors, DNA microarrays, Nanotechnology, and so on. However, the behaviours of droplets interaction with solid surfaces are unexpected, resulting in adverse or beneficial effects for these applications. Therefore, a large amount of literature focuses on exploring the mechanism behind this phenomenon and finding effective strategies to control it. This study aims to explore how to control the distribution of deposition patterns with various strategies and advance the understanding of the droplet impact behaviours on the surface with different roughness and substrate morphology. In this dissertation, the study of the behaviours of droplets interaction with solid surfaces is divided into two parts. Firstly, the evaporation process and deposition patterns of a saline droplet on a copper substrate have been experimentally studied by adjusting the surface roughness and substrate temperature. The experimental results show that the coffee ring effect is suppressed by increasing substrate roughness, and the deposited patterns transit from uniformity, ring-like structure to dual ring patterns with substrate temperature increasing. Secondly, the dynamic behaviours of droplet impact on a conical structure with different cone angles and surface roughness have been experimentally investigated with the help of a high-speed camera. The experimental results show that the maximum spreading factor β_{max} increases as the Weber number increases and the increase in the surface roughness and cone angle reduces the β_{max}. In

addition, the splashing can be promoted by increased the surface roughness and cone angle, which is characterized by critical Weber number We_{cr}.

The investigation of the thermal performance of a closed loop pulsating heat pipe(CLPHP) is also conducted. Nowadays, the energy crisis and serious environmental pollution are threatening people all over the world. Efficient energy management is one of the feasible methods to solve the existing energy crisis and has attracted extensive attention. Pulsating heat pipe (PHP), as a potential thermal management system, has great potential in application due to its simple structure, low cost and excellent heat transfer performance. The thermal performance of the PHP is affected by many factors. Although there are many investigations are carried out to understand the effects of various factors on the thermal performance of the PHP, the optimal conditions have not been found. This section devotes to experimentally explore the strategy of enhancing the thermal performance of PHPs and further reveal the working mechanism of PHPs. The experiments are conducted using a glass PHP with micro encapsulated phase change material suspension(MEPCMS). The micro encapsulated phase change material suspension(MEPCMS) is selected for the working fluids containing microencapsulated phase change materials. The results show that the thermal performance of PHP can be enhanced by applying the MEPCMS working fluid dependent on the filling ratio and concentration of the working fluid. Increasing the filling ratio not only improves the maximum heat transfer capacity of PHP but also enhances the requirement of driving force which limits the thermal performance of the PHP. With the increasing concentration of working fluid, the heat transfer capacity also can be enhanced while increasing the viscosity of the working fluid which hinders the motion of the working fluid. Therefore, the influence of filling ratio and concentration on the PHP should consider the combined effect of passive effect and negative effect of them. The best thermal performance is 0.37°C/W when the filling ratio, input power, and concentration of the MEPCMS are 40%, 90W, and 4wt% in this study.

List of Publications

[1] **Wang, X**., Liu, Z., Wang, L., Yan, Y., Investigation of Droplet Evaporation on Copper Substrate with Different Roughness, Journal of Bionic Engineering, 2020, 17(4), pp. 835–842.

[2] Liu, Z., **Wang, X**. Yan, Y., Xinyong Chen, "Thermal strategies for controlling droplet deposition patterns", UK heat transfer conference 2019, Nottingham, UK.

[3] Chen, Y., Li, B., **Wang, X**., ...Qi, F., Li, H., Direct Phase-Change Cooling of Vapor Chamber Integrated with IGBT Power Electronic Module for Automotive Application, IEEE Transactions on Power Electronics, 2021, 36(5), pp. 5736–5747, 9225695.

[4] Chen, Y., Li, B., **Wang, X**., ...Wang, Y., Qi, F., Investigation of heat transfer and thermal stresses of novel thermal management system integrated with vapour chamber for IGBT power module, Thermal Science and Engineering Progress, 2019, 10, pp. 73–81.

Acknowledgement

First of all, I would like to express my sincere gratitude to my supervisor, Professor Yuying Yan, for his invaluable support, advice, and patient guidance throughout my 4 years of PhD study.

I would like to sincerely thank our technical staff of Built Environment Department and Pharmacy Department. Thanks to Mr. Tony Gospel, Mr. Andrew Matthews, Mr. Daniel Copper, and Mr. James Hazzledine for their professional advice and assistance with my laboratory work.

I would also like to express my gratitude to my colleagues Dr. Yiyi Chen, Dr. Kuo Huang, Dr. Wei Gong, Mr. Thomas Werner, Mr. Edward Wright, Mr. Li Wang, Mr. Dahui Yu, and Mr. Shuai Zhang. Thanks for their continuous support and unforgettable memories during my studying in Nottingham. Especially, I would like to thank Dr. Xuehui Wang for his kind help and guidance in the design of the experiment.

I also want to thank my friends who live in Nottingham for their kind help.

Finally, my deepest gratitude to my parents for their endless support and encouragement. Without their continuous love, I could not complete the thesis and I would be grateful for them forever.

Table of Content

Nomenclature

Symbols

θ_Y	apparent contact angle
σ_{SV}	interfacial tensions for the solid–vapor
σ_{Sl}	interfacial tensions for the solid–liquid
σ_{lv}	interfacial tensions for the liquid–vapor
St/Sa	roughness ratio
St	true area of the solid surface

Sa	the apparent area
θ_{rough}	contact angle on a rough surface
θ_{smooth}	contact angle on a smooth surface
σ_1	interface area fraction of the solid substrate
R_a	Rayleigh number
l	length
v	kinematic viscosity
g	acceleration due to gravity
α	thermal diffusivity
β	coefficient of thermal expansion
T_s	surface temperature
T_∞	ambient temperature
η	dynamic viscosity
ρ	liquid density
C	concentration
β_{max}	maximum spreading factor
D_{max}	diameter of the final lamella at the surface
D_0	droplet initial diameter
We	Weber number

Re	Reynolds number
Oh	Ohnesorge number
μ	viscosity
σ	surface tension
V_0	impact velocity
h_0	thickness of the pre-existing liquid film
R_{max}	maximum spreading radius
V_t	tangential impact velocity
Ca	critical capillary number
$K_{splashing}$	splashing parameter
R_{pk}	average height of protruding peaks above roughness core profile
R_{sm}	mean width of a profile element
R_a	surface roughness parameter
h	height between the syringe and cone tip
t	time
R_{eq}	equilibrium spreading diameter
We_{cr}	critical Weber number
D_{tube}	acceptable diameter of capillary tube

D_{crit}	critical diameter
ρ_{liq}	densities of working fluid at liquid phase
ρ_{vap}	densities of working fluid at vapor phase
R_{th}	thermal resistance
T_e	average temperature of the evaporation section
T_c	average temperature of the condensation section
Q	heat input
T_i	average temperature from thermocouple measuring point i of the PHP
ρ_1	density of DI water
ρ_2	density of test sample
μ_1	viscosity of water
μ_2	viscosity of test sample

Abbreviations

PHP	pulsating heat pipe
MEPCMS	micro encapsulated phase change material suspension
TPLC	Triple-Phase Contact Lines

CCR	Constant Contact Radius
CCA	Constant Contact Angle
CRE	coffee-ring effect
CAH	Contact Angle Hysteresis
DI	Deionized
HSA	human serum albumin
SDS	sodium dodecyl sulfate
CTAB	cetyltrimethylammonium bromide
CLPHP	closed loop pulsating heat pipe
FR	filling ratio

List of Figures

List of Tables

Chapter 1 Introduction

1.1 General background

Over the past few decades, liquid drops and droplets are the ubiquitous phenomena occurring in nature. Theses phenomena attracted many investigations' attention. It can be not only observed in nature, such as spilled coffee on the desk or rain droplets on the lotus, but also applied to different industrial applications, like inkjet printing [1], spray cooling [2], biosensor [3], DNA microarrays[4], Nanotechnology [5-6] and so on. However, the behaviours of droplets interaction with solid surfaces are an unexpected result in adverse or beneficial effects for these applications. Therefore, a great number of studies have been carried out to understand and control this process. This work aims to extend the understanding of behaviours of droplets interaction with solid surfaces and provide fundamental support for the relevant applications. Two behaviours are focused on in this work, they are droplet evaporation and droplet impingement. The coffee ring effect is one of the sub-sections of droplet evaporation, which is deposited by non-volatile solute of liquid after evaporation and was firstly proposed by Deegan et al. [7-8]. This effect should be firstly illustrated to understand the formation of deposition patterns because it widely occurs in industrial and practical applications, such as inkjet printing, polymer coating, micro/nanotechnology, biomedical analysis, and diagnosis. Over the past decades, deposition pattern formation has attracted much attention, which has encouraged many investigations to contribute to understanding and to control the distribution of deposition pattern formations by different influencing factors such as droplet properties, substrate properties, ambient conditions, and particle size.

Droplet impingement is one ubiquitous phenomenon widely existing in nature, which has similar practical applications to droplet evaporation such as ink-jet printing [9] and spray cooling [10]. The droplets impact on solid and liquid surfaces are a common phenomenon that occurs in daily technical applications, such as ink-jet printing, spray cooling of hot surface incinerators, surface coating[11] and 3D printing[12]. These impacts were started to investigate in the early 20th century. In 1908, Worthington [13] investigated the impact of a droplet and solid-ball on deep liquid pools, and many photographs accompanying this phenomenon were contained in his book as Figure 1-1 shown. Although the impact is common, the phenomenon is still not fully understood over 100 years of research and continue to attract investigations to study this topic.

a b

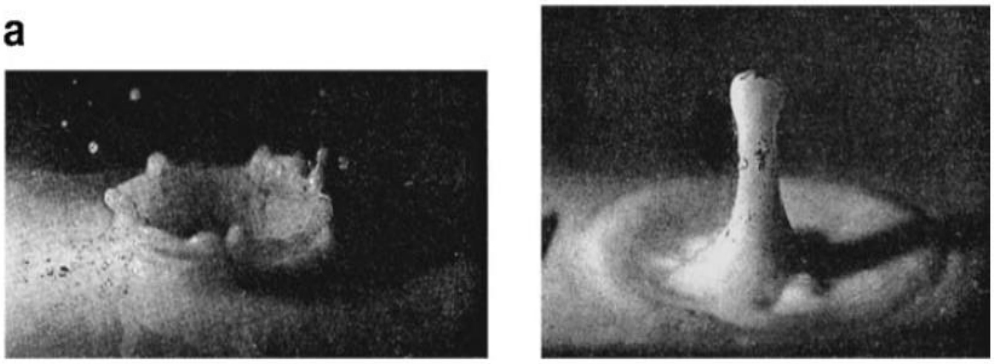

Figure 1-1 water droplet impact on a deep pool of milk mixed with water (Worthington)[13]

The accompanying phenomena shows an extreme variety, complexity, and unexpected behaviours. The behaviours are affected by plenty of factors. During the impact process, the droplet can be changed to spherical or elliptic shape. For the impacted target, the impact can be happened on a dry solid surface, on the free surface of a liquid deep pool, in the air, or in vacuum. The place can be perpendicular or oblique. The liquid droplet can be mixed with the pool/film(miscible) or not dissolve in the pool/film(immiscible). The solid surface can have different properties, it can be hydrophilic or hydrophobic, porous, flat or curved. The droplet spreading, receding, and rebounding happens when the droplet impacts the solid surface. The crown formation, propagation breakup, and bubble trapping can be observed when the droplet impacts a liquid film.

Therefore, the result of droplet impact can be influenced by the impact velocity, solid surface property (roughness and wettability), the properties of the liquid (density, viscosity), thermal effects(evaporation), drop size, impact direction relative to the surface, ambient condition, surface tension, interfacial tension and so on. The droplet impact can be governed by the below equation, which is the main dimensionless groups to determine the droplet impact.

$$We = \frac{\rho D_0 V_0}{\sigma} \tag{1.1}$$

$$Re = \frac{\rho D_0 V_0}{\mu} \tag{1.2}$$

$$Oh = \frac{\mu}{(\rho \sigma D_0)^{\frac{1}{2}}} = \frac{We^{\frac{1}{2}}}{Re} \tag{1.3}$$

$$K = We \cdot Oh^{-\frac{2}{5}} \tag{1.4}$$

Where We, Re and Oh represent the Weber, Reynolds and Ohnesorge numbers, respectively. K denotes composite group. ρ is liquid density, μ represents viscosity and σ is surface tension. D_0 denotes drop initial diameter. V_0 represents the impact velocity.

The droplet impact is hard to explain in a comprehensives single topic because the phenomena accompany an abundance of behaviours and is influenced by a number of factors. Therefore, the studies of droplet impact can be classified into: (1) droplet impact on thin liquid layers;(2)droplet impact on dry solid surfaces;(3)droplet impact on deep liquid pools. The present work mainly focuses on the droplet impact on a dry solid surface. Rioboo et al.[14] summarized the dynamics behaviours of droplet impact on a dry solid surface. Upon the droplet contacting the surface, the impact and substrate parameters affect the droplets impacting outcomes. When the impact velocity is relatively small, the droplet deposits on the surface without splashing. Upon the droplet touching the surface, the droplet spreading outwards driven by the horizontal momentum which is converted from vertical momentum, until it reaches a maximum spreading diameter. Subsequently, the liquid lamella keeps static or retracts back relates to the interaction between the liquid surface tension, the inertia, and the liquid viscous. When droplet impacts on a superhydrophobic surface, the partial or complete rebound can be observed during retracing stage. When the impact velocity increases enough, the droplet will splash, which detaches tiny droplets from the periphery of the lamella and number of secondary droplets are generated. The studies of droplet impact on a solid surface can be divided into three sub-titles in the thesis, e.g., maximum spreading factor, splashing threshold, and the effects of substrate properties. Chapter 2 presents the advances and relevant literature reviews of droplet evaporation and droplet impingement.

Another aim of my research is to explore an effective method to enhance the thermal performance of a PHP. Nowadays, the energy crisis and serious environmental pollution, and the global demands for sustainable energy are threatening people all over the world. The sustainable development of energy and environment can be realized by reduced the irreversibility of energy transfer process, especially the heat transfer process. Pulsating heat pipes (PHPs) are high-efficiency two-phase heat transfer devices with high heat transfer capacity, which is taken as an effective method to improve heat transfer efficiency. As opposed to conventional heat pipes, the PHP is more compact and design simpler, which does not need a wick structure to assist the working fluid back from condenser to evaporator. This technology is currently still being further developed for the purpose of solar energy utilization, waste heat recovery, aerospace thermal management and so on. The heat transfer performance of the PHP is affected by the different factors, which can be categorized into three groups:(1) geometric parameter of PHP; (2) properties of working fluid;(3) operational parameters. Although there are many investigations are carried out to understand the effects of various factors on the thermal performance of the PHP, the optimal conditions have not been found, which can give the best thermal performance over the wide range of operation.

So, the third aim of the present work is to find an effective method to enhance the thermal performance of PHP and further understand the working mechanism of a PHP. This part focus on the effects of various factors of PHPs, and the effect of the MEPCMS on the thermal performance of PHP. In order to further understand the operating mechanism of a PHP, with the help of a high-speed camera, a visualization experiment was carried out in the research to observe the flow motion and flow patterns occurring in the PHP and correlate them with the thermal performance of PHPs.

1.2 Research objectives

There are three main aims for the present work. For the droplet evaporation, most method try to control the distribution of pattern formations by adjusting characters of original solution with chemicals. In many applications, the characteristics of solution can't be changed to control deposition patterns. Therefore, the first aim is to explore effective thermal strategies to control the distribution of deposition patterns without chemicals. On the other hand, the impact happens in various kinds of scenarios, the droplet does not always impact on flat surfaces but could impact on surfaces with complex structures As one of the most representative geometric shapes, droplet impact on conical structures is relatively less studied. So the second aim of my research is study the behaviours of droplet impact on a conical structure

The third aim is to explore effective fluid to improve the performance of a PHP and further develop the understanding of the working mechanism of the PHP. The thermal performance of the PHP is influenced by filling ratio, working fluid, heat input and so on. Working fluids is probably the most important factors affecting heat transfer performances of PHPs. The nanofluids and alcohols are commonly used as working fluid in PHP in recent advances. However, both working fluid has their disadvantage. Therefore, the research keep finding some novel fluid to enhance the thermal performance of PHP. To achieve these aims above, the research can be divided into several scopes as below:

- Explore the relationship between the distributions of pattern formations and different influencing parameters (surface roughness and substrate temperature) and analyze the mechanism underlying the different pattern formations.

- Experimental investigation on the droplet impact on a conical structure with different roughness and cone angle and further reveal effect of the surface roughness and substrate morphology on the droplet impact behaviours.
- Experimentally investigate the effective methods to improve the performance of a PHP and present the relationship between the performance of the PHP and various parameters (filling ratio, heat input, and concentration of working fluid). Furthermore, analyzing the working mechanism of the PHP by different advanced instruments.

1.3 Outline of work

Three related parts are carried out to achieve research objectives of this thesis. The first part focuses on experimental investigations of saline droplet evaporation on a solid substrate with different surface roughness and varying substrate temperature. The second part states the study of the droplet impact on a conical structure with different surface roughness and cone angle. The third part experimentally investigates the PHP operating with MEPCMS working fluid. The main works are outlined and presented in the following chapters.

Chapter 1 introduces the background and necessity for this research. Recent advances in the behaviours of droplets interaction with solid surfaces and PHPs are reviewed briefly. The main objectives of this research are stated clearly.

Chapter 2 introduces the background and relevant theories of droplet evaporation and droplet impact. Meanwhile, the recent advances in droplet evaporation and droplet impact are summarized. In terms of droplet deposition pattern, the important concepts, mechanisms, and various influencing factors studies are comprehensively concluded in this chapter. In addition, it also provides an overview of the PHPs and the recent studies of the PHPs. The recent studies include the effects of different parameters on its thermal performance and visualization study of PHP.

Chapter 3 presents the experimental study of droplet evaporation on the copper substrate with different surface roughness. It discusses the effect of surface roughness on the droplet deposition pattern, and it also reveals the influence of droplet evaporation driven flow and the fundamental of pattern formation.

Chapter 4 experimentally investigate the effect of substrate temperature on distributions of droplet deposition pattern formations and further explore its mechanism with the help of a CCD camera and IR camera.

Chapter 5 is an experimental study of the droplet impact on 9 conical structures with different cone angles and surface roughness. A high-speed camera is used to record the whole impact process and analysis the droplet impact behaviours on the conical structures, especially the effect of surface roughness and substrate morphology on the droplet impact behaviours.

Chapter 6 gives an experimental investigation of a PHP with MEPCMS working fluid. This Chapter includes an outline of the overall experimental setup, an overview of the common devices, and measurement instruments, and an introduction to the test setups in this study. This study focuses on the effects of the various parameters (filling ratio, heat input, working fluid) on the thermal performance of the PHP. It explores the relationship between the thermal performance of PHP and various influencing factors. Furthermore, a high-speed camera is used to record the whole oscillating process of PHP in order to analyze the working mechanism of the PHP. It further describes the flow pattern, flow motion and bubble generation in the PHP.

Chapter 7 summarizes the key findings of this research. It also presents suggestions for future works related to droplet evaporation, droplet impingement and PHP.

Chapter 2 Literature review of droplet evaporation and droplet Impact

2.1 Background of sessile droplet evaporation

The spreading and wetting phenomena were earliest recognized by Galileo in 1612[15]. He observed a flat thin solid floating on the liquid, but he did not have any knowledge of surface tension and the contact angle can't measure. Therefore, he can't further analysis this phenomenon. After a long period time, Gudris and Kulikowa[16] firstly studied sessile droplet evaporation in micro-scale. Mangel and Baer[17] began to investigate droplet evaporation on a solid surface in 1962. After that, many investigations further investigated the effect of various influence factors such as surface roughness, particle size, and so on. Droplet evaporation is a common phenomenon that occurs in nature. However, its complicated mechanism retards the development of its application such as drying patterns for medical applications, dropping of the whole flood, and so on.

The investigations have conducted the studies on the topic of droplets and evaporation over the past 50 years, and published more than 6800 papers in journals, as archived in the Scopus database. Mechanical and chemical engineering account for more than 40%, fundamental physics, and chemistry account for 27%, material science account for 10% and energy application account for 7%[18].

In chapter 2, the necessary concepts of sessile droplet, typical deposition pattern and influencing factors for deposition pattern are introduced in the following section.

2.2 Sessile droplet and wetting

A sessile droplet is defined as a symmetry droplet located on top of a horizontal solid substrate. The droplet with asymmetric shape is defined as asymmetric droplet when the substrate rotates to a vertical position. The asymmetric droplets are investigated and applied for diagnostic purposes [19][20]. The Triple-Phase Contact Lines(TPLC) is used to describe the intersectant position of substrate(solid), droplet liquid(liquid) and ambient and vapour (gas), which occurs in the sessile droplets[21].

The profile of the sessile droplet on a horizontal substrate can be determined by the apparent contact angle θ_Y. For an ideal flat surface, the apparent contact angle θ_Y can be described by the Young-Dupré equation which also expresses the wettability between the droplet and the substrate. The equation is shown below:

$$COS\theta_Y = \frac{\sigma_{sv} - \sigma_{sl}}{\sigma_{lv}} \quad (2.1)$$

The σ_{sv}, σ_{sl} and σ_{lv} represent the interfacial tensions of the solid–vapor, solid–liquid and liquid–vapor interfaces, respectively. Figure 2-1 shows the illustration of the definition of static contact angles formed by sessile droplets sitting on a homogeneous surface. Figure 2-1 (a) demonstrates that the droplet is easier to spread on the surface if the contact angle is smaller than $90°$. On the contrary, Figure 2-1 (b) indicates that the spreading of the droplet is hindered on the surface, and which contact angle is larger than $90°$[22-23].

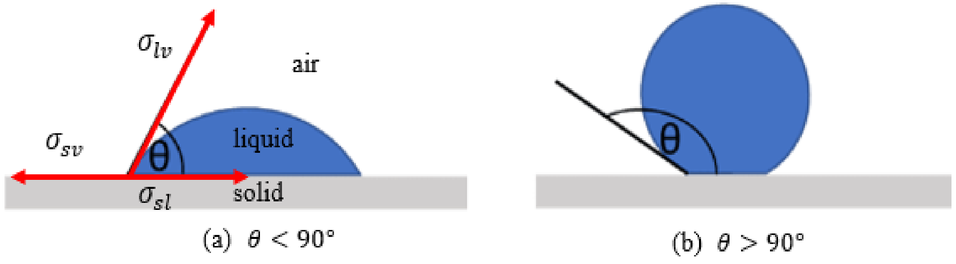

Figure 2-1 Schematic of surface tensions acting on sessile droplets and definition of static contact angles[22][23]

Hence, surface wettability is indicated by the contact angle of the sessile droplet. The schematics of solid surfaces with different wettability classifications are summarizes in Tables 2-1. The solid surface can be categorized into four types based on different wettability classifications: superhydrophobic surfaces, hydrophilic surfaces, hydrophobic surfaces and superhydrophilic surfaces. The contact angles normally change between $30°$ to $150°$ on smooth and homogeneous surfaces[24]. The superhydrophobic/superhydrophilic states can be achieved by further increasing or decreasing the contact angles on hydrophobic/hydrophilic surfaces with surface texturing technology.

Table 2-1 Illustration of solid surfaces with different wettability[24]

Contact angle	Wettability	Illustration
$\theta \leq 30°$	Superhydrophilic	

$30° < \theta \leq 90°$	Hydrophilic	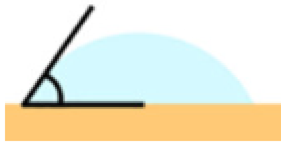
$90° < \theta \leq 150°$	Hydrophobic	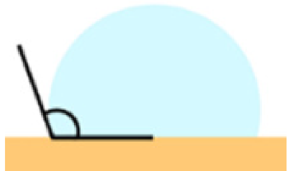
$150° < \theta \leq 180°$	Superhydrophobic	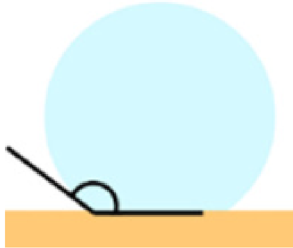

The wetting state of droplets on a smooth surface is different from that on a rough surface. There are two wetting models of sessile droplets: the Wenzel model and the Cassie-Baxter model. Figure 2-2 shows the schematic of these two wetting models. The Wenzel is defined as the protrusions are wetted completely by a king of fluid which fill in the gaps between each protrusion without any spaces occurring between the fluid and substrate[25].

The apparent contact angle for the Wenzel model[26] on the rough surfaces or micro/nanostructures decorated surfaces can be incorporated as

$$Cos\theta_{rough} = \frac{S_t}{S_a} Cos\theta_{smooth} \tag{2.2}$$

The equation(2.2) is called Wenzel equation. Here, $\frac{S_t}{S_a}$ represents the surface roughness factor, S_t and S_a are defined as the true area of the solid surface and apparent surface, respectively. θ_{smooth} represents the contact angle on a smooth surface and θ_{rough} denotes the contact angle of rough surface.

The apparent contact angle for the Cassie-Baxter model[27] is defined as

$$Cos\theta_C = Cos\theta_{smooth} \cdot \sigma_1 - 1 + \sigma_1 \tag{2.3}$$

The σ_1 represents the interface area fraction of the solid substrate. If the wetting model of a droplet is the Wenzel model, it has high contact angle hysteresis and pinning of the contact line[28-29]. The continuous removal of droplets can be achieved by further understanding the transition mechanism between the Wenzel wetting model and the Cassie-Baxter wetting model on a superhydrophobic surface[30].

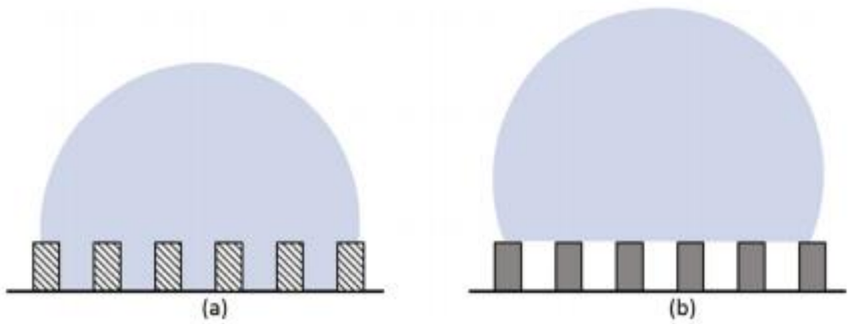

Figure 2-2 Illustration of drop wetting on a rough surface(a) Wenzel's model (b) Cassie-Baxter model[31]

2.3 Sessile droplet evaporation

2.3.1 Different modes of drying

Generally, the droplet evaporation mode can be categorized as two modes based on the behaviours of the contact line and contact angle, which is defined by Picknett and Bexon in 1977[32]. First, The Constant Contact Radius(CCR) mode which describes that the droplet keeps a constant contact area, but the contact angle of the droplet decreases with time during the whole drying process. Second, The Constant Contact Angle(CCA) mode which describes that the contact angle remains constant, and the contact area of the droplet varies with time though out the drying process. Picknett and Bexon studied the deposition process of methyl acetoacetate drop on a poly surface. Their results revealed the transition of the shape of the liquid droplet affected by this two evaporation modes, as shown in Figure 2-3.

Birdi et al.[33] found that the liquid evaporation rate can be influenced by contact angle. When the contact angle <90°, the evaporation rate is linear with time whereas the evaporation rate is non-linear when the liquid contact angle > 90° on a substrate. Rowan et al.[34] also used the same kind of working fluid to observe the evaporation in CCR mode on methyl methacrylate polymer surface, which exposes to open air and they explain the reason of linearity in evaporation graph in CCR mode. The CCR-CCA mode transition process is influenced by rapid drying as well as slow drying[35]. The CCR mode happens when the weak Marangoni factor fluid is deposited on a high-energy surface, which contact angle is less than 90°[36]. The CCR mode is hampered by different factors. For example, the modes of drying are strongly affected by substrate temperature[37]. In some cases, the pinning of the droplet increases with the increase of surface roughness[38], which is dominated by CCR mode. The CCA mode always exhibits on smooth and hydrophobic substrates when evaporation, which is typical for low-energy surfaces [39-40].

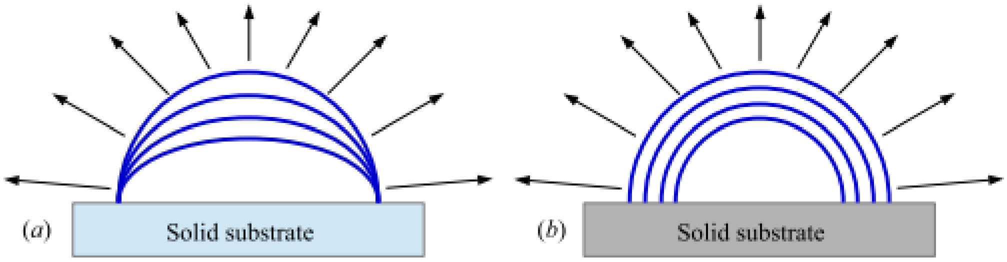

Figure 2-3 Schematic diagram of (a) Constant contact radius(CCR) (b) Constant Contact angle (CCA)[32]

2.3.2 Droplet evaporation driven flow and its fundamental

There are two distinct sources that occur inside drops, which are called buoyancy convection and capillary convection, resulting in convection inside drops. The vertical gradient of temperature is the origin of the buoyancy convection inside a drop. The buoyancy convection can be widely characterized by the Rayleigh number which is shown below.

$$R_a = \frac{g\beta}{v\alpha}(T_s - T_\infty)l^3 \tag{2.4}$$

The l represents the characteristic length. In the case of the sessile drops, the characteristic length is considered as the height from drop apex to substrate. β expresses the coefficient of thermal expansion; v is the kinematic viscosity, which can be obtained by $v = \eta/\rho$, where η is the dynamic viscosity; g is defined as the standard acceleration due to gravity; α represents thermal diffusivity; T_s represents the surface temperature; T_∞ represents the ambient temperature. Convection is the dominating factor instead of conduction when the Rayleigh number high enough the characteristic of that fluid. The cause of 'coffee-ring' could be induced by buoyancy convection. The capillary convection maybe arises in another two distinct effects. Above all, A gradient of Laplace pressure is produced by any distortion of the equilibrium shape of drop free surface. The outward and inward flows can be produced by this gradient, which depends on the shape of the free surface.

The Laplace number describes the ratio of the momentum-transport to the surface tension within a fluid, which is shown below:

$$La = \frac{\rho l \sigma_{lv}}{\eta^2} \tag{2.5}$$

The capillary convection also results from Marangoni flow, which is induced by the gradient of surface tension in sessile drops. The gradient is produced by the non-uniform evaporation flux along the interface of the droplet, which causes differential temperature distribution on the surface. This temperature distribution causes a temperature gradient that, in turn, results in a surface tension gradient along the droplet interface. Therefore, the Marangoni flow is induced by this surface tension gradient.

In terms of the thermal properties of both substrate and fluid, the edge temperature or the apex of the droplet is the highest. Since surface tension increases as temperature decreases. The convection that appears in this situation can be characterized by the thermal Marangoni number. Thermal Marangoni number can be described by the ratio of adhesive force to surface tension induced by the temperature gradient along the interface of the droplet.

$$Ma_T = -\frac{d\sigma_{lv}}{dT}\frac{l\Delta T}{\eta\alpha} \tag{2.6}$$

The concentration of dissolved substances is another factor that influence the surface tension. The solutal Marangoni effect can be observed during the evaporation process of binary mixture droplets and saline[41].

This effect is gave rise to the occurrence of different solutes/dispersions, such as saline, polymer or colloids [42], and surfactants [43]. Therefore, the solutal Marangoni number is necessary to characterize this effect, which presents the ratio of surface tension induced by a concentration gradient to adhesive force. The surface tension increases with the increase of the concentration of electrolytes, and by contrast, the surface tension decreases as the concentration of colloids or polymers increases.

$$Ma_C = -\frac{d\sigma_{lv}}{dC}\frac{l\Delta T}{\eta\alpha} \tag{2.7}$$

Where C is the concentration

To sum up, the Marangoni flow can be induced by the gradient of surface tension, which has two possible resources. First, the gradient of surface tension can be achieved through non-uniform temperature distribution, such as evaporate cooling or heated substrate. Second, the evaporation of binary mixture droplet or saline solution also can cause a gradient of surface tension. This can achieve by drying the multicomponent droplet or adding surfactant to the droplet[44][45].

2.3 Different deposit pattern on the substrate

Deposition patterns is ubiquitous phenomena occurring in nature and practical application. Over the past decades, a number of studies have conducted to understand the mechanism behind different deposit patterns and find effective strategies to control morphologies of drying patterns with various parameters. In this section, the most well-known drying patterns are introduced in the following.

2.3.1 Ring-structure pattern

The coffee ring pattern is one of the deposition patterns of droplet evaporation, which is deposited by non-volatile solute of liquid after evaporation. The fluid transport to the contact line of the droplet is driven by capillary convection. The ring shape generates along the contact line is dominated by CCR mode due to the dissolved or suspended inclusions is transported outward of the droplet until the droplet is completely evaporated. This phenomenon is known as the coffee ring effect[46]. However, the ring shape cannot be generated by the completed evaporation of every droplet. In 2006, Hu and Larson found that the contact line has low temperature than the rest part of the droplet due to the higher evaporation rate at the contact line, the higher evaporation rate leads to a higher solute concentration. The surface tension gradient is caused by the higher concentration, which further induces the Marangoni flow. This leads to the fluid moving to the opposite side of outward capillary flow. Thus, there is a tradeoff occur between the Marangoni flow and capillary convection and the coffee ring pattern only generates when the Marangoni flow is weak within the droplet, as figure 2-4 shown[47].

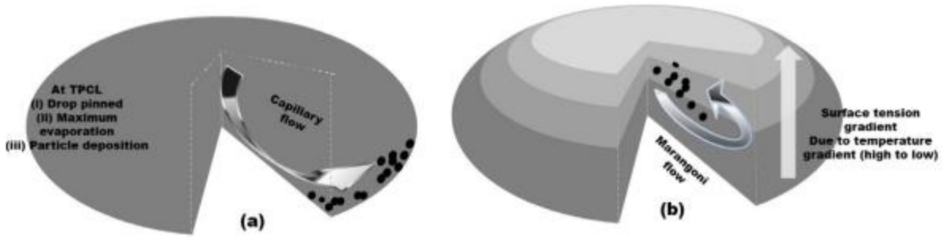

Figure 2-4 Schematic diagram showing (a) coffee ring formation due to capillary flow, (b) Marangoni flow due to temperature gradient or surface tension gradient.[48]

2.3.2 Dome-shaped structure pattern

In the previous study, the dome-shaped structure pattern happens in CCA mode, which particles accumulate at the central region of the droplet drying pattern shown in figure 2-5. Thokchom et al. [49] investigated the evaporation process of an inkjet-printed droplet. They found that the dome-shaped occurred when the Marangoni flow dominates the flow field, which transported and delivered particles from the contact line to the central region wherever self-assembly occurred. Finally, the dome-shaped structure form which was induced by Marangoni flow. Uno et al.[50] studied the droplet deposition patterns formed on hydrophilic and hydrophobic surfaces. During the evaporation process, the particles were prevented accumulating at the fixing contact line by the shrinking edge. The dome-shaped pattern was formed when the concentration achieved a certain value and aggregate in the central region.

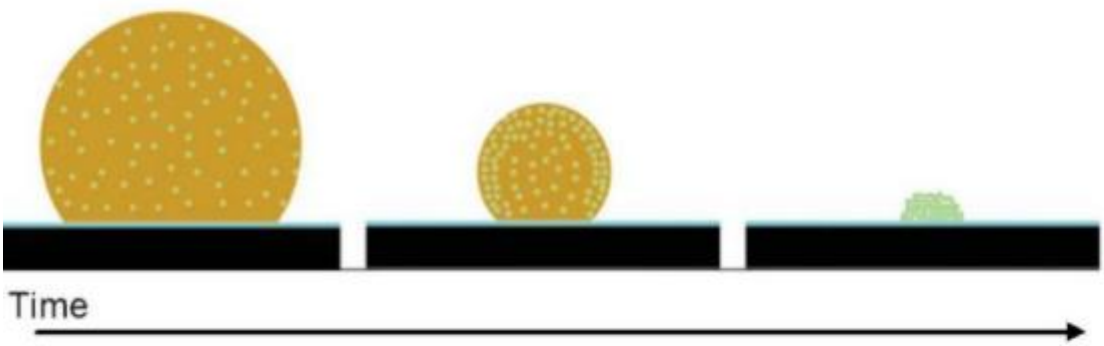

Figure 2-5 the formation of the dome-shaped pattern[51]

2.3.3 Stick-slip pattern

As Figure 2-6(a) shows, the stick-slip pattern contains a series of concentric rings after complete evaporation, which combine the ring-structure pattern and dome-shaped pattern. Moffat et al.[52] investigated the evaporation behaviours of ethanol droplets containing TiO_2 particles. They reveal that the stick-slip pattern always happens in mixture of CCA and CCR drying mode. The ring structure form due to the particles transport outward along the contact line when the evaporation mode is CCR mode of mixture modes. When it comes to CCA mode, the particles are delivered from the edge to the central region of the droplet and accumulate at the central of droplet. Eventually, the multiple concentric rings forms when the CCR mode and CCA mode occur alternately. However, many experimental results show that the particles are not shrink inward simultaneously but contract from one side of the droplet. Adachi et al.[53] numerical study the suspension droplet dries on the substrate. Their model describes the oscillatory motion of the stick-slip process, which includes friction force. The friction force hinders the particles transfer from central region to the edge. On the other hand, the striped stain pattern forms at the contact line due to the oscillatory motion induced by surface tension and friction force. As a result of the tradeoff between the surface tension and friction force, leading to the oscillatory motion of droplets and forming stick-slip pattern, rather than evaporation modes.

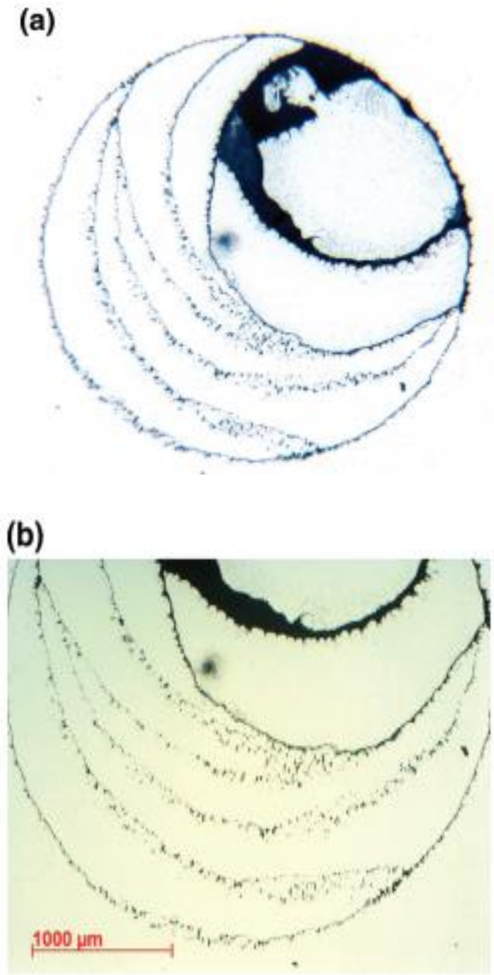

Figure 2-6 (a) evaporation of ethanol containing TiO_2 particles. Each ring of particles corresponds to the stick-slip pattern. (b) Magnified image of stick-slip pattern [54]

2.3.4 Crystal pattern

The crystal pattern appears when the NaCl solution drops completely evaporation at the pinned TPCL. The mixture of CCA and CCR modes is the key parameter for the formation of crystal patterns [55-56]. Many investigations interested in crystal patterns, because it is widely applied in medical science. Dutta Choudhury et al.[57]investigated the drying of a droplet of gelatin containing NaCl under various relative humidity. As figure 2-7 shows, they reveal that the crystal growth is more regular and symmetric with increased humidity. Due to the absorbing ions on the macromolecules, the crystalline property of the polymers increases as the saline concentration increases, which further influences the distribution of the deposits. This effect has been studied on human serum albumin(HSA) and salt solutions[58-59]. At present, the mechanisms of crystal patterns are not well understood, as the main components of crystal patterns are difficult to distinguish by analytical techniques[60].

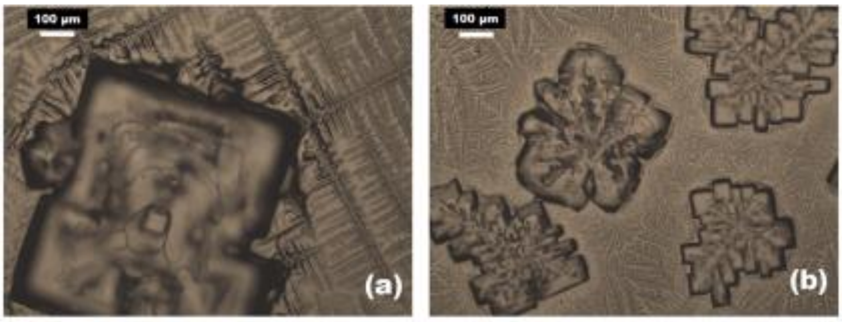

Figure 2-7 (a)deposition behaviours of NaCl in gelatin base with RH 45% (b) RH 35% [57]

2.4 Influencing factors for deposition pattern

In the previous section, the different typical deposition pattern have been introduced and also mentioned various influencing factors that affecting the distribution of drying patterns, such as solution, substrate property, ambient conditions, morphology of droplet and magnetic field.

2.4.1 Droplet properties

As equilibrium (advancing) contact angle depends on the liquid/air and solid/liquid interfacial tension, the surfactants or nano-particles can affect the duration of the spreading state by adsorption kinetic from them thus the duration can be enhanced than those that without surfactant or nano-particles. The surfactant can affect the deposition pattern and the reason are summarized below.

The surface tension along the droplet interface is controlled by the concentration of surfactant which in turn affects the Marangoni flow within the droplet[61].

Gaalen et al.[62] predicted the flow within droplets with soluble surfactant during evaporation by using a developed numerical model. They observed that the Marangoni flow circulation is suppressed by stronger evaporation, slower adsorption kinetic and lower solubility of the surfactant. Their results prove both experimental and numerical results from current studies and also state the differences in flow behaviour of droplets with surfactant. Tim Still et al. [63] investigated drying patterns about surfactant sodium dodecyl sulfate (SDS) modified solution. In their study, they found that the addition of SDS surfactant induced the Marangoni flow along the air-liquid interface, reversing the ring-like structure at the edge and formed a more uniform deposition pattern of colloidal particles. In contrast to these studies, graphite nanofluids droplet with cetyltrimethylammonium bromide (CTAB) surfactant promoted the formation of ring-like structure, but not uniform patterns shown in Figure 2-8 [64].

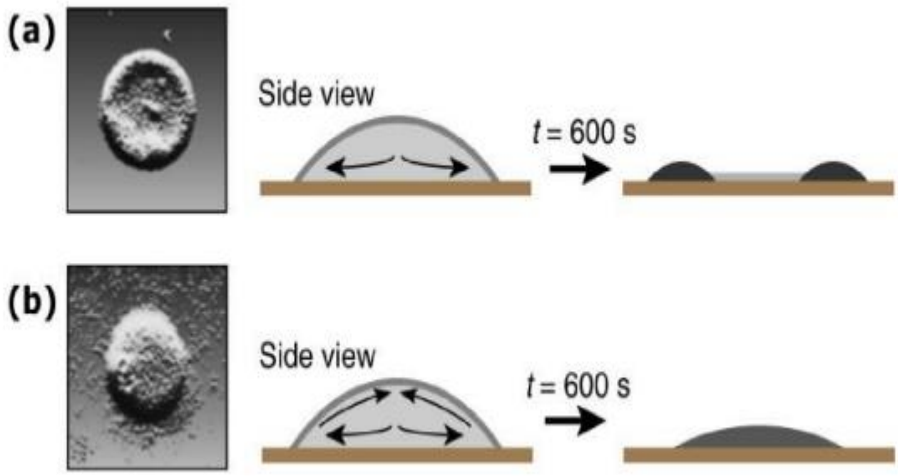

Figure 2-8 (a) A ring-shape pattern was formed without CTAB due to capillary flow (b) A uniform pattern was formed with CTAB caused by the strong Marangoni flow. [64]

The edge deposits of colloidal particles and long chain-polymers [65-66], colloidal particles [67-68] and living bacterial systems[69]also can be suppressed by surfactant. Dier et al.[70] reported a fingering instability at pinned TPCL. They stated that this pattern occurs before the Marangoni flow which is produced by surfactant as well as thermocapillary flow. Kajiya et al.[66] studied the influence of surfactant in the drying and film formation processes of polymer solution droplet. The number of surfactant particles is increased by the convection flow along TPCL during the pinning of the droplets. The local interfacial tension is decreased by surfactant particles at the liquid-air interface adjacent to TPCL, inducing ‘‘Marangoni vortex’’ or ‘‘Marangoni eddies’’ there. This lead to a ‘‘levelling effect’’ in a droplet and provides Marangoni flow which reverses to the coffee ring effect with a fixed contact line during drying process. In addition, the surfactant also can control the ordered array of organic nanoparticles at the boundary of the droplet[71]. Small et al.[72] observed that the evaporation of droplets with surfactant can modify the single-walled carbon nanotube networks. To sum up, the coffee ring effect of nanofluid droplets forms easier by adding surfactant. Crivoi et al.[73] also investigated the evaporation of nanoparticles with surfactant by using mathematical modelling. They found that the patterns followed by surfactant induced nanoparticle flow can be considered by a sticking factor of particles at the contact line.

Nanofluid is another solution that affect the distribution of deposition patterns. Sefiane et al.[74] observed the Al_2O_3 nanofluids with 0.1%,0.5%.1% and 2% concentration. Their experimental results show that the coffee-ring structure exhibited all the concentrations. Furthermore, the thickness of the ring structure increases with concentrations and cracking patterns become more obvious at higher concentrations. Covor et al.[75] in 2004 used 6nm nano-particles of $CoPt_3$ at concentration below 1%, leading to rings measuring 0.6-1.5 μm in diameter. They experimentally studied the formation of a bilayer stricture caused by phase separation. The $CoPt_3$ can be found at the contact line and meanwhile accumulated along the line. In their research, the particles with smaller spheres than their nano-particles also were used, and the droplet assembled more pronounced at the droplet boundary. D.Brutin[76] investigated the pattern formation of nano-particles of iso-density water based nanofluid drops. Nine various nanofluids concentrations were used. Their results show that the deposition pattern switched to a flower pattern when the nanofluids concentration increased to 1.15wt.%. In addition, the thickness increases with increasing of concentration, while the number of flower shapes decreases.

2.4.2 Substrate property

The deposition pattern of the droplet is strongly affected by the substrate property which influences the adhesion of the liquid droplet with the substrate. The molecular interactions between the droplet and the surface molecules of the substrate depend on the substrate property, such as surface roughness, surface energy and thermal conductivity of the substrate. The smooth hydrophilic substrates were applied in most of studies focusing on the coffee-ring effect[77-79]. The formation deposition pattern is affected by the Contact Angle Hysteresis(CAH)[80] which manifested the heterogeneity of the substrate because of the roughness and composition variation. The adhesion with droplets can be influenced by any heterogeneity of the substrate. In the case of the substrate with weak CAH, the droplet recoil when the evaporation starts and then generates a dot on the substrate after completely evaporation. On the contrary, the coffee ring is easy to produce on the substrate with strong CAH, such as the polymer substrates. Li et al.[81] investigated the distribution of deposition patterns of polymer particles. Their results show that the ring-line deposit pattern was generated on the substrate with strong CAH, and a dot left on the substrate with weak CAH, as shown in figure 2-9.

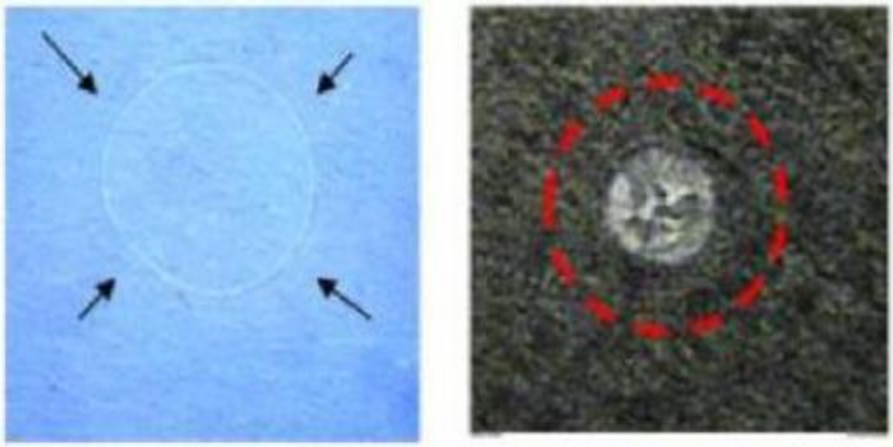

(a) (b)

Figure 2-9 Deposition pattern of polymer particles on substrate with various CAH(a)strong CAH(b) weak CAH[81]

The solute particles show different deposition behaviours when the evaporation mode transfer from CCR mode to CCA mode. When the difference between the receding angles and advancing angle is higher enough, resulting in a stick-slip drying pattern [82]. The multi-ring shape, spider web and foam occur due to the various contact line velocities with the particle deposition growth(figure 2-10). Applying heat can influence the stick or slip behaviours on both hydrophilic or hydrophobic substrate[83]. Nagesh D. Patil et al. [83] compared different surface wettability with the non-heated and heated substrates. In the case of a hydrophilic substrate, the thermal Marangoni flow induces the droplet to leave a uniform peripheral ring pattern in the centre after evaporating completely without heating. When applying heat to the substrate, the Marangoni effect becomes more intense, resulting in a thinner ring shape. When it comes to hydrophobic substrate, the inner deposit pattern can be observed on non-heated substrate due to depinning contact line. In the case of hydrophobic substrates with heat, the pattern deposit at the contact line and leave peripheral deposition rather than depositing at the centre of the droplet. The generation of the peripheral deposition is caused by the reverses the surface tension gradient in the droplet due to the temperature at the centre of the droplet higher than the contact line temperature, finally leading to a thin ring with an inner deposit. Lee et al.[84] investigated the droplet evaporation on the different substrates including glass, stainless steel and Teflon, with contact angle of 55.2°, 80.9°, and 90.4°, respectively. They found that the ring shape pattern easier forms on the substrate with a lower contact angle, while the patterns can be observed at the centre of the peripheral ring on the substrate with a higher contact angle.

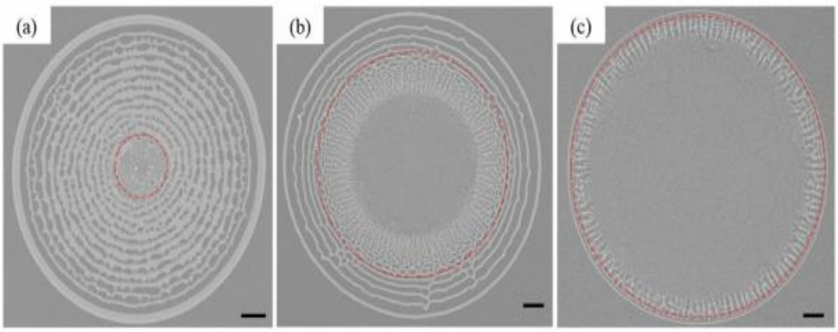

Figure 2-10 Deposition morphologies inside colloidal drops under 40% relative humidity with 20nm particles at different particle volume fractions: (a)0.5%,(b) 0.25%,(c) 0.1%[82]

2.4.3 Ambient conditions

The ambient pressure is another factor affecting the droplet pattern, which can change the effective diffusion coefficient of water vapour in the environment and therefore alter the evaporation rate at the contact line. Askounis et al.[85]

investigated the water based SiO_2 nanofluid evaporated at various ambient pressure, ranging from 750mbar to 100mbar. When the pressure is 750 mbar, the well-established “stick-slip” behaviour dominates the whole process. At 500mbar, a single and uniform ring formed. If the pressure was continuously decreased to 250mbar, the ring structure becomes wider. Their results show that the evaporation rate increases with decrease of pressure, which result in fasted evaporation cycles and, in turn, leads to different patterns.

Relative humidity also influences the distribution of droplet deposition patterns, which also belongs to ambient conditions. Brutin et al.[86] applied 24-nm-diameter polystyrene sphere at relative humidity ranging from 13% to 85%. Their results show that relative humidity only affects the drying rate which is proportional to the humidity but no effect on pattern formation. Chhasatia et al.[87] investigated the evaporation of a pico-liter droplet of a nanofluid under different relative humidity. They observed that the spreading effect increases with the increase in relative humidity for the pinned droplet mode. They concluded that the evaporation process as well as the deposited pattern are strongly affected by the relative humidity. Furthermore, the increased humidity increases the initial spreading of the droplet.

2.4.4 Particle size

Particle size inside the droplet is another factor affecting the distribution of droplet deposition patterns. Chon et al. [88] experimentally investigated the thermal characteristics of evaporating nanofluids droplets with different particles size: 2nm, 11nm, 30nm and 47nm. Their results show that the dry-out stain pattern strongly relates to particles sizes. With the increasing particles size, the temperature span between the droplet center and edge increases. Because of the large difference in thermal conductivity between nanoparticles and water, more particles accumulate at the edge of large nanoparticles, leading to a larger temperature span and distinct ring shape. For the case of nanoparticles, a relatively smaller temperature span is formed by the less distinction between the edge ring and central deposited. Jung et al.[89] studied the motion of micro and an evaporating colloid droplet with nanoparticles on a hydrophilic surface. They found that different size scales show various distributions of droplet deposition patterns and their results are shown in Figure 2-11. For the case of nanoparticles, the pinning effect enhances due to the accumulation outward of particles. While microparticles move inward toward the centre of the droplet because of the surface tension of liquid.

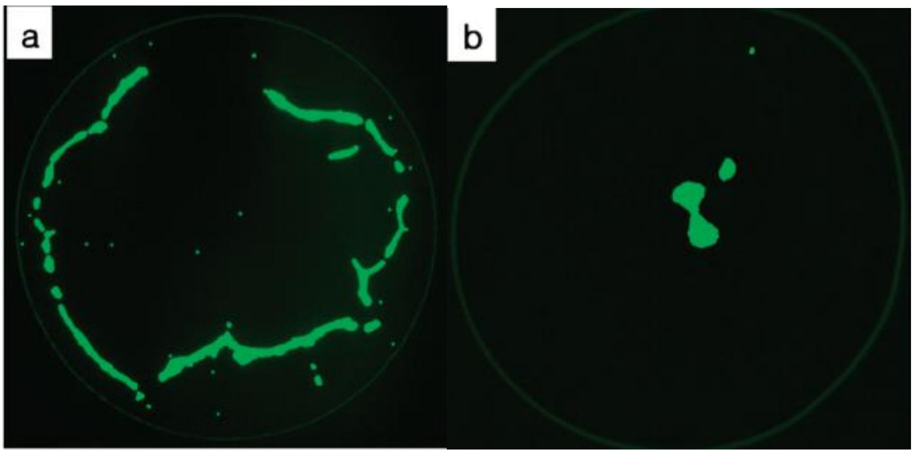

Figure 2-11 Self-assembly of small particles (0.5 μm diameter) and large particles (5 μm diameter) in a dried-out droplet. (a) 0.5 μm diameter (b) 5 μm diameter[89]

2.5 Literature review for droplet impact on a dry solid surface

The droplet impact is firstly studied from 1876, despite 140 years of study, the mechanism of the rapid dynamics of the impact process understand poorly until the past 20 years, the development of high-speed video technology began to allow time-resolved observations, which helped the investigations further investigate the droplet impact dynamics[90]. Studies of droplet impacts are driven by several areas relevant both in nature and in industry. In the case of nature, a stone is hollowed by a droplet, and aerosols is generated by splashing. In the case of industry, spray interacts with the wall during coating, cleaning, cooling and combustion processes. The inkjet droplet plays an important role in the manufacture, from the soldering of electronics to microarrays in biotechnology[91].

This work mainly focuses on the droplet impact on the dry solid surface, I emphasize relative theory and recent works below, which dealt with droplet impacts on the solid surface. Due to the influence of surface property, the outcome of droplet impacts on a dry surface shows more complicated flow shape than those on wetted surfaces[92]. As Figure 2-12 shows, Rioboo et al.[92] observed different flow patterns of droplet impact on a dry solid surface in his experiment.

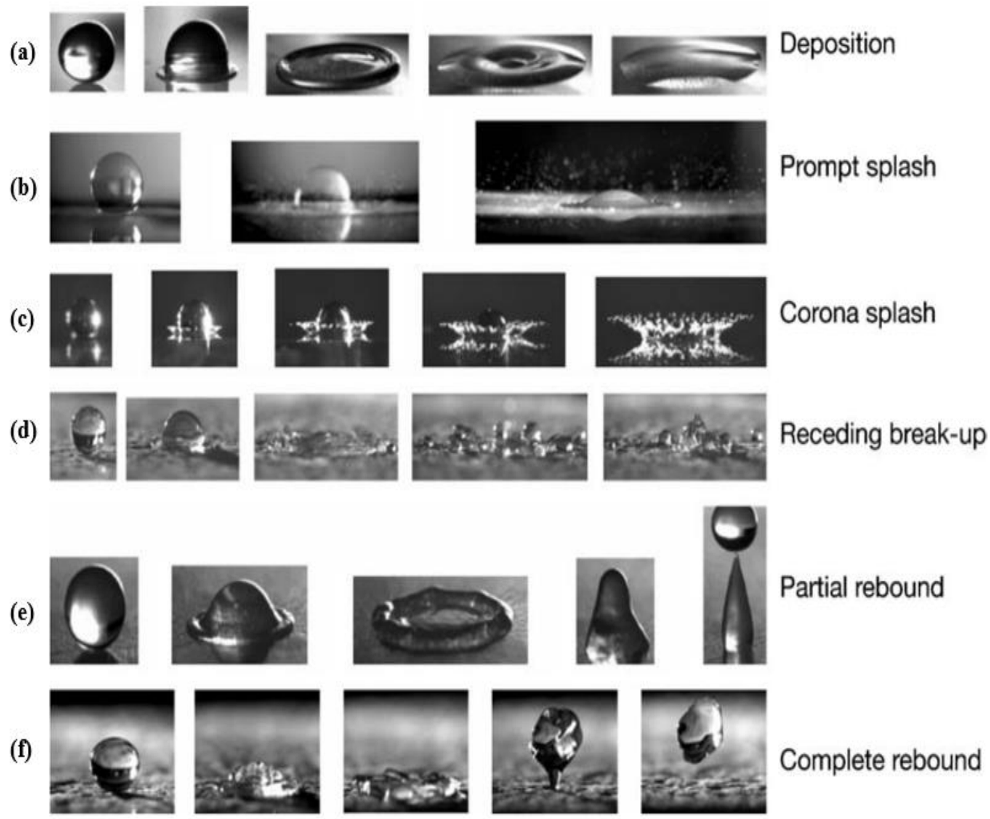

Figure 2-12 outcome of drop impacting onto a dry solid surface (a) Deposition (b)Prompt splash(c)Corona splash(d)Receding break-up(e)Partial rebound(f)Complete rebound [92]

There are two stages contain in the deposition pattern formation: the kinematic and actual deposition, shown in Figure 2-12(a). During the kinematic stage, the radius of drop can be predicted by $R \sim t^{1/2}$ which is not be affected by the physical properties of the surface and the liquid. However, these parameters influence the actual deposition stage. The maximum spreading factor can be obtained through the ratio of the maximum spreading diameter of the lamella at the surface D_{max} to the droplet initial diameter D_0, shown as below.

$$\beta_{max} = \frac{D_{max}}{D_0} \tag{2.8}$$

The initial phase of droplet impact on a dry surface is constituted by these stages, which included the prompt splash scenario, corona splash, receding break-up, partial rebound, and complete rebound. As Figure 2-12(b) shows, in the case of the prompt splash scenario, the tiny droplets are separated from the boundary of the liquid lamella during the droplet spreading, which is strengthened by increased impact velocity on a rough surface. The impacting droplet continues to spread and stays on the surface finally. The reduction of the surface tension results in the liquid lamella being separated from the surface and this pattern is called the corona splash scenario shown in figure 2-12(c). The kinetic energy of droplet impact is partly converted into the surface energy if the free-surface area increases enough and is partly consumed by the viscous forces, further the surface wettability strongly affects the subsequent behaviour of the lamella. Rioboo et al. observed that the diameter of the spreading lamella exceeds the maximum diameter D_{max} when the kinetic energy of the impact droplet is high enough. After spreading the droplet start to recede necessarily due to the surface tension. As Figure 2-12 (d) shows, the receding breakup scenario is observed on non-wettable surfaces, which detached a number of fingers from the shrinking lamella, the fingers able to further breakup due to the capillary. At the end of the spreading stage, there is sufficiently large kinetic energy remaining in the liquid, which does not fully dissipate during the receding stage. In the case of mention above, the receding velocity stays high and the shrinking lamella almost disappears near the impact point. The collapse can still provide enough kinetic energy to bring the liquid upward from the surface and further produce a rising liquid column from the surface. Due to the capillary instability, a part of liquid remains at the surface and one or more droplets bound at its top, which is named the partial rebound scenario and shown in figure 2-12 (e), or and intact droplet is detached from the surface which defined as complete rebound scenario (last line in figure 2-12). Specially, the receding break-up, partial rebound and complete rebounds can be observed when droplets impact on non-wettable or partially wettable surfaces.

Rioboo et al.[92] summarized the effect of each parameter on the six-impact pattern, which shown in Table 2-2.

Table 2-2 summary of the effect of each parameter on each of the six scenarios[92]

Increase of	Deposition	Prompt splash	Corona splash	Receding breakup	Partial rebound	Complete rebound
V_0	↓	↑	↑	↑	↑	
D	↓	↑				
σ		↓	↓	↑	↑	↑
μ	↑	↓	↓	↓		
R_a	↓	↑	↓			
R_w		↓				
θ_{rec}				↑	↑	↑

The experimental studies of droplet impact dynamics can be mainly categorized into: the maximum spreading factor, the splashing threshold and the effect of substrate properties. For the maximum spreading factor β_{max} , the studies mainly investigated the factors influencing the β_{max} and further developed the empirical correlation to evaluate the maximum spreading factor under different conditions. The splashing threshold plays an important role in many applications such as spray cooling and spray impingement occurs in a variety of liquid-fueled engines. It is necessary to find the splashing threshold for the transition from spreading to splashing, which affects the performance of relevant application. Thus, the thesis also focuses on the factors affecting the splashing threshold. With the development of different applications, the enhanced surfaces were designed to meet diverse requirements rather than flat or smooth surfaces. There are amount of research have been conducted to study the effect of surface roughness and substrate morphology on droplet impacting behaviours. In addition, the rebound is observed on hydrophobic surfaces, which relates to many engineering applications, such as self-cleaning[93], anti-icing[94] and anti-bacteria[95]. The investigation on droplet rebound aim to reduce the contact time of duration of whole droplet impact process, which benefits to these applications. Therefore, many strategies were found to reduce the contact time, such as changing the property of the substrate.

2.5.1 Maximum spreading factor

The maximum spreading factor β_{max} is an important quantity to define the outcome of a droplet impact on a solid substrate, which defined by the ratio between the maximum spreading diameter and the initial diameter of droplet.

$$\beta_{max} = \frac{D_{max}}{D_0} \tag{2.9}$$

Recently, the empirical and theoretical models of β_{max} have been developed and proposed, which correlate β_{max} with non-dimensional parameters. All these relations aim to predict the maximum spreading size, and there have been recent advances in the understanding of the mechanism behind this phenomenon from both numerical, experimental, and theoretical works. Singh et al.[96] observed the drop impact on a polymethyl methacrylate when airflow is incident. Their results reveal that the maximum spreading diameter increases with the Re_{air} and for a give We_{water}. They also proposed a theoretical model $\beta_{max} \sim \sqrt{\frac{We_{water}+12+(We_{air})}{3(1-cos\theta_a)}}$. Lin et al.[97] experimentally studied the impact behaviours of droplets on solid surfaces with different wettability. The droplet deposits on the surface when reaching the maximum spreading diameter on the superhydrophilic surface. On the superhydrophobic surface, the droplet behaviours depend on the droplet viscosity and impact velocity. They proposed a scaling law to predict the maximum spreading ratio $\frac{t_s}{\frac{\rho R_{max}^3}{\gamma}} = 0.92We^{-0.43}$ (where γ is surface tension, R_{max} is maximum spreading radius), which considers the effects of liquid viscosity and surface wettability. The most commonly used formulas are presented in Table 2-3, summarized by Josserand and Thoroddsen[98].

Table 2-3 Different models for the maximum spreading factor

Reference	**Droplet-surface**	**Expression**
Scheller & Bousfield[99]	Water, ethanol droplet impact on the smooth polystyrene glass	$\beta \sim 0.61\ (Re^2 Oh)^{1/6} = 0.61\ Re^{1/5}(We\ Re^{-2/5})^{1/6}$
Clanet et al.[100]	Water droplet impact on the smooth super-hydrophobic surface	$\beta \sim We^{0.25}$
Roisman[101]	Water impacts on the smooth surface of different material	$\beta \sim 0.87\ Re^{1/5} - 0.4\ Re^{2/5}\ We^{-1/2}$
Sen et al.[102]	Biofuel droplet impacts on the stainless steel surface	$\beta \sim 1.73 We^{0.14}$

2.5.2 Splashing threshold studies

When the impact velocity increases enough, droplet splashing can be observed. The splashing threshold can be defined by the minimum impact velocity resulting in droplet breakup and generation of secondary droplets. There are three typical types of splashing occur: prompt ,corona and fingering splashes. A prompt splash happens when a droplet impact on the rough surface, which releases tiny droplets from the periphery of the advancing lamella. Corona splash is always observed on a smooth surface, which liquid lamella is detached from the substrate and forms a bowl-like structure, subsequently breaks up into fine droplets. Fingering splash is caused by the Rayleigh-Taylor instability at the rim of the expanding lamellae[103].

Classically, Stow and Hadfield[104] and Mundo et al.[105] proposed a splashing parameter to characterize the splashing threshold, which is shown below

$$K_{splashing} = We\sqrt{Re} \tag{2.10}$$

The splashing parameter K relates to liquid inertia, viscous stress and surface tension, and the splashing will happen when the force associated with surface tension is much smaller than the inertial forces. Range et al. [106] experimentally studied the dynamics behaviours of water droplet impacts on the aluminum surfaces. They found that substrate roughness plays an important role in the critical value of $We\sqrt{Re}$. Bird et al.[107] observed an inclined liquid droplet impact on surfaces. They proposed a splash threshold(equation 2.15) for inclined droplet impact and the equation predicts that the threshold velocity for splash increases for higher liquid viscosity.

$$WeRe^{\frac{1}{2}}\left(1 - 3.5\frac{V_t}{V_n}Re^{-\frac{1}{2}}\right)^2 > 127 \tag{2.11}$$

Where V_t and V_n denotes the tangential impact velocity and normal impact velocity, respectively. Van der Wal et al.[108] investigated the droplet with different viscosities impact on a very smooth surface. They proposed a critical capillary number $Ca = We/Re$ to predict the splash threshold. Their experimental result contradicts with the Bird's equation, in which threshold velocity decreases for higher viscosity. Xu et al.[109] observed the droplet impact on the smooth substrate by adjusting the surrounding air pressure. They demonstrated that the corona splash can be suppressed by reducing the surrounding air pressure. Stevens et al. [110] developed the Xu's discovery and investigated the liquid viscosity effects on the impact behaviours under varying surrounding air pressure. They demonstrated that increasing the liquid viscosity results in threshold surrounding air pressure becomes non-monotonically.

Moreira et al.[111] ,Marengo et al.[112] and Roisman et al.[113] summarized variants of the above power laws and current findings exist in the literature(figure 2-13). The current studies devoted to find the critical values of K for various impact condition and effect of various factor on splashing behaviours. However, the influence of different factors have not well understood and do not have a universal correlation of the splash threshold [114].

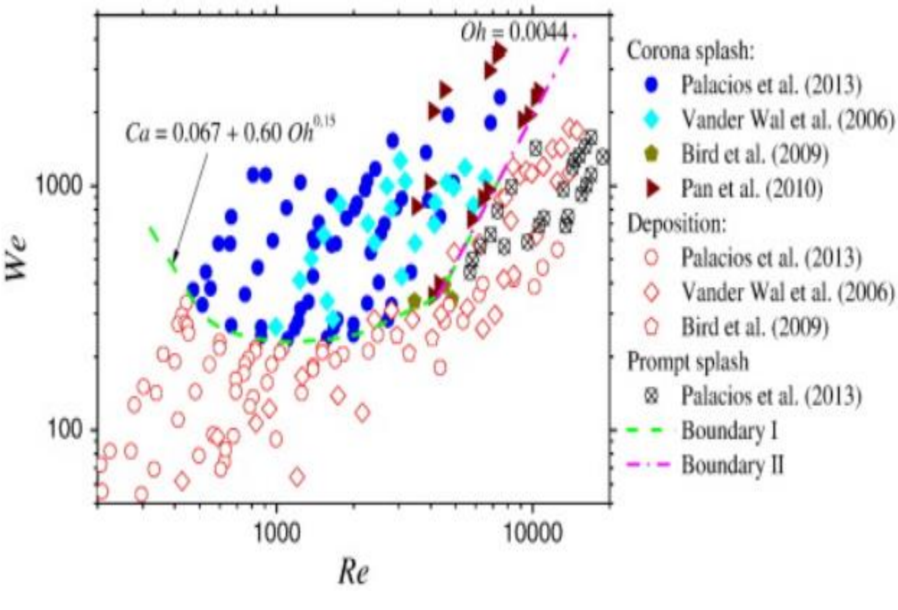

Figure 2-13 Map depicting the outcome of drop impact at normal ambient pressure[113]

2.5.3 The effects of substrate properties

With the development of different applications, the enhanced surfaces were designed to meet diverse requirements rather than flat surfaces. The enhanced surfaces manufacture with different surface wettability, surface morphology and surface roughness.

Motivated by the lotus leaf, superhydrophobic surfaces have been widely used in various applications to make an impacting drop bounce. Due to the weak adhesion of the surface and small impact area, the droplet rebounds after the spreading, retracting stage when it impacts on superhydrophobic surfaces. The contact time is always used to define the duration of the whole process of droplet impact. For some engineering application, the performance can be enhanced by reducing the contact time, such as self-cleaning, anti-icing and anti-bacteria. Richard et al. [115] investigated the droplet impact on a smooth hydrophobic surface, and they mainly observed the impact velocity and droplet size effect on the contact time. They revealed that the contact time increases as the droplet size increases. However, the contact time remains constant when the droplet impact on the surface with different velocity. Bird et al.[116] designed a flat superhydrophobic surface with macro-ridge structure which is slightly lower than the spreading film. They found that the contact time was reduced by 37% due to the faster retraction process than those that impact on flat surfaces. Shen et al.[117] designed a dome convex superhydrophobic surface and investigated the bouncing dynamics of impact droplets on the surface. They found that droplets rapidly bounce off with a 28.5% reduction in the contact time compared with that on flat superhydrophobic surfaces.

Currently, there are amount studies have conducted on the droplet impact on a surface with various geometries such as pillars[117][118][119], ridges[120], cones [121][122] and spheres[123]. The droplet impacts on the pillars surface is more common in practice, so most of the research focused on the pillars surface.

Juarez et al. [119] machined 8 surfaces with different cross-sectional geometries. "n" represents the number of vertices in their study. They found that the shape of expanding lamella resembles the cross-sectional geometries when $3 \leq n < 8$. When the n further increased, the lamella breakup from the outer rim and does not resemble the geometric cross-section of the target. Hu et al.[117] experimentally investigated behaviours of droplet impact on the superhydrophobic surfaces with a single pillar of different sizes. They demonstrated that the maximum width of droplet decreases with the increasing of pillar size. Furthermore, they proposed a theoretical model to predict the maximum width of the droplets which impact on superhydrophobic surfaces with a single pillar. Chen and Bertola[124] manufactured convex surfaces with different diameters and conducted the droplet impact experiments on these surfaces. Their results show that the retraction phase was strengthened when droplet impact on the surfaces with higher curvature. Luo et al.[125] released a droplet above copper cone structure with different cone angles and found that the contact time decreases with increasing cone angle, while We higher enough, the cone angle does not affect the contact time. When the droplet impact on a surface with decorated morphology, the droplet impact behaviours are strongly affected by the redistribution of mass and momentum transfer during impact processes[126][127].

The surface roughness also strongly affects the droplet behaviours. However, there is a few studies have considered the effects of the surface roughness. Stow and Hadfield et al.[128] in 1981. They reveal that the surface roughness affected the critical value K_c of droplet splash. Mundo et at.[129] and Range and Feuillebois's[130] proposed the splashing threshold was depended on the critical

Weber number which is related to the surface roughness. Cossali et al.[131] developed an empirical correlation demonstrated that corona splash only happens on very smooth surface. With increasing of surface roughness, the corona splash transforms into prompt splash. Roisman[132] studied the droplet deposition and splash on rough and porous surfaces. They found that the splash threshold is mainly affected by Weber number and substrate morphology, R_{pk}/R_{sm} (where R_{pk}, R_{sm} represents average height of protruding peaks above roughness core profile and mean width of a profile element, respectively). Miguel et al.[133] experimental investigated the water and ethanol droplets impacting on smooth hydrophilic, hydrophobic and superhydrophobic surfaces. They demonstrate that the maximum dynamic contact angle increases as the surface roughness increase and the splashing behaviour on substrates can be characterized by the roughness ratio R_{pk}/R_{sm} in his work. Tang et al.[134] observed the various droplet impact on a flat stainless-steel surface with different surface roughness. They found that the droplet impact behaviours changes from spreading to splashing with increasing the surface roughness. Meanwhile, the critical value of $(We/Oh)^{1/2}$ was found to characterize the transition from spreading to splashing. Wang et al.[135] recorded the droplet impact on surface with the help of digital inline holographic imaging. The surface roughness affects the diameter, velocity, angle, height and mass-loss rate of splashing droplet. In addition, they developed a new empirical correlation to characterize the secondary droplets.

In existing research, the effects of the conical structures with different roughness on droplet impingement have not been considered. Therefore, an experimental investigation on droplets impact on conical structures with different surface roughness is carried out in this thesis.

2.6 literature review for pulsating heat pipe

2.6.1 General introduction

Nowadays, the energy crisis and serious environment pollution are threatening people all over the world. Efficient energy management is one of the feasible methods to solve the existing energy crisis and realize the sustainable development of energy and environment. A heat pipe is referred to as superconductors of heat, which can transfer heat from one point to another without any heat loss[136], as a potential thermal management system to improve the heat transfer efficiency and minimize the energy consumption in the heat transfer process. Heat pipe was first produced around early 1960s, and since then different shapes and forms was developed based on this technology. A conventional heat pipe includes three sections: evaporator part, adiabatic part and condenser part. The working principle of a conventional heat pipe is shown in Figure 6-1[137]. The heat is absorbed at the evaporator, then working fluid evaporates and formed vapor flow through the adiabatic part towards condenser due to the pressure difference. The vapor flow condenses and dissipates heat at the condenser section, and then transfers into liquid flow returns evaporator via the wick structure driven by capillary force.

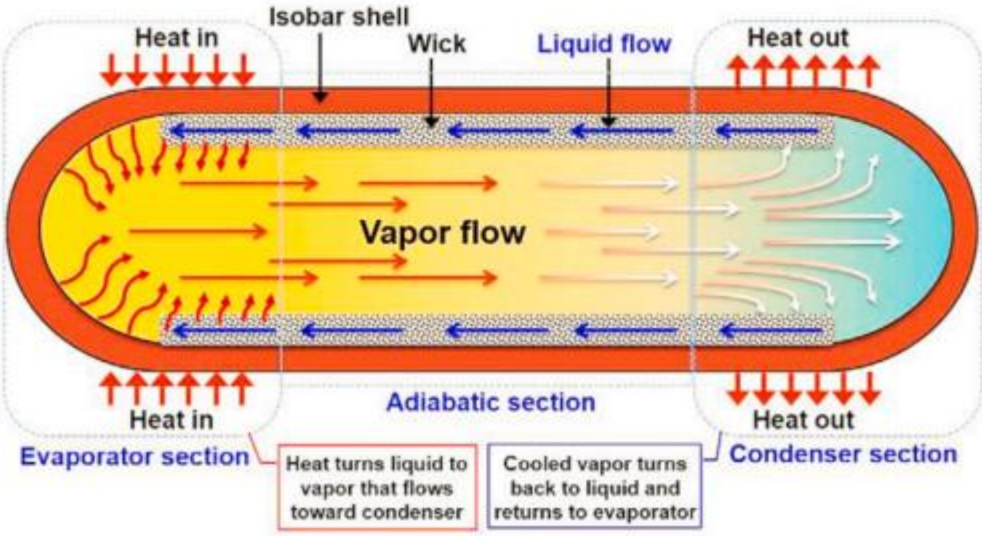

Figure 2-14 Working principles of traditional heat pipe[137]

However, the restriction of capillary force and complex structures limit the application of such heat pipe which is hard to minimize to the microscale. Therefore, Akachi et al.[138] invented an efficiency heat transfer device called pulsating heat pipe or oscillating heat pipe in 1990s with economical solution for solar energy collecting[139],and cooling of electronics and fuel cell[140], micro-electronic device [141], automotive technology [142] and many more. The issues of high heat flux of modern electronic devices directly relate to the PHP heat management system which has compact structure, low cost and simple design[143]. The working mechanism of traditional heat pipes is different from PHP. Although, the PHP also has evaporator, adiabatic and condenser these three parts. Especially, as Figure 6-2 shows that there is no wick structure in the PHP to assist the working fluid back from condenser to evaporator. Therefore, the structure of PHP is more compact and design simpler compared with conventional heat pipes[144]. As Figure 6-3 shows, the pulsating heat pipe include three types: closed loop PHP, closed loop PHP with additional control check valves and open loop PHP [145].

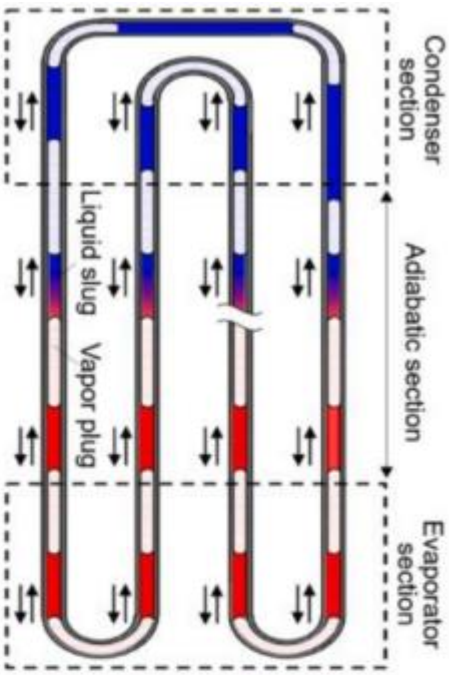

Figure 2-15 Schematic of close loop PHP with closed ended[144]

As Figure 6-3(a) shows, a closed loop PHP is defined as both ends of the tube is connected to form a closed loop. Figure 6-3(b) shows a CLPHP with a check valve which can control the movement of working fluid and adjust to a specific direction. On the contract, the definition of an open loop pulsating heat pipe is two ends of tube are not connected to each other, which is shown in Figure 6-3(c). Most investigations proved that the heat transfer performance can be improved by the potentiality of fluid circulation within the pipe, thus the performance of CLPHP is better than the other two types[146].

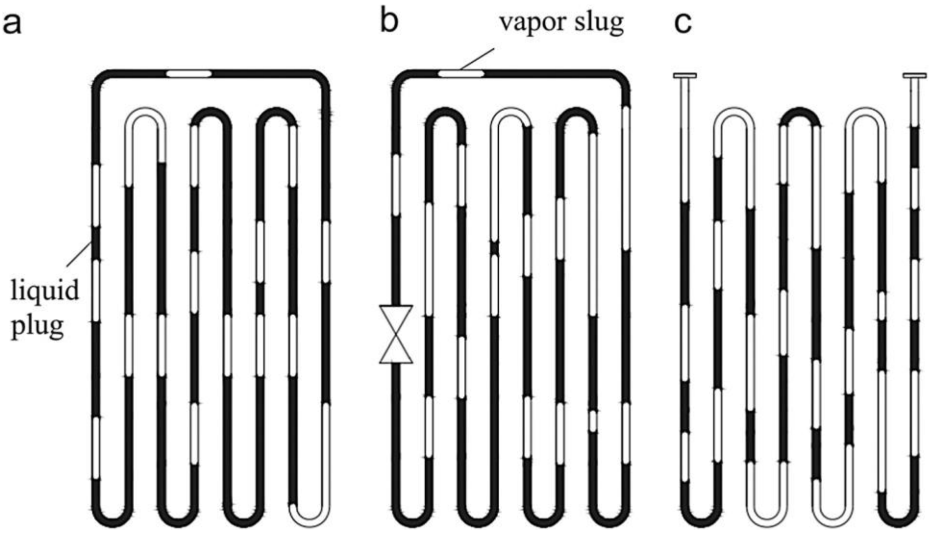

Figure 2-16 (a) closed loop PHP (b) closed loop PHP with check valve (c) open loop PHP[145]

In the CLPHP, the heat will be absorbed in the evaporator section and transferred to the condenser section where is cooler than evaporator section. When the evaporator absorb heat, working fluid evaporates and formed vapor flow through the adiabatic part towards condenser due to the pressure difference. During the working process, the growth, generation and collapse of bubbles are induced by the temperature gradient and temporary pressure within the tube. Therefore, the CLPHP can dissipates the latent heat during vaporization at the evaporator and release the sensible heat during condensation at the condenser. Therefore, the CLPHP is regarded as common type of pulsating heat pipe.

Although PHPs have many advantages such as high efficiency, low cost, good reliability and simple construction, the working mechanism of PHP has not been fully understood yet, resulting in the PHP cannot operate successfully at all situations. Therefore, the topic of development for PHP has attracted attention of a large number of investigations. The investigations are focused on exploring and understanding the working principle, thermodynamics and hydrodynamics of the PHP and influencing factors affects its performance.

The thermal resistance is taken as the performance measuring criterion. The thermal resistance can be obtained by the temperature different between the evaporation section and condensation section and the heat input. Thus, the thermal resistance of the device can be given by the equation below:

$$R_{th} = \frac{T_e - T_c}{Q} \tag{6.2}$$

where R_{th} denotes thermal resistance (K/W), T_e represents the average temperature of the evaporation section(K), T_c denotes the average temperature of condensation section (K), and Q denotes heat input(W).

The thermal performance of the PHP is influenced by various parameters. First, the geometry of PHP, which includes thickness and diameter of tube, length of the tube and number of turns of the PHP. Second, the condition of operation such as the filling ratio, heat input, number of turns, etc. Third, working fluid which have different surface tension, latent heat of vaporization, specific heat capacity, boiling point, thermal conductivity, thermal conductivity, thermal diffusivity. There are amount of research have been conducted to understand the these parameters effect on the thermal performance of the PHP at the moment.

2.6.2 Influence factor for PHP

2.6.2.1 Tube diameter

The thermal performance is affected by the internal diameter of the PHP. The limitation of the internal diameter of PHP can be determine by Bond number

(Bo). In terms of the surface tension, the minimum internal diameter of the PHP can be determined by the below equation which expresses the surface tension drives the flow inside the tube and opposed by the gravity[152].

$$D_{tube} \le D_{crit} = 2\left[\frac{\sigma}{g\left(\rho_{liq} - \rho_{vap}\right)}\right]^{\frac{1}{2}} \qquad (6.3)$$

D_{tube} represents the acceptable diameter of capillary tube, D_{crit} represents the critical diameter, g represents the acceleration of gravity, σ denotes surface tension, and ρ_{liq} and ρ_{vap} denote the densities of working fluid at liquid phase and gaseous phase, respectively.

If the diameter of PHP is not allowable, there are four situations will occur. As Figure 6-4 shown, the oscillations will cease and the surface tension will reduce when D_{tube}>>D_{cr} (Case A). If the $D_{tube} \ge D_{cr}$ (Case B), circulation will generate in the tube, but most of the liquids adhere to the capillary wall with larger plugs of liquid. On the other hands, if $D_{tube} \le D_{cr}$ (Case C) the continuous and efficient heat transfer was assisted by the formation of liquid plugs which is induced by the annular flow with surface tension inside PHP. However, annular flow cannot be developed, and the there is only bulk movement of fluid when $D_{tube} \ll D_{cr}$(Case D)[146].

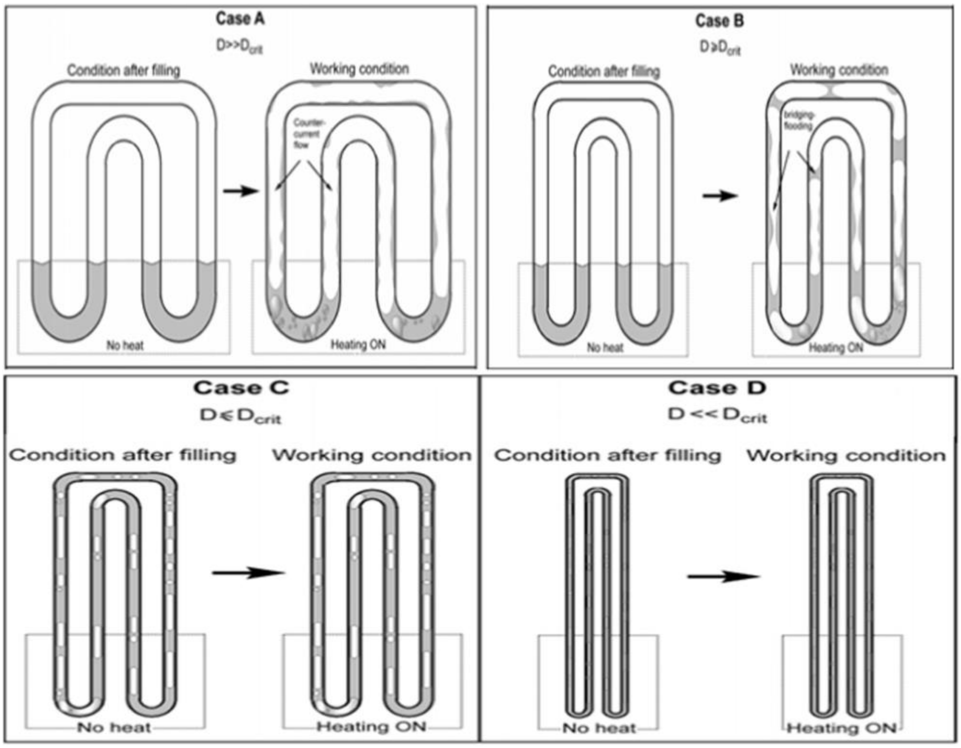

Figure 2-17 The working condition of PHP under 4 different situations[146]

2.6.2.2 Number of turns

Number of turns also a parameter to influence the heat transfer performance of PHP. The volume capacity of the PHP increases by increasing the number of turns and more heat absorb in the evaporator because of wider area. However, the total heat flux is related to the number of turns, the optimum number of turns have not been found yet. Pouryoussefi et al.[147] and Rahma et al.[148] investigated the PHP with 4 turns and 16 turns, respectively. Their results shows that the thermal performance can be enhanced by increase the number of turns. Mameli et al.[149] tested a copper PHP with 32 turns in micro/hyper gravity condition. They found that the thermal performance of PHP is strongly affected by the variation of gravity field. Akachi et al.[150] designed a PHP with 80 turns for experimental study the thermal performance of PHP. They indicate that the inclination does not affect the thermal performance of PHP when the number of turns is high enough. There are no works to explain why the number of turns affects the performance of PHP. Therefore, the relationship between the number of turns and thermal performance of PHP is not very clear.

2.6.2.3 Length of pipe and each section

The thermal performance of PHP is also affected by the length of each section which includes evaporator, condenser, and adiabatic. Otherwise, the performance of PHP is also affected by the entire capillary length of tube which affects the volume of working flow. In previous studies, investigations found that the performance of PHP increases if the heat flux of the evaporator completely dissipates in the condenser area. The heat transfer strongly relates to the effective heat transfer length of the length of the evaporator and condenser. Therefore, making the length of the condenser area equals to the length of evaporator or longer than the evaporator is a more effective consideration to design the PHP operations. Charoensawan et al. [151] investigation the relationship between the evaporator length and thermal resistance. They utilize two copper PHPs with length of each section as 50mm and 150mm. They found that the length of evaporator did not affect the thermal resistance of PHP. The thermal performance was increased by lowing the evaporator length. The variation in thermal resistance for different evaporator length are shown in Figure 6-5.

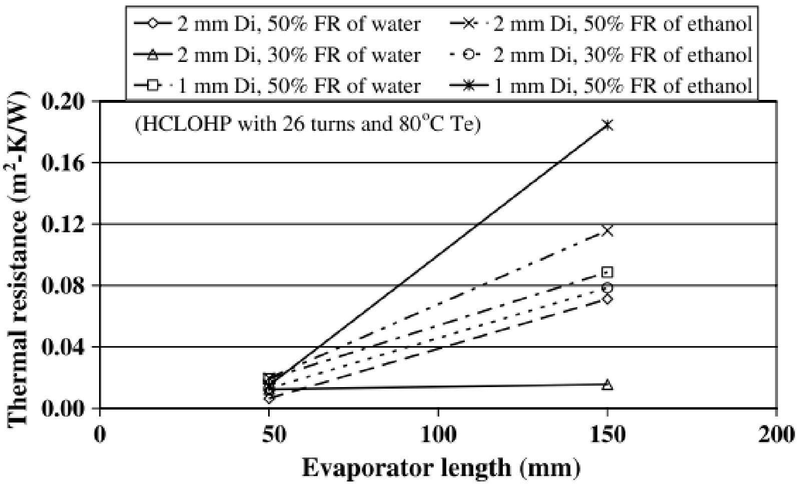

Figure 2-18 The relationship between the evaporator length and thermal resistance[151]

Wang et al. [152] investigated a 2D single loop closed-loop pulsating heat pipe by CFD and experiment. By compare the experimental result and simulative result, they found the start-up accelerates and thermal resistance decease if increase of the length ratio of evaporator to condenser in same condition. Rahman et al. [153] advises that the PHP work more efficient when the heat absorption area of evaporator smaller than the exposed area of condenser. Therefore, they design a PHP which condenser length was 3cm larger than the evaporator. Their result shows that the temperature of condenser did not rise too much when the PHP working and the thermal resistance is gradual decrease when heat supply was increased from 10W to 80W. The length of condenser determines how much heat will release to the surrounding, so for larger length of condenser region, the effective area will be higher and promotes condensation of vapour phase of working fluid inside PHP. Kim et al. [154] experimentally investigated the effect of the condenser length on the thermal performance of a micro pulsating heat pipe under various condenser temperature. They found that the evaporator temperature decreases with decreasing condenser length when the condenser temperature is low. When the condenser temperature high enough, the evaporator temperature increases with decreasing condenser length

2.6.2.4 Filling ratio

The filling ratio (FR) is defined as the ratio of the volume of the working fluid, which is initially filled by the liquid. The FR corresponding to PHP's best performance depends on a variety of factors. There are many research have been conducted to find the optimal filling ratio for PHP operation under different condition. Therefore, there are many research have been conducted to find the optimal filling ratio for PHP operation under different condition. Gamit et al. [155] experimentally investigate the performance of PHP and used the water as the working fluid. The test was conducted for 40%, 50% and 60% filling ratio at various heat supply. They found that the better performance at lower filling ratio and higher heat load. However, different working fluid has different optimal filling ratio. Because different working fluid has different thermal properties. Rahman et al. [156] select the ethanol as the working fluid with 40%, 50%, 60%, 70% filling ratio. The experiment was conducted for different inclination of angle of 0°,30°,45° .60° and different heat supple. It is observed that the better performance of the PHP with ethanol can be obtained when FR is 40% and low heat supply. Bastakoti et al.[157] investigate the thermal performance of PHP with different fill ratios of Methanol, Ethanol, CTAC and DI water at varying thermal loads ranging from 15W to 80W. It is understood from the study that the lowest thermal resistance of the PHP with DI water was 0.34K/W achieved with 50% FR at 75W. Rahman et al.[158] experimental investigated thermal performance of a Vertical PHP with Acetone and DI water working fluid. They found that the optimal FR for PHP with acetone was 70% and the optimal FR for PHP with DI water was 50% due to the different surface tension and latent heat of vaporization.

At the lower filling ratio, less driving force is needed to make the working fluid oscillate in the PHP, which increase the thermal performance of PHP. On the contrary, small amount of working fluid limits the heat transfer capability of the PHP with lower filling ratio. With increase of the filling ratio, the heat transfer capability of PHP increases, but the requirement of driving force also increases. Therefore, the research of PHP with various filling ratio aim to find the optimal FR for different working fluid under different working conditions thus obtain the best thermal performance of PHP.

2.6.2.5 Working fluid

Working fluids is probably the most important factors affecting heat transfer performances of PHPs[159]. In present, many research focused on working fluids and their properties on the thermal performance of PHPS. The working fluid can be categorized into two types based on its property: conventional fluid (pure fluid, mixed fluid) and non-conventional working fluid (such as nanofluids).

For most applications, water and alcohols are commonly used as pure working fluids(conventional fluids) in PHPs[160]. However, these two fluids have different thermos-physical properties(surface tension, thermal conductivity, and viscosity) resulting in different performance when they are used as working fluid in PHP. Kim et al.[161] experimentally investigated the thermal performance of 2 turns PHP with Ethanol and Deionized (DI) water with 50% filling ratio. Their results indicates that PHP with ethanol shows better performance than those that with water at low heat input. Because the boiling point and specific heat capacity of water is higher than ethanol, PHP with water need to absorb more heat to attain the start-up point, in turns, increasing the start-up time compared to PHP with ethanol. Miura et al.[162] used ethanol as working fluid for experimental investigating the thermal performance of PHP. Their results shows that the best filling ratio of working fluid is 50% when the evaporation section and condensation section are equal in length. In addition, the thermal performance of PHP related to the oscillation frequency and amplitude.

However, the thermal properties of pure working fluids are single, which cannot satisfy all requirement for the start-up and oscillating motion of PHPs. Thus, more favorable thermal properties can be obtained by using mixed working fluid for enhancing the thermal performance of PHPs[163].

Zhu et al.[164] studies the start-up and heat transfer performance of PHP with pure water and water-acetone mixtures with different mixing ratios. The results indicated that the PHP with water-acetone mixture has lower thermal resistance and higher start-up performance than that of PHP with pure water. Xu et al.[165] set up an experiment to study the thermal performance of PHP with different mixing ratio(20, 30, 40, 50 and 75vol%) of ethanol-water. They found that 30vol% ethanol-water mixture has best thermal performance than DI water and ethanol-water mixture (20, 40, 50 and 75vol%). It is mainly attributed to synergistic effects between ethanol and water increase the velocity of liquid, in turns, enhanced the thermal performance of PHPs.

Nano-fluid is taken as non-conventional working fluids, which have higher thermal conductivity and dynamic viscosity compared with pure water. However, the thermal performance will decrease which is due to increase in dynamic viscosity of working fluid when the concentration of Nano fluid higher than a certain value. Because the fluid motion will be impeded by high dynamic viscosity in the PHP [166]. Nazari et al. [166] investigated experimentally the effects of heat input and concentration of graphene oxide nanofluid in PHP. They found that the thermal resistance of PHP can be reduced up to 42% by utilizing graphene oxide. In addition, high concentration (1.5g/lit) of the nanofluid has worsen thermal performance of the PHP in comparison with pure water, due to relative higher dynamic viscosity. Qu et al.[167] use Al_2O_3/water as working fluid with five different mass fractions at 0.1%, 0.3%, and 0.6%, 0.9%, 1.2% in PHP. They found that the maximal thermal performance enhancement of PHP was obtained when the mass fraction of the alumina nanofluids is 0.9% which is taken as the optional mass fraction.

The nano-fluids were known as strong method for future to enhance the performance of PHP. However, there is also lack of clearly understand the relationship between concentration of nano-fluids and thermal performance of PHP. Generally, the addition of nanoparticles can significantly improve the thermal conductivity of base fluids, and the presence of nano-particles the nucleation sides. But the presence of nanoparticles also increases the dynamic viscosity and pressure drop inside PHPs, which are not benefit to the fluid oscillation flow and heat transfer. Therefore, more experiment should be carried on and explained how the nano-fluids affect the thermal performance of PHP so that the optimal nanofluids and optimal concentration of nanofluid can be found easier.

2.6.2.6 Heat input

The beginning of the pulsating action is the “start-up time” which also terms the onset of pulsation and this is dependent on the total heat input. V.M.Patel et.al.[168] investigated the start-up mechanism for water(Figure 6-6).They found that 20.87W is the minimum heat input to attain the pulsating flow inside the PHP(Figure 6-7). Meanwhile, with increase of heat input, the start-up time of PHP decreases. Wang et al.[169] used water and sodium solutions as working fluid to investigate the thermal performance of PHP with heat input range of 0-160W. They revealed that the thermal performance of PHP depends on the heat input. With increasing of heat input, the thermal resistance of PHP charged with water and sodium solution both decreases.

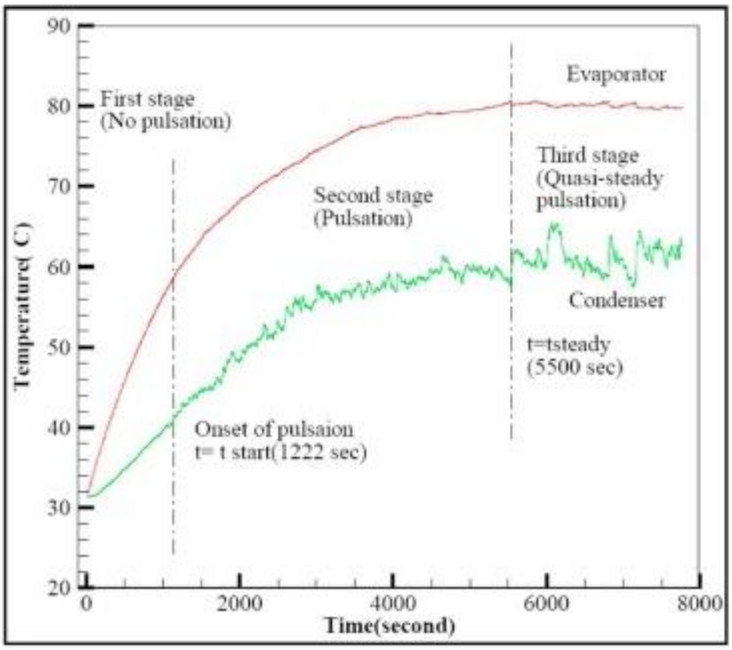

Figure 2-19 The start-up mechanism for water[168]

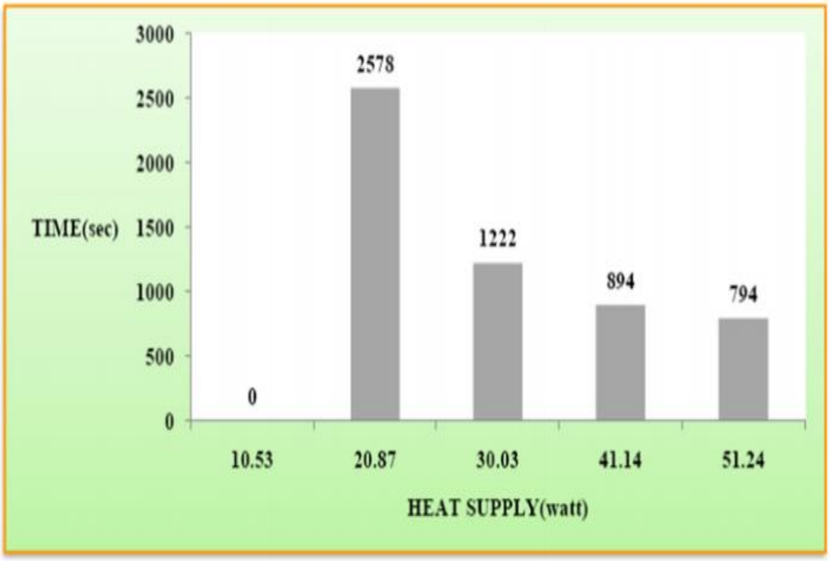

Figure 2-20 Start-up time for different heat input[168]

Heat input play an important role in thermal performance of PHP, but it cannot be an individual parameter to regulate the operational characteristic of PHP. When study the effect of heat input on the thermal performance of PHP, all functional parameters should be considered not just heat input. Hu et al.[185] experimental study the effect of various parameters on thermal performance of PHP. They found that the start-up time is not only affected by heat input but also filling ratio and heating mode. The pulsation of PHP easy to start with bottom heating mode.

In addition, the heat input must not be so high that it results in dry-out of the working fluid. If the supplied power is too low, there will be an insufficient amount of working fluid being supplied to the vapor region of the pipe, resulting in the dry-out condition.

As mentioned above, there is a minimum heat input induce the onset of pulsation inside the PHP. However, the start-up time is not only affects by the heat input but also filling ratio of PHP, mode of heating and so on. Thus, the investigations focus on the start-up of PHP should consider the combined effects of such parameters.

2.6.3 Visualization study of PHP

From the full visualization experiment of PHP, it is very easy to observe the start-up characteristics and flow phenomena which includes the growth and collapse of bubbles, the distribution of vapour-liquids plugs and changes of the flow pattern. According to the existing research, the thermal performance of PHP have a direct relationship with the flow pattern in the tubes[170]. Many visualization studies have been conducted, which using a transparent PHP with the aid of high-speed camera to observe the inner flow of PHP.

In the PHP, the self-sustained thermally driven flow oscillations attributed to the effect of combined the bubble growth, expansion, shrinking and collapse, which provide a pumping action drive the liquid slugs transport between the evaporation section and condensation section[171]. Therefore, observe and analysis the behaviour of bubble in a PHP contribute to further understand the thermo-hydrodynamic characteristics in PHPs. Hosoda et al.[172] experimentally and analytically investigated the heat transport rates and fluid flow patterns of meandering closed-loop heat-transport tube. They found a new propagation phenomena there is a new vapour plug appears in the turn adjacent to the turn including the grown-up vapour plug when the shrinking plug disappears. This phenomenon results in large temperature differences between the liquid and tube wall. Further, The PHP has the best performance when the charging ratio is 60%. Sun et al.[173] mainly focused on the interaction of bubble size distribution, bubble movement, temperature variation in a PHP which made of glass. Their results shows that oscillation frequency and amplitude of bubble movement can be strengthened by increasing the heat input and filling ratio, in turns, enhance the performance of PHP. Senjaya et al.[174]reveal that the motion of liquid slugs and vapor slugs is induced by bubble generation and growth. The generation of TS bubbles(diameter of bubble equal to diameter of tube) accelerates the motion of liquid-vapor interfaces.

The flow pattern is affected by the many parameters such as properties of working fluid, geometrical parameters of PHP and operating parameters during experiment. There are five different types of flow pattern occur in the PHP. At the evaporation section. the annular, semi-annular, slug, and churn flow can be observed at the evaporation section. The major flow pattern at the condensation section are bubbly and annular flow. The discrepancy between these two sections may attributed to the difference of boiling and condensing during heat transfer process[175]. Kim et al.[176] investigated the flow behaviour inside a PHP with different criterion of a diameter ratio($D_h/D_{h,crit}$) . They found that the flow behaviour changes from oscillation mode to circulation mode when the $D_h/D_{h,crit}$ reached 0.5. Ahmed et al.[177] designed a 2 turns PHP for visualization study the relationship between flow patterns and input power. The results showed that the flow pattern changes from liquid slugs and vapor plugs to larger vapor plugs and annular vapor plugs as heat input increased. Patel et al.[178] also studied the heat input effects on the flow pattern. They revealed that the amplitude of flow increases with the increasing of the heat input. The flow patterns also can be change by adding mixture working fluid. Xu et al.[179] conducted a visual study on flow pattern in PHP with mixture of water and HFE-7100. The results showed that the rate of bubble generation and oscillation frequency can be enhanced by applying the HFE-7100 mixture due to its smaller latent heat of vaporization than water. Gandomkar et al.[180] and added CTAB surfactants into working fluid. They indicated that the churn and annular flow was developed by adding CTAB at low heat input, which due to reducing surface tension.

Recently, nanofluids also attracted many research' attention, which also change the flow pattern inside the PHP. Zhang et al.[181] experimentally investigated the effect of the SiO_2-H_2O nanofluids on the performance of PHP. They found that there are amounts of small bubbles generated at the evaporation section after adding the nanoparticles into base fluid, thus the volume fraction of vapor phase is increased which enhanced the heat transfer of PHP. Gandomkar et al.[182] studied flow patterns in two-turns Pyrex PHP and copper PHP using magnetic nanofluids as working fluid. They indicated that the heat input strongly affects the flow pattern. With the increasing of heat input, the slug-plug flow changed to annular flow. At the low heat input, the semi-annular and annular flow are developed with increasing the concentration.

To sum up, the visualization study on PHP mainly focuses on the behaviours of bubble, characteristics and mechanism of different flow patterns which is affected by various parameter. Xu et al.[183] proposed that the visualization experiments need to consider combination of various parameter effect on the flow pattern, such as velocity, the number of nucleation sites, liquid film thickness and so on, in turn, reveal the flow pattern transition conditions and thus further clarify the operation mechanisms of PHPs.

Chapter 3 Experimental study of droplet evaporation on copper substrate with different roughness

3.1 Introduction

The coffee ring effect is one of sub-section of droplet evaporation, which is deposited by non-volatile solute of liquid after evaporation. However, this effect is an unexpected result in adverse effect during the manufacturing process involving inkjet printing[184], spray cooling[185], substrate patterning[186], and DNA/RNA microarrays[187].

Therefore, many investigations have been carried out to understand and control the process of solute deposition in the presence of the coffee-ring effect (CRE). In 1996, Parisse et al. [188] developed a theoretical model to predict the film thickness upon complete evaporation first time. Later, Deegan et al. [189] studied the mechanism of coffee-ring formation by observing the colloid droplet evaporation and their results show that uneven evaporation is the most important role of capillary flow on mass transport.

Thenceforth, there are many investigations studying unceasingly the mechanism of the CRE. The formation of CRE is a complex process and mainly relates to the contact line pinning and contact angle hysteresis (CAH) [190]. Due to the relatively larger proportion of liquid-air interface at the contact line, the evaporation rate is higher there, as a result the flow rate there is also relatively higher [191]. For the evaporation of droplets containing colloidal suspension, the magnitude of Capillary flow affects the order of the particle deposition at the contact line. Marin et al.[192]observed that the capillary flow diverges at the end of the evaporation process, and the particle deposition also transforms from ordered to disordered. Thus, the final arrangement of solute particles in the coffee ring can be controlled by different methods such as solution, substrate property, ambient conditions, morphology of droplet and magnetic field. Meanwhile, the CRE is contributed by a number of other factors such as Marangoni flow [193-194], the geometry of the substrate and particle surface[195-196], the ratio of the thermal conductivities of the substrate and liquid[197]

Thus, the final arrangement of solute particles in the coffee ring can be controlled by different methods such as changing the PH value of dispersion[198], adding surfactant to solutions[199] and using the Nano-fluid[200-201]. The substrate plays one of the most important roles in the drying pattern of droplets. Additional, Zhang et al.[202]revealed that a high-purity vapor-deposited film is hard to be produced by changing the droplet composition, for example, by introducing polymers or changing the particle shape although these methods made a significant advance in controlling the coffee-ring effect during droplet evaporation.

Therefore, the role of the substrate with different morphology and deposition of particles has been studied by several investigations. A part of investigations focuses on the interaction between the droplet and different substrates. Wei Gong et al. [203] used a lattice Boltzmann approach to numerically study the water droplet wetting transitions on the biomimetic surface and clarified the mechanism of wetting transitions. Zu et al. [204] investigated the wetting behaviours of a single droplet on biomimetic microstructure surfaces with different roughness and the results of theoretical analysis can effectively predict the wetting transition. The contact angle hysteresis [205-208] is a factor affecting the pattern formation. The CAH increases with increasing the roughness of the substrate [209]. The droplet evaporates mainly in the pinning mode with a high contact angle hysteresis, whereas the contact line slips easily and the stage of constant contact angle is dominant with a small contact angle [210].

Recently, some investigations investigated the evaporation of the droplets on different morphology substrate. Pham et al. [211] mathematically studied drying of droplets of colloidal suspensions on rough substrates. Their mathematical model can describe several phenomena that were investigated experimentally and therefore, it is suggested that the pinning of droplets to a defect arises out of a competition between the capillary-pressure and disjoining-pressure gradients. In 2018, after investigating the evaporation and patterns of colloidal suspension droplets on glass substrates with different surface roughness, Zhang et al. [212] found that under room temperature, the coffee-ring phenomenon is more obvious than on smooth substrate, and the cross-section of the ring is wedge-shaped with its thickest part on the edge. Lohani et al. [213] investigated the factors affecting the pattern formation process, such as nanoscale roughness, topography, and skewness of roughness. Drops containing polystyrene colloidal particles are adopted in their experiment. Their results showed that with the increase of nanoscale roughness, the wetting property as well as Van de Waals interaction decreases. In 2011, Smith et al. [214] used microscopy and a modified cantilever deflection technique to investigate the crack formation and the evolution of stress in drying films of colloidal particles. They found that the cracking length scale was found to increase with decreasing substrate modulus. Darbha et al. [215] studied the deposition of latex colloids on a nanopatterned surface. They mainly focus on the effects of hydrodynamics and colloidal interactions in transport and deposition dynamics of a colloidal suspension in a parallel plate flow chamber. The results show that the impact of surface roughness on retention is more significant for smaller colloids and explains the differences in retention efficiency of mineral colloids in the environment as a function of particle size.

Most of experiments are carried out when the ambient temperature is near room temperature and the contact angle of a droplet is smaller than 90°. Currently, there are small amount of research about the droplet evaporation under relatively high ambient temperature and the droplet with a large contact angle. Thus, we studied the evaporation and the deposition patterns of saline droplet on a copper substrate with different roughness and the ambient temperature is controlled at 40°C by a water bath. The Marangoni flow is induced under the high substrate temperature because of the temperature gradient. The Marangoni flow also affects the distribution of deposit. In addition, the saline was used as working fluid in the experiment. Due to the significant application on medical science, many researchers focus on crystal patterns. However, there is less studies focused on the effect of substrate temperature and roughness on the dying pattern of saline droplet. We aim to explore the effect of roughness on deposition pattern of saline droplet at 40 °C ambient temperature.

3.2 Experiment set up

The Figure 3.1 shows the set-up of the experiment. A droplet of the saline solution was deposited by a micro-syringe on the copper substrate. Meanwhile, the substrate is attached to the aluminium heat exchanger which is connected to the water bath to control substrate temperature. The volume and concentration of the droplet is 0.2 μL and 2wt%, respectively. The 2wt% saline can be obtained by adding 2g sodium chloride powders to 98g DI water. A CCD camera(basler acA2040-90uc), which was mounted on the microscope(OPTIKA 400), was placed vertical to the saline droplet and records the whole process of the droplet evaporation on substrates with different roughness (201μm, 35μm, 15μm, and 0.2μm) per 1s. Besides, the gooseneck lamp is used to ensure that the CCD camera has enough exposure. To achieve the substrates with different roughness, the copper substrate was polished by abrasive paper with the help of grinding and polishing equipment. The 35μm substrate and 15μm substrate were polished by 400pp and 1200pp abrasive paper. "pp" represents the grits of abrasive paper and the average particle diameter of 400pp and 1200pp abrasive paper is 35μm and 15μm, respectively. Additionally, a high polish copper substrate was polished by the hemp(0.2μm). The 201μm substrate was without any polishing and it was taken as original surface in the study. In the whole experiment, the substrate temperature is set to 40℃, which is higher than normal temperature and controlled by a water bath and the relative humidity is 40%±5%. The data taker (Agilent 34970A) is used to measure the substrate temperature, which connected to two K-type thermocouples with the accuracy of 0.1K. The thermocouples were placed at the centre and boundary of the substrate.

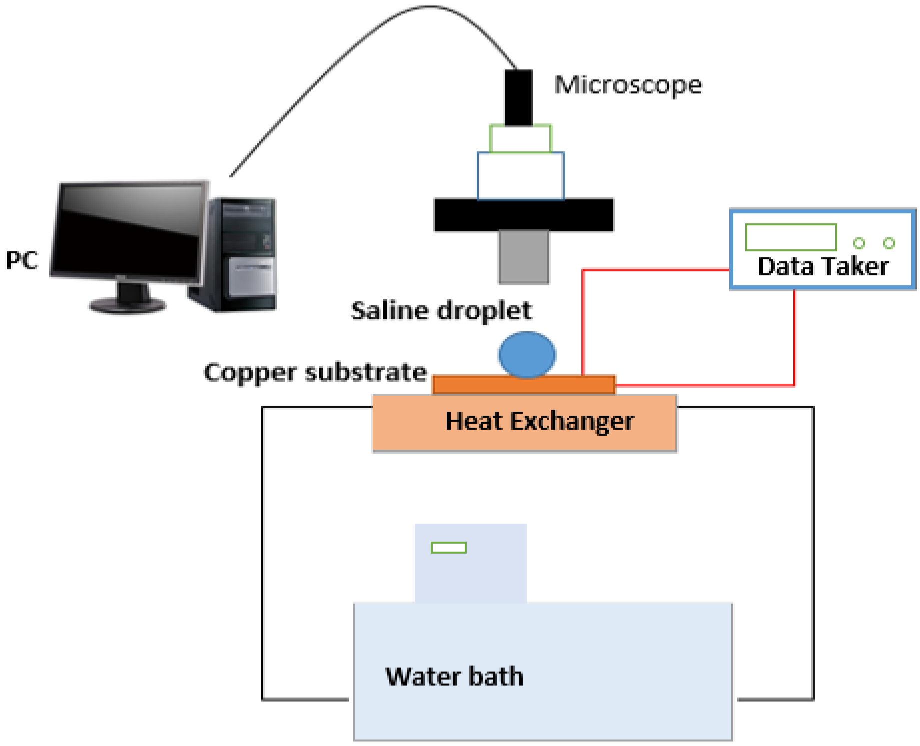

Figure 3-1 The set-up of the experiment

3.3 Contact angle measurement and analysis

The Wenzel model can be used to present and verify the relationship between the roughness and contact angle, which is written as below:

$$\cos\theta^* = r\cos\theta \qquad (3.1)$$

where θ^* is the apparent contact angle which corresponds to the stable equilibrium state, r represents the roughness ratio, and θ is the contact angle of the substrate also called young contact angle. When the roughness increases and θ is constant, the r will increase. Therefore, the apparent contact angle of the droplet is inversely proportional to substrate roughness when the θ^* smaller than 90°. When the θ^* larger than 90°, the apparent contact angle of a droplet in direct proportion to substrate roughness. To investigate the relationship between the substrate roughness and contact angle of the saline droplet. Droplet apparent contact angle is measured for different surfaces, which was carried out via a contact angle meter (CAM200,KSV Instruments). Figure 3-2(a) – Figure 3-2(d) show the results.

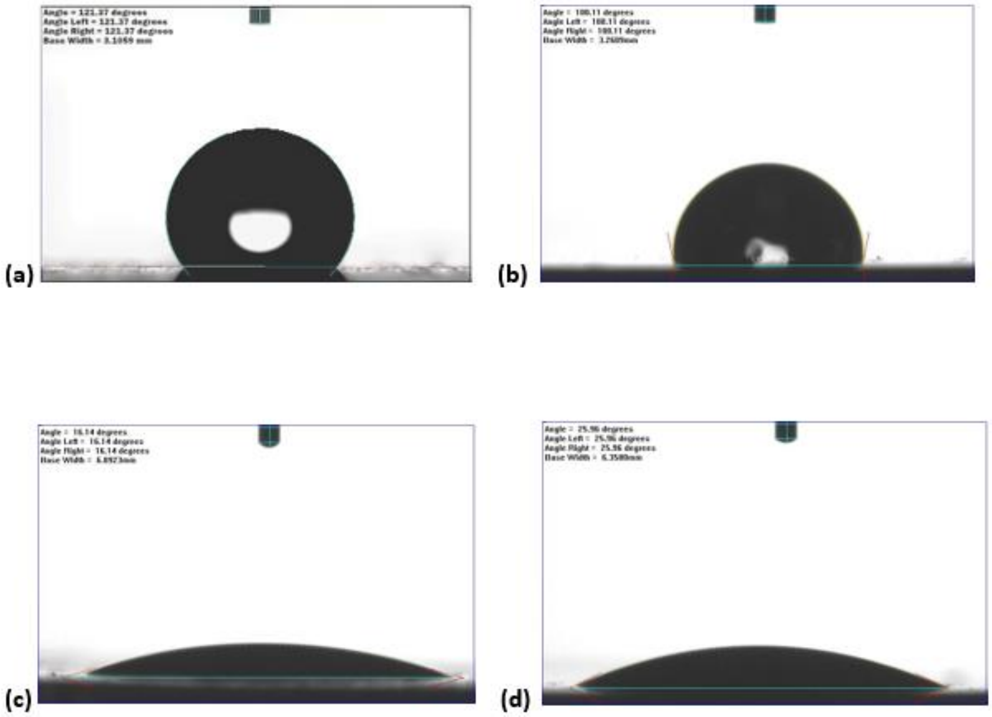

Figure 3-2. apparent contact angle of saline droplets on copper substrate (a) droplet on 201μm surface (b) 35μm (c) 15μm (d) 0.2 μm

Figures 3-2(a) and 3-2(b) show the 201μm surface and 35μm surface respectively. They are classified as rough surface in the experiment, in which the droplet contact angle is large than 90°. With the increase of the roughness from 35μm to 201μm, the contact angle increases gradually from 100.11° to 121.37°, the increase of the roughness can reduce the wetting of droplet on rough surface and the hydrophobicity became stronger. Thus, the contact angle of droplet increases as the roughness increases on the rough surface. Figures 3-2(c) and (d) show the 15μm and 0.2μm surface and they are classified as the smooth surface which droplet contact angle is smaller than 90°. With the increase of the roughness from 0.2 μm to 15μm, the contact angle decreases gradually from

25.96° to 16.14°, the increase of the roughness can promote the wetting of droplet on the smooth surface and enhance the hydrophilicity of the surface. Thus, the contact angle of droplet decreases as the roughness increases on the smooth surface. Therefore, the experimental results follow the Wenzel model.

3.4 Result and discussion

3.4.1 Deposited patterns on difference roughness substrates

The top view of deposited patterns of saline droplets on the rough and smooth substrate are shown in Figure 3-3. The resolution of figure is 96 dpi and the dimension of figure is 2040x2046 pixels. The particle distribution is different between rough surface and smooth surface. The particle distribution of rough surface is much uniform than smooth surface. For the smooth surface, the particles are closer to boundary and tendency more obvious. Meanwhile, the tendency of 0.2μm surface is more obvious than the 15μm surface. The width of the drying pattern decreases with the increase of the roughness on the rough surface, as shown in Figure 3-3(a) and 3-3(b) (3.10mm, 3.26mm, respectively). As Figure 3-3(c) and 3-3(d) show, the width decreases as the roughness decreases on the smooth surface (6.89mm, 6.35mm, respectively). The boundary thickness of the droplet decreases as the roughness decreases on the rough surface. On the contrary, the boundary thickness decreases as the roughness increases on the smooth surface. As shown in Figure 3-3(a) and 3-3(d), the boundary thickness are 0.42mm, 0.4mm, 0.43mm and 0.6mm respectively.

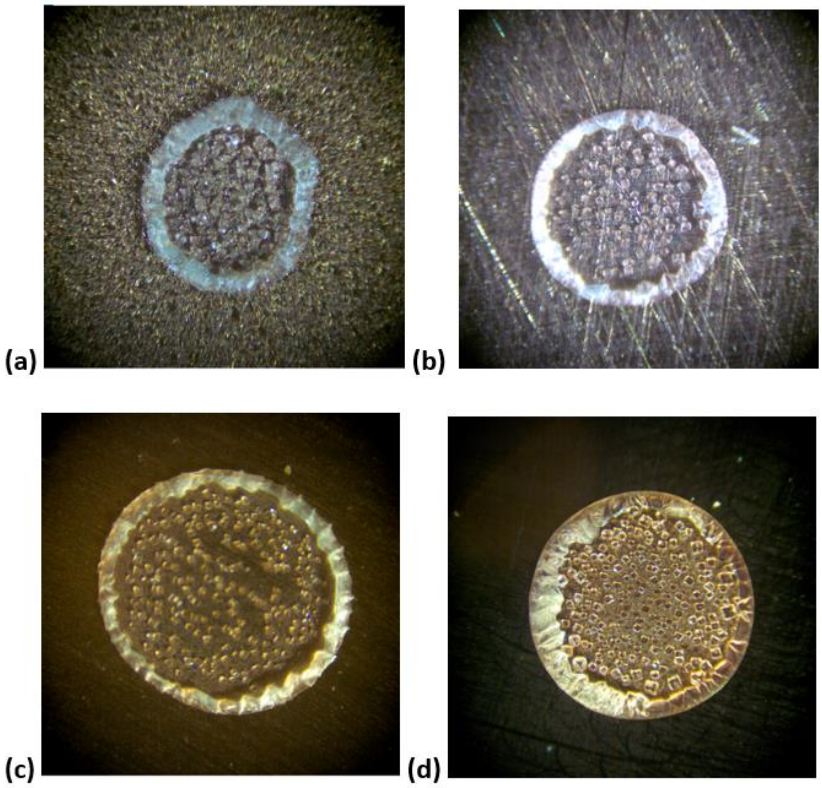

Figure 3-3 Deposition patterns of saline droplets on copper substrates with different surface roughness (a) 201μm (b) 35μm (c)15μm (d) 0.2 μm

3.4.2 Evaporation Dynamics of Saline Droplet

The boundary thickness of the droplet on smooth surface is larger than the droplet on rough surface. Several factors contribute to this result, as shown in Figure 3-4. For droplet evaporation, the edge temperature of the droplet is the highest. Thus, the evaporation rate of the edge is faster than other parts, which results in more saline evaporating at the droplet edge than the centre of droplet. Therefore, the saline moves from the centre to the edge of the droplet to offset the losing part. When the whole process of evaporation completed, the concentration of the boundary is higher than the centre of droplet due to the transported and deposited of the saline. However, due to the larger contact angle, there isn’t a thin liquid layer at the contact line on a rough surface, unlike on a smooth one. Hence, the evaporation rate at the contract line is smaller than that on a smooth surface, and there is less saline particle move to the edge of the droplet and distribute in the centre of the droplet on the rough surface.

Second, the Capillary flow is hindered by roughness of the substrate. This factor results in the particles hard to transport to edge from the centre of the droplet and remain at the centre. It also can explain why the boundary thickness of droplet on the 0.2μm is larger than 15μm surface, despite the boundary evaporation rate of droplet on the 15μm surface is faster than that on the 0.2μm surface. Therefore, the capillary flow is weakened by increasing the roughness of substrate result in more particles remain in the centre of droplet.

For the particle distribution, the particles can be easily transported to the edge on the 15μm and 0.2μm surface because of the relatively faster evaporation rate and stronger capillary flow than the 35μm surface and 201μm surface. Meanwhile, the uniform distribution of 35μm and the 201μm surface due to the height of the droplet on the rough surface is larger than that on the smooth surface. The Marangoni flow also affects the particles to remain in the centre of the droplet. Thus, more particles keep at the central region and then attenuation on the rough substrate.

On the rough surface, as can be observed in the comparison between Figure 3-3(a) and 3-3(b), the boundary thickness on the 201μm is larger than that on the 35μm surface, despite that the Capillary flow is more suppressed by its rough substrate. That could be a result of contact line moving speed. As can be seen in Figure 3-2, the contact angle of the droplet placed on the 201μm is larger than that on the 35μm substrate, thus with the evaporation ongoing, assuming the evaporation mode remains constant contact angle (CCA) mode, the contact line moves slower than that on 35µm substrate. Since the sediment is precipitated mainly on the ring area where the evaporation rate is the highest, it is fair to think that is the reason for a thicker coffee-ring being observed [216].

As the figure 3-4 shows, the contact angle of droplet depends on the substrate roughness, this is most important factor contribute to the results. The droplet with smaller contact angle leads to an increased evaporation rate at edges, resulting in more particles move to the contact line and strengthen the coffee-ring effect. In addition, the capillary flow is hindered by the substrate roughness, so more particles distribute at the center of droplet at rough substrate than those that at smooth surface when the Marangoni flow keeps constant.

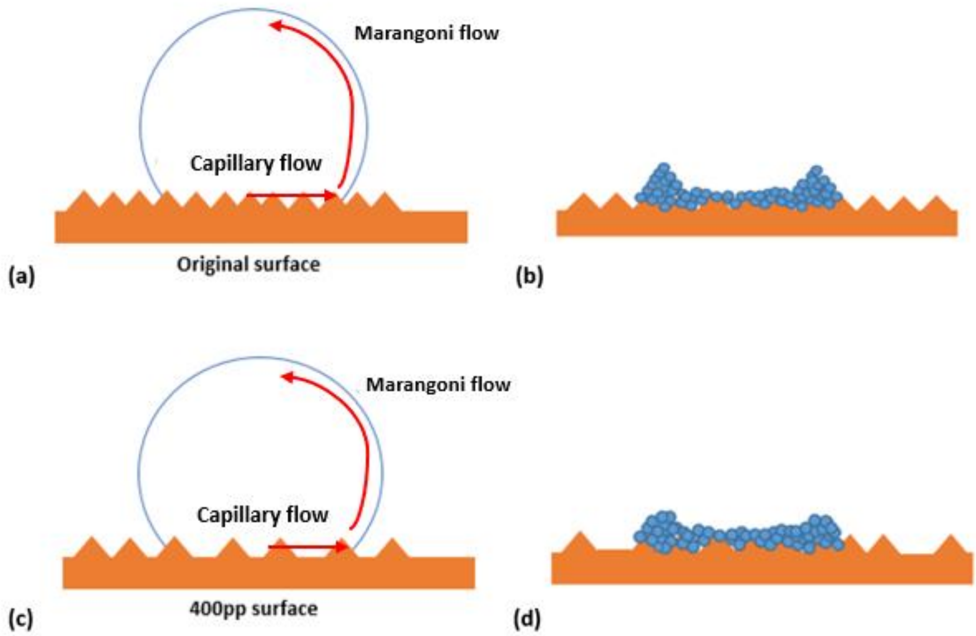

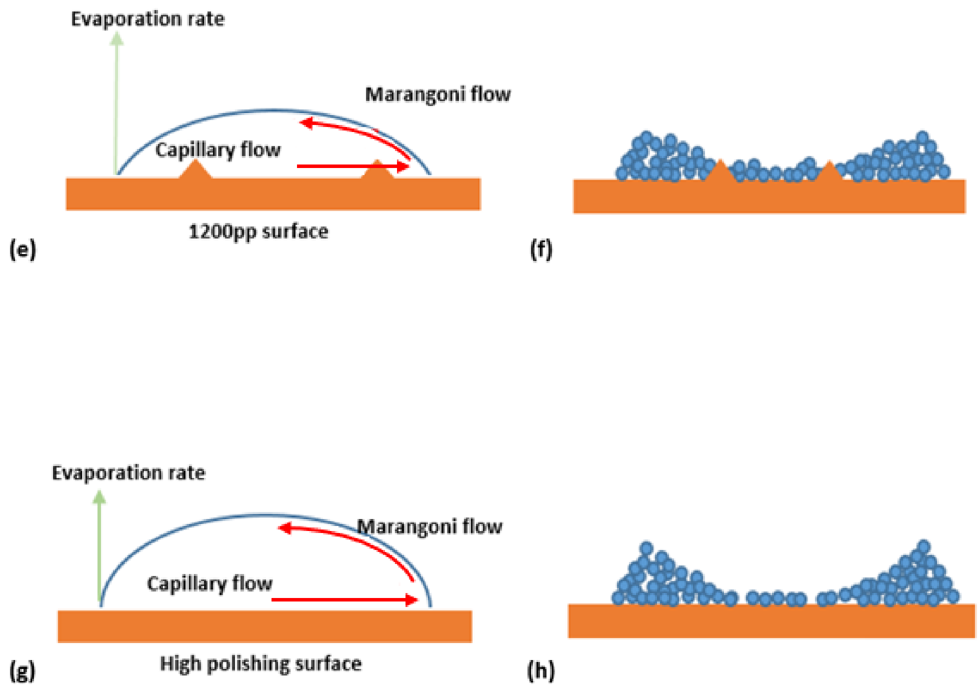

Figure 3-4 the evaporation patterns on a different roughness substrate. (a)(b) On the original substrate(201μm), the contact angle is the largest, there are more particles transported to the edge than that on the 35μm surface due to evaporation mode. A lot of particles remain at the center because of weakened capillary flow while Marangoni flow remains constant; (c)(d) On the 400pp surface(35μm), a few particles move to the edge and a large number remain at the center; (e)(f) on the 1200pp surface(15μm), more particles move to the edge than that on the rough surface and few particles in the center; (g)(h) on the high polishing surface(0.2μm), most of the particles move to the edge because of stronger capillary flow and high evaporation rate at the edge.

3.5 Summary

In the present research, the evaporation of saline droplets on four different roughness substrates at 40° temperature have been studied. We found that the boundary thickness of the evaporation pattern on smooth surface is larger than that on a rough surface and the particles are closer to boundary and tendency more obvious on a smooth surface. These factors contribute to this result:

(1) On the smooth surface, the contact angle decreases and hydrophilicity enhances with increasing of the roughness. On the rough surface, the contact angle increases and the hydrophobicity stronger with the increase of roughness. With

contact angle decreasing, the evaporation rate at the boundary increases leading to the particles at the boundary more easily sedimentate.

(2) The capillary flow is hindered by increasing the substrate roughness. On the rough surface, most of the particles remain in the centre of droplet due to the weakened capillary flow while Marangoni flow remains constant. However, the boundary thickness on the 201μm is larger than that on the 35μm due to their evaporation motion.

To sum up, the coffee ring effect is suppressed by increasing substrate roughness. The smooth substrate helps to produce a ring shape.

Chapter 4 Experimental study of droplet deposition behaviours affected by substrate temperature

4.1 Introduction

In Chapter 3, the effects of surface roughness on the deposit pattern at 40°C ambient temperature are discussed. The results show that the droplet deposit pattern is affected by Capillary flow and Marangoni flow. Therefore, Chapter 4 further studied Capillary flow and Marangoni flow inside a droplet during evaporation process, especially the Marangoni flow. In this chapter, the deposition behaviours of saline droplet are observed by adjusting the substrate temperature, ranging from 15°C to 70°C. Furthermore, the mechanism of the deposition pattern was analysed with the help of the CCD camera mounted with microscopy and IR camera, which is used to record the whole evaporation process of droplet and analysis the temperature distribution of air-liquid interface of sample droplets, respectively.

4.2 Experimental set up

The experimental set-up is shown in Figure 4-1. The water can be passed the internal of the aluminium heat exchanger which is connected to a water bath to control the substrate temperature. A side glass is attached to the aluminium substrate, which is used to support the saline droplet. Meanwhile, two K-type thermocouples placed at boundary and century of the side glass to measure the substrate temperature. The substrate temperature will be set to 15°C, 20°C, 25°C, 55, 70°C. The concentration of saline is set as 2wt% and dropped by the micropipette with volume 2 μL. The 2wt% saline can be obtained by adding 2g sodium chloride powders to 98g DI water. In order to observe the flow motion and analysis the mechanism of different deposition pattern, the Latex micro-beads with average diameter of 3.0μm made of polystyrene applied in the experiment, which is used to track the motion of internal particles. A CCD camera(basler acA2040-90uc) mounted with Microscopy(OPTIKA 400) is placed perpendicular to the droplet and record the evaporation process of droplet. Meanwhile, IR camera(SC7600M) is applied to analysis the effect of temperature distribution along droplet surface interface on deposition patterns. In addition, the gooseneck lamp is used to ensure that CCD camera has enough exposure.

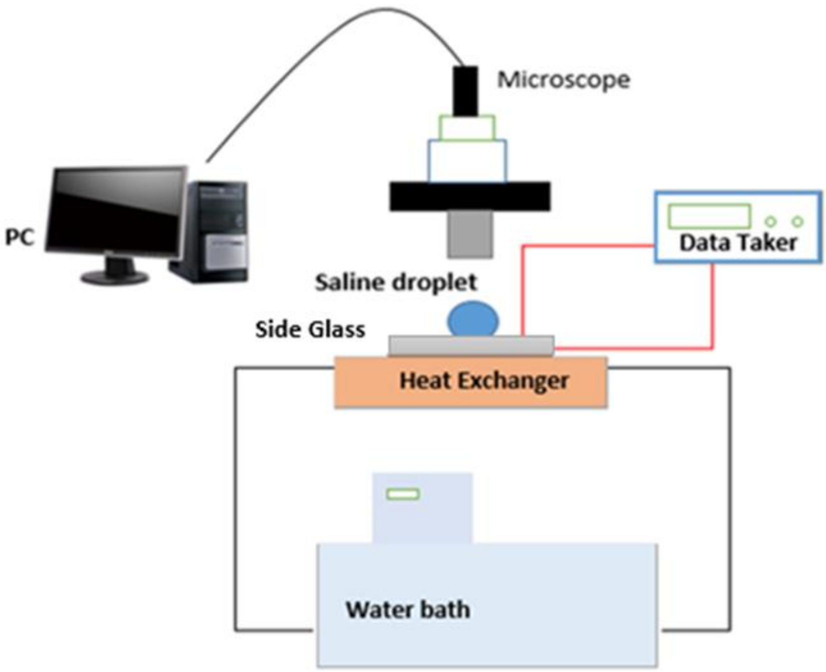

Figure 4-1 Experimental Set-Up

4.3 Results and discussion

In this section, it mainly investigated the droplet deposition pattern affected by different substrate temperature (15°C, 20°C，25°C, 55°C, 70°C). The below figures show the saline deposition pattern under different substrate temperature when the evaporation process was completed. These results can be categorized as three types based on the substrate temperature: low temperature (15°C and 20°C), normal temperature(25°C) and high temperature (55 and 70°C). In order to analysis the feature of deposition pattern more clearly, the dying pattern is divided into three area: central region, gap region and edge region. The central region is defined as the very central area of the whole pattern. For the edge region, it refers to the area close and along the contact line. The area between the edge region and central region is defined as gap region. In addition, the micro-beads are added into the saline droplet to track the flow motion inside the droplet and further reveal the mechanism of formation of deposit patterns at different substrate temperatures.

4.3.1 Deposition pattern of Saline droplets and flow patterns of micro-beads at low temperature (15°C and 20°C)

The final deposition pattern of saline droplet at low temperature is shown in Figure 4-2. After complete evaporation, several large-size crystals distributed uniform within all patterns due to the saturation, but obvious coffee ring effect cannot be observed. The gap cannot be observed at low temperature. Meanwhile, the size of the crystals decreases, and quantity increases with increase of substrate temperature.

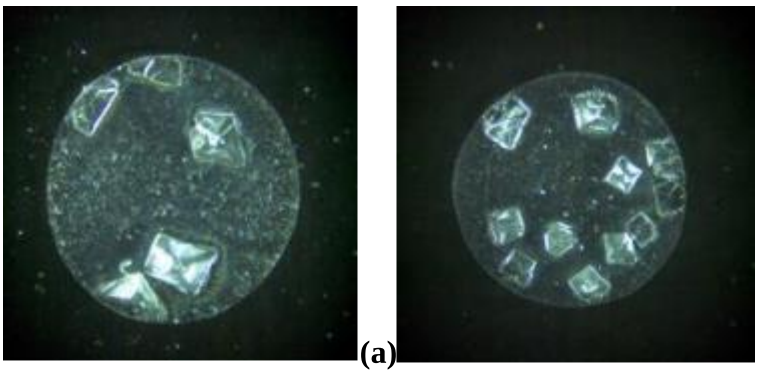

(a) **(b)**

Figure 4-2 The final deposition pattern of saline droplet at low temperature(a) 15°C (b) 20°C

The surface temperature distributions of droplet at low temperature are shown in Figure 4-3. As marked in Figure 4-4, the micro-beads are transported from central area to edge area at the early stage of the evaporation process(0~30s). Because the apex along the air-liquid interface temperature is slightly lower than the temperature along the contact line. Thus, the evaporation rate of the edge is faster than other parts, which results in more saline evaporating at the droplet edge than the centre of droplet. Therefore, the saline moves from the centre to the edge of the droplet to offset the losing part. Due to slow evaporation rate at low temperature, this flow is weak. Meanwhile, the capillary flow also drives the Micro-beads to edge area of the droplet. When the evaporation comes to middle stage(30~80s), the Micro-beads travel from edge to the central region along the air-liquid interface due to the temperature gradient induces the Marangoni flow, and this process are shown in Figure 4-5. However, the Marangoni flow is not intensive due to a relative lower temperature gradient. When the time comes to (300~450s), the Micro-beads do not have obvious movement until complete evaporation as shown in Figure 4-6. Because the evaporation mode is CCR mode, the temperature difference decreases with reduced height of droplet, which means the Marangoni flow further decreases.

At low temperature, both flows in droplet are weak, the particles did not have obvious movement during the evaporation. Therefore, the Micro-beads tend to distribute uniform on both edge and interior.

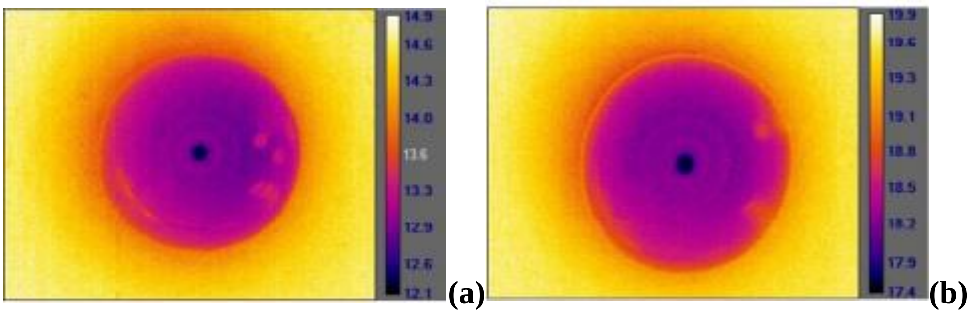

Figure 4-3 Surface temperature distribution (a)substrate temperature= 15°C, (b) substrate temperature= 20°C

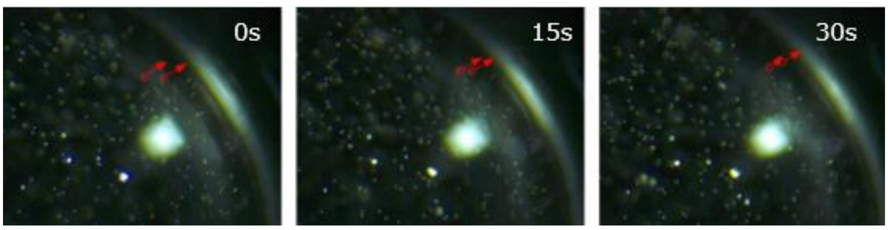

Figure 4-4 The footprint of Micro-beads at early stage of the evaporation process

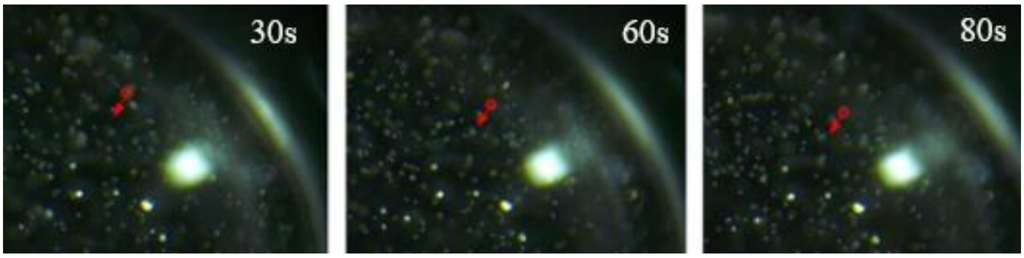

Figure 4-5 Micro-beads travel from edge area to central area

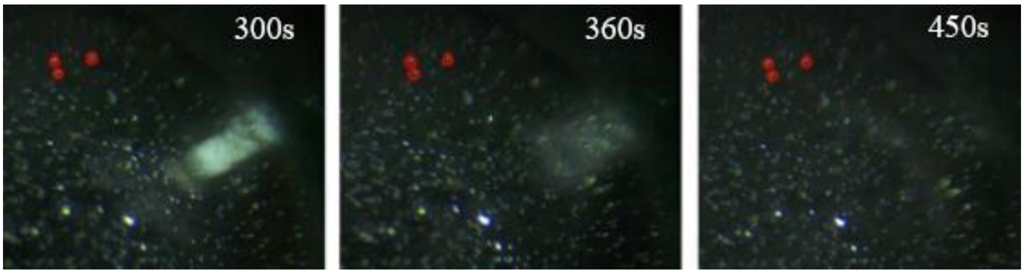

Figure 4-6 Footprint of Micro-beads keep static when the evaporation almost complete

4.3.2 Deposition pattern of Saline droplets and flow patterns of micro-beads at normal temperature (25°C)

Figure 4-7(a) shows the final deposition pattern of saline droplet at normal temperature. Comparing to low temperature, the amount of salt particles distributed at interior significantly reducing. Most of the salt particle crystallized on the boundary region and formed a ring shape structure. As Figure 4-7(b), the temperature along the contact is higher than temperature at apex along the air-liquid interface, meanwhile the maximum temperature differences is larger than that at low temperature, resulting in larger Marangoni flow. As Figure 4-8 shows Micro-beads movement at the early stage of evaporation process at 25°C. During 185s~220s, particles with red mark and yellow mark transported to contact line from edge area to replenish the loss at the contact line, and this flow is strengthened due to the increased evaporation rate at the contact line. The particles movement between the gap area and central area along liquid-air interface are chaotic as the white mark shown. Because it is affected by

Marangoni flow the direction of which is from edge area to apex of droplet, and Capillary flow the direction of which is toward the edge area. The particles closed to the substrate were not affected by Marangoni flow, which flow towards edge of the droplet during evaporation process. As Figure 4-9 shows, at final stage, the particles closed to the substrate continue transport towards edge area (yellow mark), while the Marangoni flow drives the particles from edge to apex (red mark). At normal temperature, the deposit pattern presents a typical coffee ring pattern due to dominant Capillary flow. Meanwhile, the particles in the central region are distributed due to the Marangoni flow.

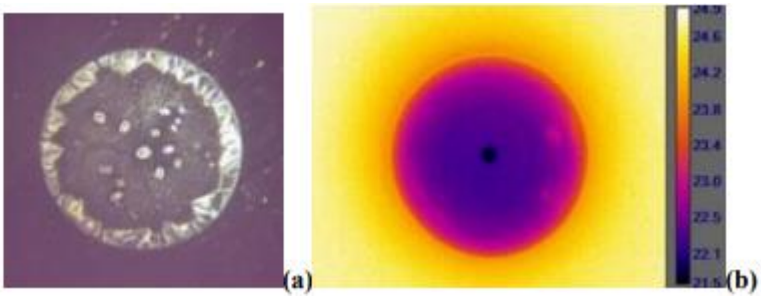

Figure 4-7 (a)The final deposition pattern of saline droplet at normal temperature(b) surface temperature distribution at 25°C

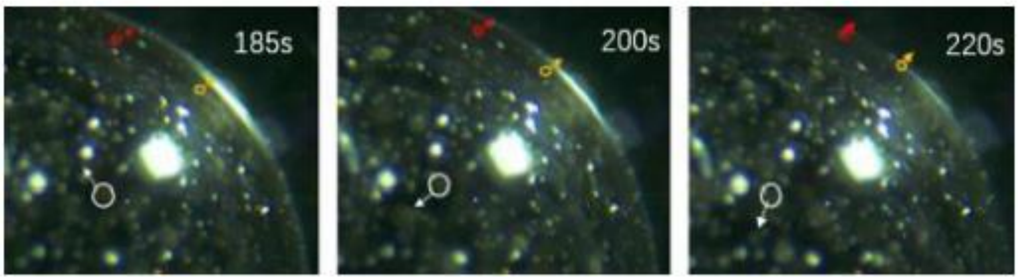

Figure 4-8 Micro-beads movement at the early stage at 25°C

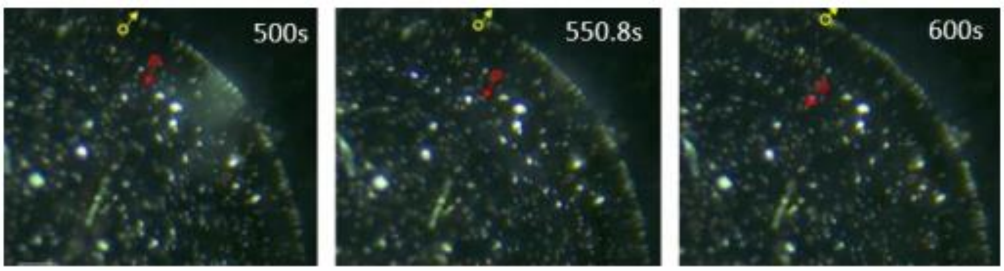

Figure 4-9 Micro-beads movement at final stage at 25°

4.3.3 Deposition pattern of Saline droplets and flow patterns of micro-beads at high temperature (55°C,70°C)

Figure 4-10 shows the final deposition pattern of saline droplet at high temperature. The ring shape structure can be observed in both patterns. Furthermore, a secondary ring is formed near the contact line. With increases of temperature, the size of crystals decreases, while quantity of crystals increases at the central area, and the particles tend to accumulate at secondary rings rather than central area. As Figure 4-11 shows, the temperature different further increases at high temperature than those at lower temperature.

At early stage, the flow motion of particles at high temperature is similar to that at normal temperature. The capillary flow dominates edge and gap region, which drives the particles to edge region. Meanwhile, the Marangoni flow is strengthened due to the larger temperature difference, which drives more particles from edge to apex of droplet. As shown in Figure 4-12, at the final stage, the tracked particle flow outward when t=90s, as when the particles is closed to the substrate it is majorly affected by Capillary flow. And when it reaches the edge area of the droplet(t=95s), it is pull upward by Marangoni flow and flow toward the apex then. However, as Figure 4-13 shows, as the height of the droplet is very low when evaporation is almost completed, the particles moving outward will easily collide with those moving inward and accumulate in the gap area, in turn, forming a secondary ring.

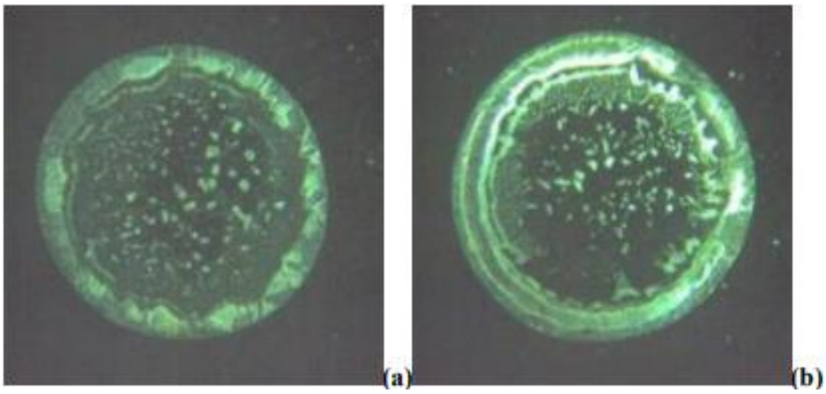

Figure 4-10 The final deposition pattern of saline droplet at high temperature(a) 55°C (b) 70°C

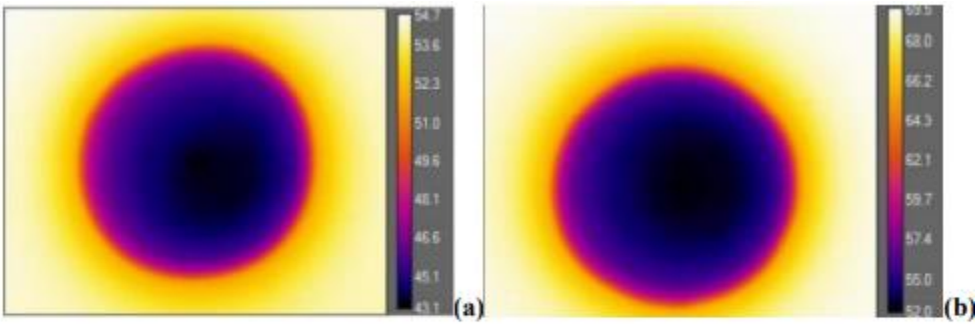

Figure 4-11 Surface temperature distributions (a) 55°C (b) 70°C

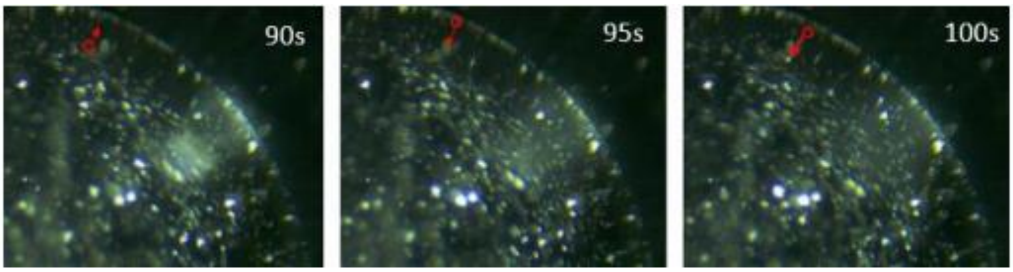

Figure 4-12 Micro-beards movement at middle stage at 55°

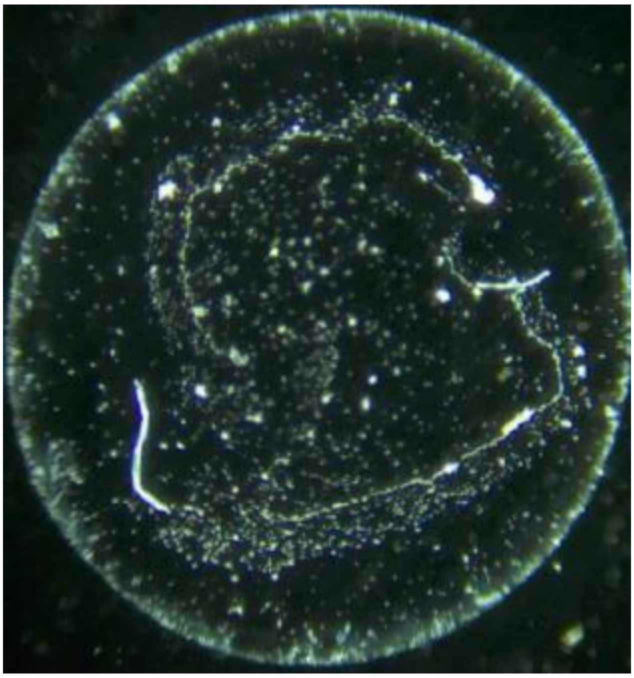

Figure 4-13 Final pattern distribution of Micro-beads at 55°C

4.4 Summary

In this chapter, the effects of substrate temperature on deposition patterns have been carried out. The results show that the coffee ring shape easily forms at high temperature substrate. With the increase of substrate temperature, the evaporation rate at the edge increases, resulting in more solvent to replenish the loss at the boundary of droplet, and accumulate at boundary, in turn, forming the coffee ring shape. Meanwhile, a secondary ring formed at gap area of deposit pattern when the droplet evaporates at high temperature substrate (55°C and 70°C). This attributes to the collision between the Marangoni flow and outward flow when evaporation is almost completed.

Chapter 5 Investigation on droplet Impacting on a Conical Structure

5.1 Introduction

Droplet impingement is one ubiquitous phenomenon widely existing in nature, which has been studied for more than 140 years since the works of Worthington in 1876[217]. This phenomenon has attracted great attention for many years, due to its importance in many industries such as spray cooling [218], surface spraying[219] inkjet printing[220] and meatal quenching[221]. The outcomes of the droplet impact on a solid surface can be characterized into three typical groups: deposition, splash, and rebound[98].

Luxford[222] summarized the conclusion of past research in 2005, dimensionless numbers can be used to describe the dynamics of droplet impact

$$Re = \frac{\rho D_0 V_0}{\mu} \tag{5.1}$$

$$We = \frac{\rho D_0 V_0^2}{\sigma} \tag{5.2}$$

$$Oh = \frac{\mu}{(\rho\sigma D_0)^{\frac{1}{2}}} = \frac{We^{\frac{1}{2}}}{Re} \tag{5.3}$$

Where Re , We , Oh and K are the Reynolds number, Weber number, Ohnesorge number and Mundo impact parameter, respectively. μ, σ, and ρ represent the viscosity, surface tension and density of water droplets. D_0 and V_0 denote the droplet initial diameter and impact velocity.

For the experimental studies on droplet impact dynamics, it can be categorized into three aspects: the maximum spreading factor β_{max} (where $\beta_{max} = D_{max}/D_0$, D_{max} is the maximum spreading diameter, D_0 is the initial diameter of water droplet), the splashing threshold and the effect of substrate properties.

When the impact velocity is relatively small, the droplet deposit on the surface without splashing. After the droplet contacting the surface, its vertical momentum is partially converted to horizontal momentum, driving the droplet to firstly spread outwards until it reaches a maximum spreading diameter D_{max}. Subsequently, the liquid lamella keeps static or retracts back depending on the interaction between the liquid surface tension, the inertia and the liquid viscous. The evaluation of β_{max} corresponding to empirical and theoretical models have been summarized[21][99][100][223][224][225], showing the commonly used formulas to fit the experimental/numerical results. When the impact velocity is high enough, the droplet splashing can be observed, as tiny droplets detached from the periphery of the lamellae and a number of secondary droplets were generated. However, there are two different types of splashing occurs: prompt and corona splashing. It is necessary to identify the splash thresholds which are used to define the minimum impact velocity leading to drop breakup and generation of secondary droplets. A prompt splashing happens when droplets impact rough surface, which releases tiny droplet directly from the periphery of the advancing lamella. Corona splashing is always observed on smooth surfaces, which liquid lamella is detached from the substrate and forms a bowl-like structure, subsequently breaking up into fine droplets. The splashing threshold have not been well understood, and the role of air and surface roughness need to be pinned down. In 1977, Stow and Hadfield[104] revealed that the droplet splashing can be strengthened by surface roughness. Xu et al.[109] observed the droplet impact on smooth substrates by adjusting the surrounding air pressure. They demonstrated that the corona splash can be suppressed by reducing the surrounding air pressure. Josserand[98] and Moreira et al.[111] reviewed and concluded the difference between the various proposed splashing thresholds. The current research is devoted to finding the critical values of K for various impact conditions and the effect of various factors on splash behaviours. However, the influence of various factor is not well understood and there is yet to be a universal correlation between the splash threshold and the factors[114].

With the development of different applications, enhanced surfaces were designed to meet diverse requirements rather than flat surfaces. T Many researchers have used both experimental and numerical methods to study droplet impact on surfaces with different structures such as pillars[117][118][119], ridges[120], cones [121][122] and spheres[123]. The droplets' dynamic behaviours are influenced by the redistribution of mass and momentum of during the process of droplets interaction with the structures. The droplet impacts on conical structures is relative less studied, which is one of the most representative geometric shapes, thus some research focus on the dynamics of droplet impacting on a conical substrate recently. Luo et al.[121] numerically and experimentally studied the droplet rebounding dynamics behaviours on superhydrophobic cone surface with different cone angles. They observed the three different phases depending on the selections of Weber number and cone angle. When the droplet impacts the surface with a low Weber number, the contact time decreases as the cone angle increase. With the increase of the Weber number, the contact angle does not affect the contact time and the reduction of contact time is about 54% compared with flat surfaces. Furthermore, a phase diagram was revealed for distinguishing three phases under various conditions and the critical We numbers were proposed for each phase. In 2017, Shen et al.[122] designed a dome convex superhydrophobic surfaces and investigated the bouncing dynamics of impacting droplets on the surface. They found that droplets rapidly bounce off with a 28.5% reduction in the contact time, compared with that on flat superhydrophobic surfaces. Recently,

However, these investigations focus on the droplet impingement on the superhydrophobic surface, which aim to reduce the contact time during the bouncing process of droplet and further increase the performance of applications of droplet impacting such as self-cleaning, anti-frosting and anti-icing. For spray cooling, the mechanism is more complex, which is not only affected by the surface geometry [226] but also affected by surface roughness [227].

In recent years, many investigations investigated the droplet impact on surfaces with different roughness and their results showed the droplet impacting behaviours are strongly affected by surface roughness. The earliest research on droplet impacting on dry surfaces was carried out by Stow and Hadfield et al.[104] in 1981. They revealed that the surface roughness affected the critical value K_c of droplet splashing. Mundo et at.[105] and Range and Feuillebois[106] proposed that the splashing threshold depends on the critical Weber number and is related to the surface roughness. Cossali et al.[131] developed an empirical correlation which demonstrated that corona splashing only happens on very smooth surfaces. With the increase of surface roughness, the corona splash transforms into prompt splashing. Roisman[113] studied droplet deposition and splashing on rough and porous surfaces. They found that the splash threshold is mainly affected by Weber number and substrate morphology, R_{pk}/R_{sm} (where R_{pk}, R_{sm} represents the average height of protruding peaks above roughness core profile and mean width of a profile element, respectively). Miguel et al. [133] experimentally investigated the water and ethanol droplets impacting on smooth hydrophilic, hydrophobic and superhydrophobic surfaces. They demonstrated that the maximum dynamic contact angles increase as the surface roughness increases and the splashing behaviours on substrates can be characterized by the roughness ratio R_{pk}/R_{sm} in his work. Tang et al. [134] observed various droplets impacting on flat stainless-steel surfaces with different surface roughness. They found that the droplet impacting behaviours change from spreading to splashing with increased surface roughness. Meanwhile, the critical value of $(We/Oh)^{1/2}$ was found to characterize the transition from spreading to splashing. Wang et al.[135] recorded the droplet impacting on surface with the help of digital inline holographic imaging. The surface roughness affects the diameter, velocity, angle, height and mass-loss rate of splashing droplet. In addition, they developed a new empirical correlation to characterize the secondary droplets.

In existing research, the combined effects of the surface roughness and conical structure on droplet impingement have not been considered. Therefore, an experimental investigation on droplet impact on 9 conical structures with different cone angles and surface roughness is carried out in this chapter. A high-speed camera was used to record whole impacting process and analyse the behaviours of droplets impacting on the conical structure, especially the effect of surface roughness on the droplet impacting behaviours. We expect that this work will not only extends the understanding of the droplet impacting against a conical structures but also provide fundamental guidance for related applications such as spray cooling.

5.2 Experiment set up

Figure 5-1 shows the schematic of the experimental apparatus. The droplet is generated by a syringe connected to a pump which can adjust the volume of the droplet. The pump has two pulleys on the back side which are attached to a vertical slide. The impacting velocity can be controlled by adjusting the height of the pump, and can be obtained by $v_0 = \sqrt{2gh}$, where g and h represent the gravity acceleration and the height between the syringe and cone tip, respectively. In our experiment, the initial droplet diameter is D_0= $3\pm0.05mm$ and impacting velocity v_0 ranges within 0.63 $\leq$ v_0 $\leq$ 3.49(m/s), corresponding to Weber number from 16 to 501(Here, We = $\rho v_0^2 D_0/\sigma$,where ρ is the density of water droplets, σ is surface tension, v_0 and D_0 are impact velocity and droplet diameter, respectively).The droplet falls vertically and impact the conical structure under gravity. The whole impact process is record by a high-speed camera (Phantom v12.1) at 6000 frames per second(fps) and two light sources are placed opposite the camera. The exposure time is set as 3 μs and the video has a resolution of 1024x769 pixels. A laptop is used to store all data for further analysis. The cone is made of aluminum and is manufactured with three cone angles (60°, 90°, 120°). To achieve different roughness(125μm,21.8μm and 0.2μm), the structures are polished by abrasive paper with the help of grinding and polishing equipment. The 125μm structure and 21.8μm structure were polished by 120pp and 800pp abrasive paper. The

0.2μm structure is polished by the hemp wheel(0.2μm) and it represents the relative smooth surface in this paper. There are 9 different aluminium conical substrates applied in the experiment. Fig. 5-2 shows the apparent contact angle of droplet on the flat aluminum substrate with different roughness, which is carried out via a contact angle meter(CAM200, KSV Instruments).

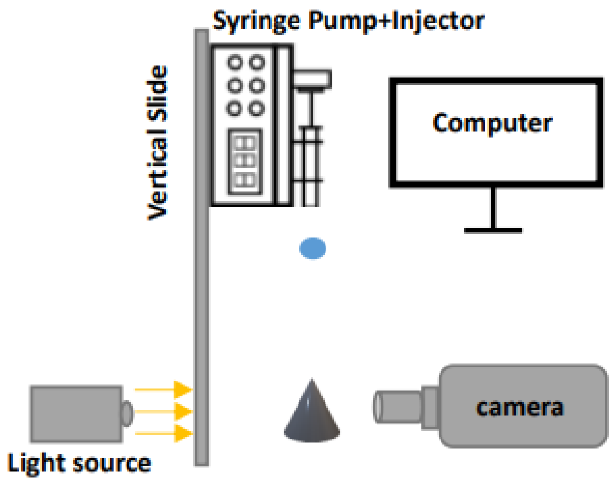

Figure 5-1 Schematics of experimental apparatus

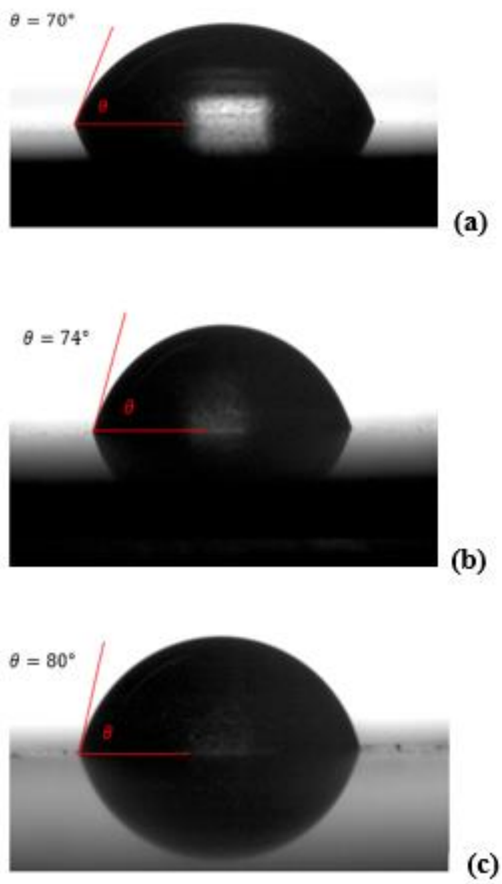

Figure 5-2 Surface contact angle of water droplet on aluminium substrate (a) droplet on smooth surface (b) 21.8µm (c) 125µm

5.3 Results and discussion

In this section, the typical images of a droplet impacting on the smooth cones and rough cones with varying Weber numbers and cone angles are shown. These images mainly demonstrate the beginning of impingement, spreading state, retracting state, relaxation stage and equilibrium state. The “t=0ms” is taken as the beginning of impingement and the dash-dot line denotes the instance of the droplet contacting the cone tip.

5.3.1 Droplet impacting on a relative smooth conical structure

Fig. 5-3 to Fig. 5-5 show the processes of droplets impacting on the smooth aluminium conical structure (R_a=0.2μm) with 60°, 90° and 120° cone angle at different Weber numbers. As the figures show, the outcomes of droplet impacting on different conical structures with different cone angles are similar. When the droplet contacts the cone tip, the horizontal fraction of momentum drives the droplet to firstly spread downwards along the side of the cone from the cone tip and this stage is dominated by inertial force. At a low Weber number (We=16, shown in Fig. 5-3 case **1**, Fig.5-4 case **4**, Fig.5-5 case **5**), the droplet reaches the maximum spreading radius R_{max} at t_{max} =17ms in case **1**. Subsequently, two boundaries can be observed. The upper boundary is formed by the penetration of water film due to the outward velocity vector at the cone tip. The lower boundary represents the rim of the lamella which is formed during the droplet spreading. After reaching the R_{max}, the rim liquid retracts slightly under capillary force with the velocity vector upward along the surface until it merges with the upper boundary which moves downwards along the surface of the cone under gravity and surface tension. Later an annulus is formed at t=30ms in case **1**, which subsequently oscillates for several periods of time and the liquid attains a final equilibrium spreading radius R_{equ} which is slightly smaller than R_{max}. The length between the R_{equ} and R_{max} represents the retracting amplitude. The initial kinetic energy of the droplet is partly dissipated by oscillation at relaxation stage. For droplet impacting a conical structure, the contact line advances in the spreading stage and recedes in the retracting state and settles in the equilibrium state.

When the Weber number becomes larger (We=258, shown in Fig. 5-3 case **2**, Fig.5-4 case **5** and Fig.5-5 case **8**), R_{max} increases and the spreading velocity is larger than those that when We=16 due to the larger initial vertical momentum, while the “finger-like” perturbations can be observed at the rim of the lamella in case **5** and case **8** during the spreading stage. The reason of the perturbations can be concluded by Rayleigh-Taylor Instability (R-T Instability). The instability occurs at the interface between two fluids of different density when the lighter fluid(air) is pushing the heavier one(water) and the instability increases as the impact velocity increases[228]. After reaching the R_{max}, the rim liquid retraction is stronger than We=16 due to increased capillary force. This is because according to the Young-Laplace equation, the capillary pressure can be obtained by:

$$p_c = \frac{2\sigma cos\theta}{r_c} \tag{5}$$

Where σ is surface tension, r_c represents the effective radius of the interface, θ is the wetting angle of the liquid on the surface. Therefore, the larger R_{max} increases the wetting area of spreading, resulting in a thinner rim of the lamella, thereby enhancing the capillary force. Meanwhile, the two boundaries also can be observed in the case **2**, **5** and **8**, which are more obvious than case **1**, **4** and **5**(We=16). Subsequently, both the upper and lower boundary start to retract until they merge into an annulus, whereafter the annulus separates into several droplets(t=40ms) due to the surface tension at the relaxation state rather than oscillation, which is different from the droplet impacting on a relative smooth conical structure at low We(We=16). The R_{equ} is much smaller than R_{max} due to the strengthen retracting stage when We =258.

As We further increased (We=501, shown in Fig.5-3 case **3**, Fig.5-4. case **6** and Fig.5-5. case **9**), R_{max} further increases and the spreading is faster, the spreading droplet reaches its R_{max} at t_{max}=8ms, 9ms and 8ms for case **3**, case **6** and case **9**, respectively. The fingering perturbations can be observed around the outer rim of the spreading lamella for all cases when We =501. During the retracting stage, the rim liquid tends to retract back while the “finger” is not able to be pulled back and is pinched off from the outer rim, resulting in secondary droplets which settle in the maximum spreading contact line, as shown by Fig. 5-3 case **3**(t=15ms), Fig.5-4 case **6**(t=12ms), Fig.5-5 case **9**(t=12ms). Because, with the increase of R_{max} , the thickness of rim of lamella decreases, which causes the rim liquid to more easily be detached from the outer rim of lamella [118] at higher We(We=501). This can be explained by Plateau-Rayleigh Instability (P-R Instability) as well. As the rim moves downwards along the surface, the perturbations grow with time resulting in an increased unevenness in the thickness of the rim. When approaching the maximum spreading radius, the capillary force caused by surface tension starts to overtake gravity and pull the rim backwards. However, the capillary force is not strong enough where the radius of rim is larger, thus, some of the liquid fails to be pulled back and detach from the rim, forming into secondary droplets. Subsequently, the residual rim liquid retracts toward the cone tip and tends to form back into an annulus, however most of the liquid is transferred to secondary droplets, and the retracted liquid forms some droplets distributed randomly between the maximum spreading contact line and upper boundary(t=26ms) in case **3**. For the case **6** and case **9**, the rim liquid retracts and merges with the upper boundary and form an annulus, whereafter the annulus separates into several droplets due to the surface tension before the equilibrium state.

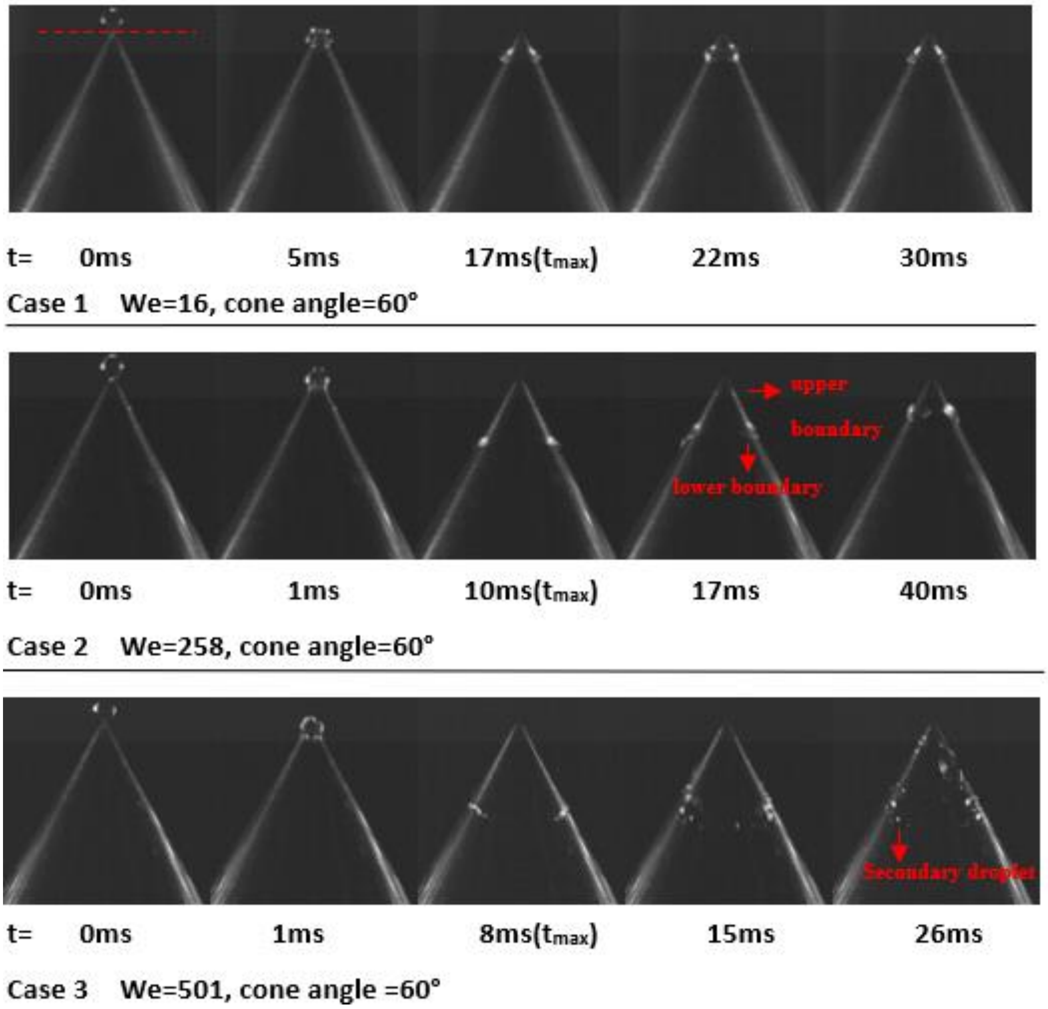

Figure 5-3 Images of a water droplet impacting on a relative smooth aluminium conical structure with 60° cone angle at different Weber numbers

t= 0ms 5ms $14ms(t_{max})$ 18ms 30ms

Case 4 We=16, cone angle=90°

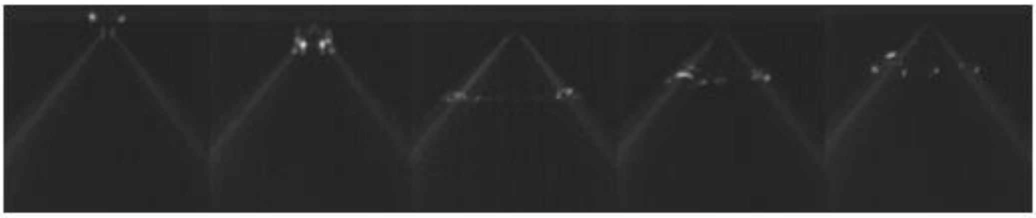

t= 0ms 1ms $9ms(t_{max})$ 23ms 40ms

Case 5 We=258, cone angle=90°

t= 0ms 1ms $9ms(t_{max})$ 12ms 26ms

Case 6 We=501, cone angle =90°

Figure 5-4 Images of a water droplet impacting on a relative smooth aluminium conical structure with 90° cone angle at different Weber numbers

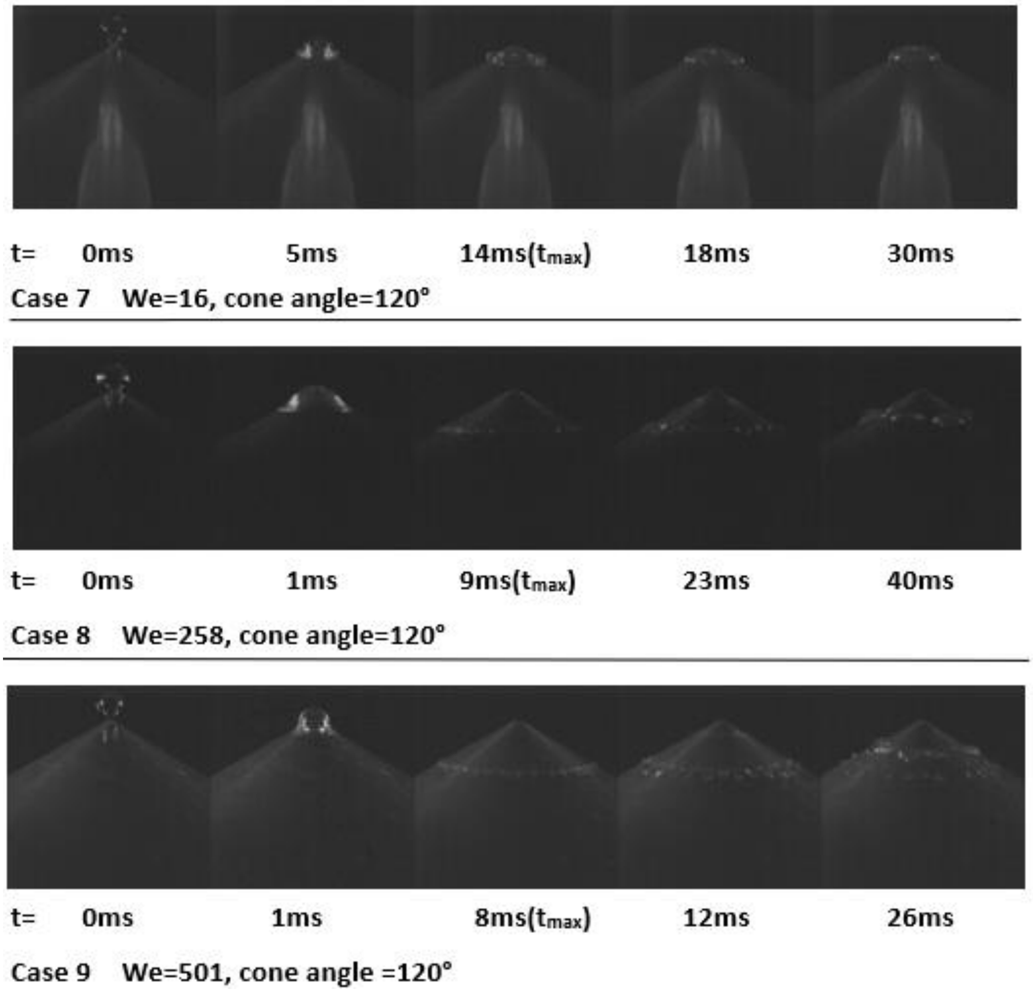

Figure 5-5 Images of a water droplet impacting on a relative smooth aluminium conical structure with 120° cone angle at different Weber numbers

5.3.2 Droplet impacting on a rough conical structure

Fig.5-6 and Fig.5-7 show the images of a water droplet impacting on a rough aluminum conical structure with different surface roughness and cone angle=60°. As the figures show, the outcomes of droplet impact a rough surface are similar to those that impacting a relative smooth conical structure. The spreading state, retracting state, relaxation stage and equilibrium state also occur during the impacting process of Case **10**-Case **15**. When the droplet impacts rough conical structure, the droplet spreads downwards along the side of the cone from the cone tip under inertial force until it reaches the maximum spreading radius

R_{max} which increases as the We increases. Subsequently, the rim liquid retracts towards the cone tip and merges with the upper boundary which is formed by the penetration of droplet film. Besides, the secondary droplets also can be observed when Weber number is 501(Fig.5-6 case **12**, Fig.5-7 case **15**).

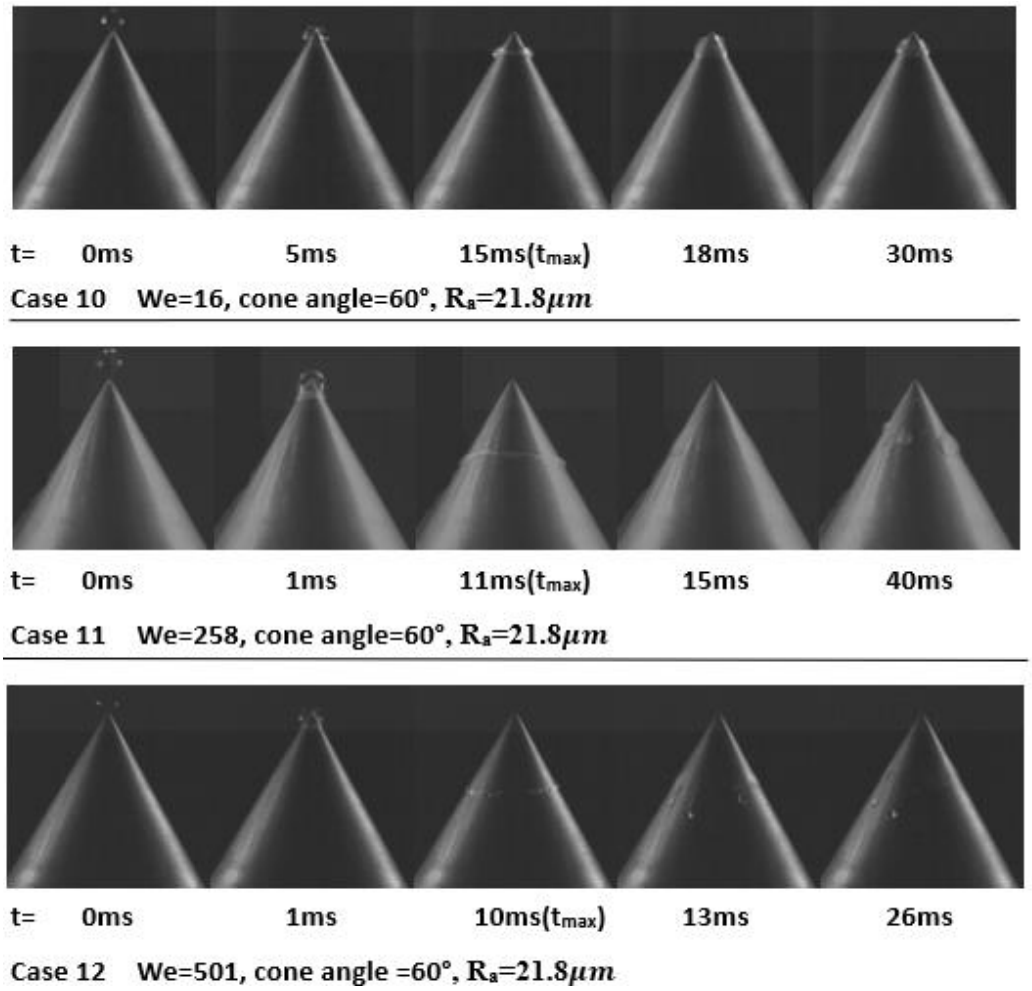

Figure 5-6 Images of a water droplet impacting on the 21.8μm aluminium conical structure with 60° cone angle at different Weber numbers

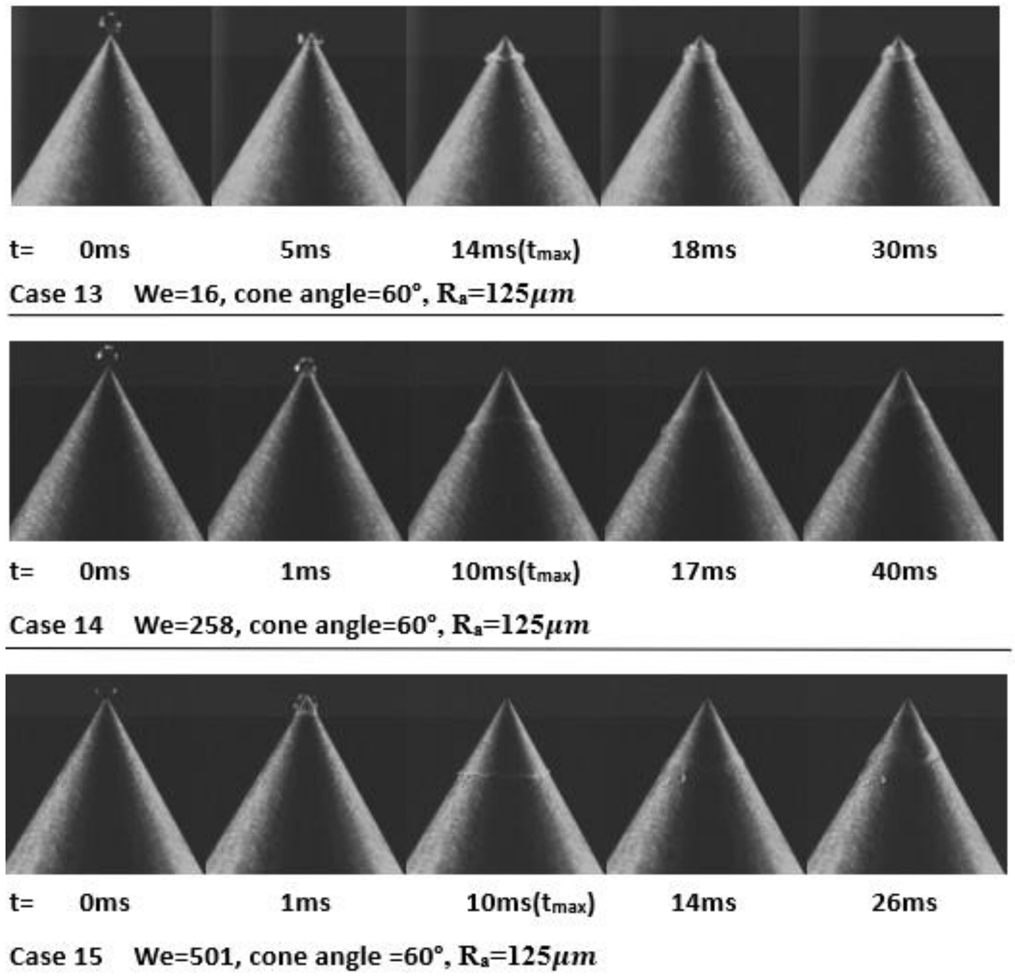

Figure 5-7 Images of a water droplet impacting on the 125μm aluminium conical structure with 60° cone angle at different Weber numbers

Specially, when We = 16, cone angle =120°, the cone tip is not covered by the liquid on the smooth conical structure(case **7**) at the final equilibrium stage as shown in Fig. 5-8. In the case of roughness = $21.8\mu m$ (case **16**) and roughness =$125\mu m$ (case **17**), the cone tip is covered by the liquid at the final equilibrium stage due to the contact angle of the droplet on rough surfaces(CA=74° and 80°, respectively for $R_a = 21.8\mu m\, and\, 125\mu m$) is larger than that on smooth surfaces (CA=70°), while the maximum spreading factor decreases with the increased of roughness, making it more likely for the droplet to wrap the cone tip.

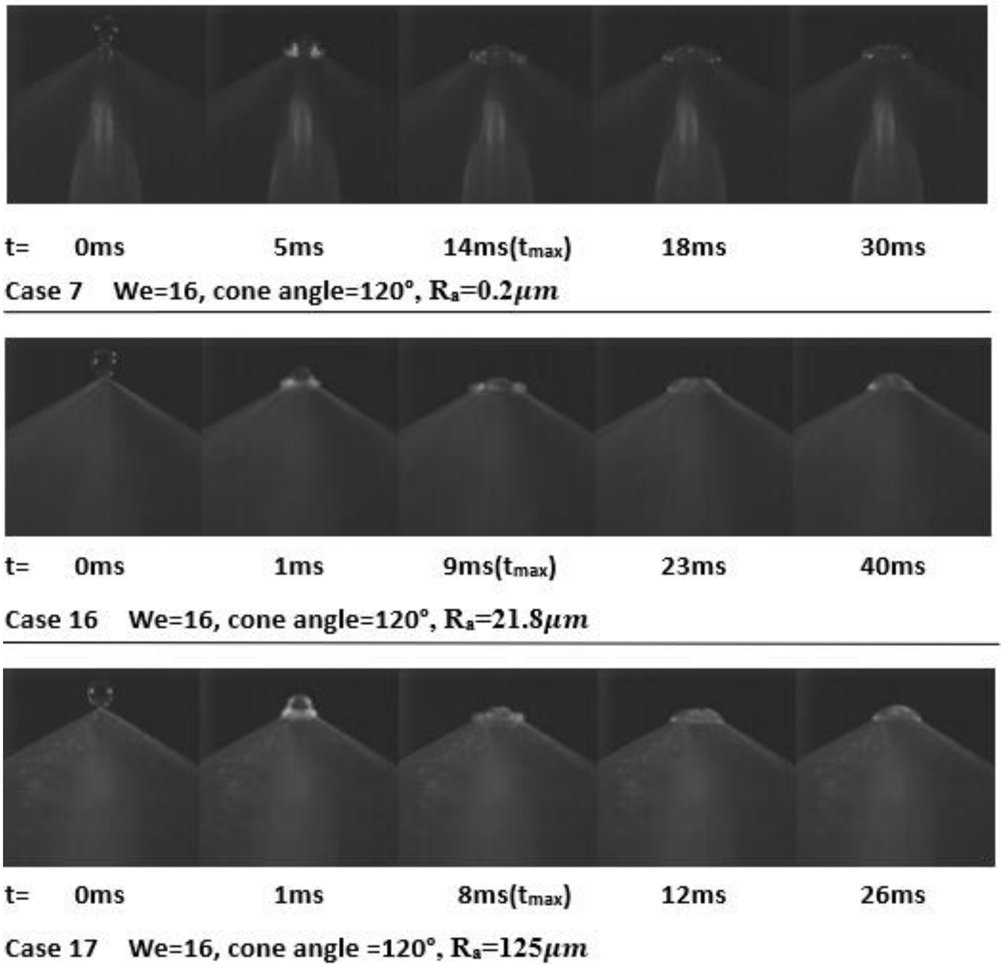

Figure 5-8 Images of a water droplet impacting on the aluminium conical structure with different surface roughness for We=11 and cone angle = 120°

5.4 Impact dynamic

5.4.1 Dynamic process analysis

Due to the visual difference between the droplet impacts a smooth conical structure and a rough conical structure is not obvious, in order to further analyse the effect of We number, cone angle and surface roughness, the droplet impacting dynamics is quantified by the variation of the droplet spreading factor ($\beta = R/R_0$,where R is the spreading radius, which is defined as the parallel distance along the cone surface between the cone tip and the contact line; R_0 represents the droplet initial radius) as a function of the impacting time t for all test cases are presented in below. The variation of β represents the movement of the outer rim of the lamella not considering the secondary droplets. The figures only describe the droplet spreading factor during the spreading stage and retraction stage, because the variation of the spreading factor after the retraction stage is not obvious.

Fig 5-9 depicts the variation of droplet spreading factor β of droplet impacts a smooth conical structure with different cone angle. With increasing We, the curve of β becomes steeper during the spreading stage, which indicates a larger spreading velocity. Meanwhile, the β_{max} increases significantly as We increases. As Fig. 5-9 (a) shows, when the cone angle is 60º, the largest maximum spreading factor is 8 when We=501, and the smallest one ($\beta_{max} = 3$) can be obtained when We=16. The largest maximum spreading factor is 6.67 and 6 at We =501 and the smallest β_{max} is 2.8 and 2.6 at We=16, when the cone angle is 90º and 120º, respectively (Fig. 9(b)(c)). According to Clanet et al., Roisman et al. and Yarin[229][230][231], they proposed theoretical models for predicting the evaluation of β_{max}, their results show that the β_{max} ranges from 1.25 to 5 when droplets impacting on a flat surface. However, the β_{max} is higher than 5 when We is 501 in our experiment. This may attribute to a smaller momentum loss when the droplet impacts on a conical structure, as the conical structure redirects the way the droplet moves in a less steep way. Therefore, the β_{max} is also affected by the geometry of the substrate. The "finger-like" perturbations can be observed when the We is higher than 258, which is induced by the R-T Instability and increases as the impact velocity increases.

When the We reaches 501, the droplet splashing appears and the secondary droplets are detached from the outer rim of the lamella, which is attributed to the

P-R Instability and larger inertial force. After the spreading stage, the retracting amplitude increases with the increase of We. For the conical structure with different cone angles at We = 16, the retracting amplitude is neglectable during retracting stage. As the We reaches 258, the retracting amplitude increases to 0.97~1.6. When the We further increases to 501, the retracting amplitude ranges from 2~2.19. The larger retracting amplitude is mainly attributed to the stronger capillary force due to the thinner rim of the lamella at higher We. Meanwhile, droplet splashing occurs at We=501, resulting in the formation of secondary droplets and volume reduction of the rim of the lamella, and further decreased rim thickness. Therefore, the rim of the lamella can be pulled back more easily due to its lighter weight and stronger capillary force when the impact outcome is splashing.

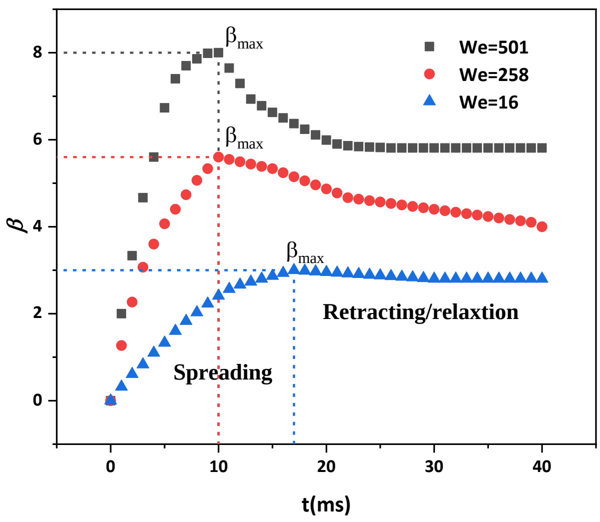

(a)

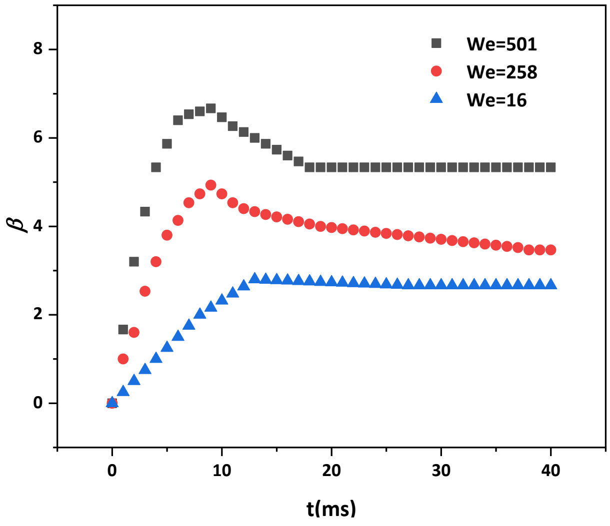

(b)

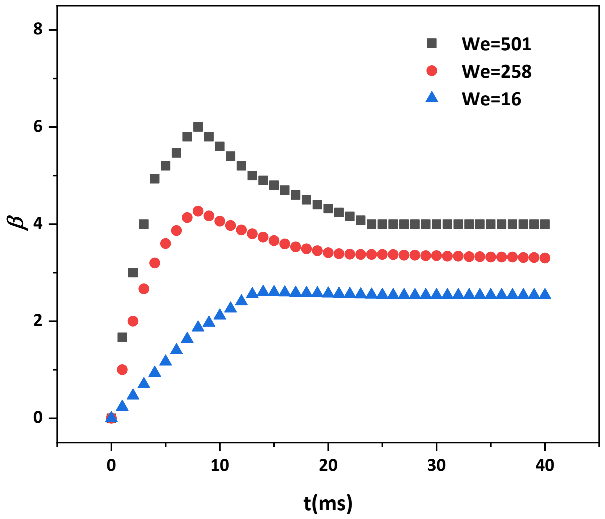

(c)

Figure 5-9 The variation of droplet spreading factor of droplet impacts on a relative smooth conical structure(Ra=0.2µm) as a function of time for different conical structure with various cone angle;(a) cone angle = 60°, (b) cone angle=90° ,(c) cone angle=120°.

Fig.5-10 shows the spreading factor of droplets impacting a smooth conical structure with different Weber number as a function of time. At low We(We=16, Fig.10(a)), the variation of droplet spreading factor for all cases are similar. The β_{max} is 3, 2.8 and 2.6, when the cone angle is 60°, 90° and 120° respectively. The effect of cone angle on β_{max} is not obvious at low We due to the smaller initial momentum. When We=258 and We=501(Fig.5-10(b)(c)), with the increase of cone angle, the variation of droplet spreading factor becomes steeper during spreading stage, which means a larger spreading velocity. Meanwhile, the maximum spreading factor increases with decreases in the cone angle. For We=258, the β_{max} is 5.6, 4.93 and 4.27 when the cone angle is 60°,90° and 120° respectively. For We=501, the β_{max} is 8, 6.67 and 6.13 when the cone angle is 60°, 90° and 120° respectively. This is mainly attributed to the vertical fraction of momentum that increases with decreasing cone angles, which means a larger inertia force drives the droplet spreading, thereby increasing the maximum spreading factor β_{max} . Therefore, the varying cone angle redistributes the momentum transfer during the impacting process.

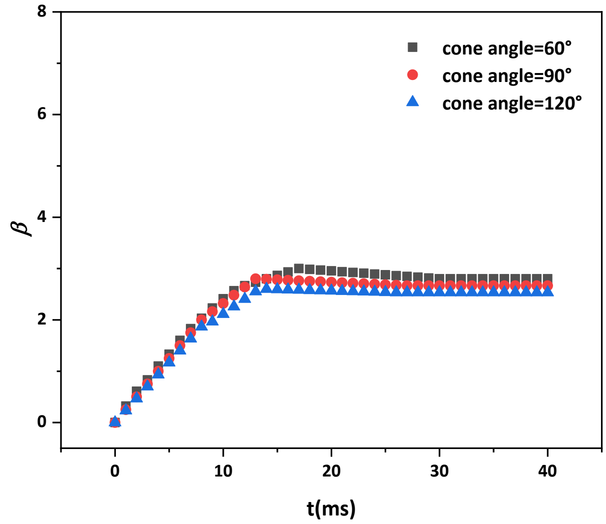

(a)

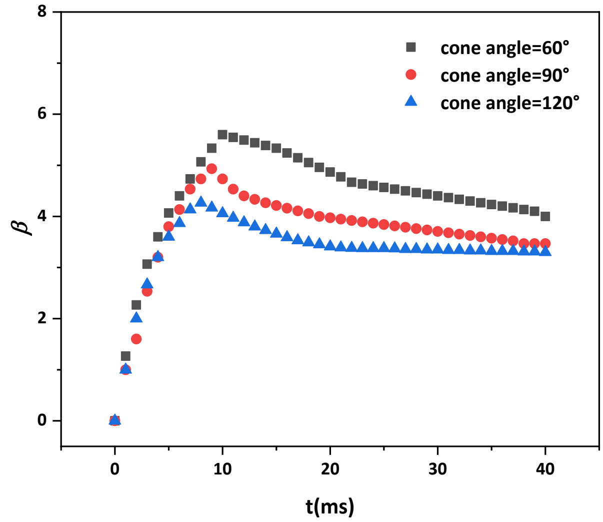

(b)

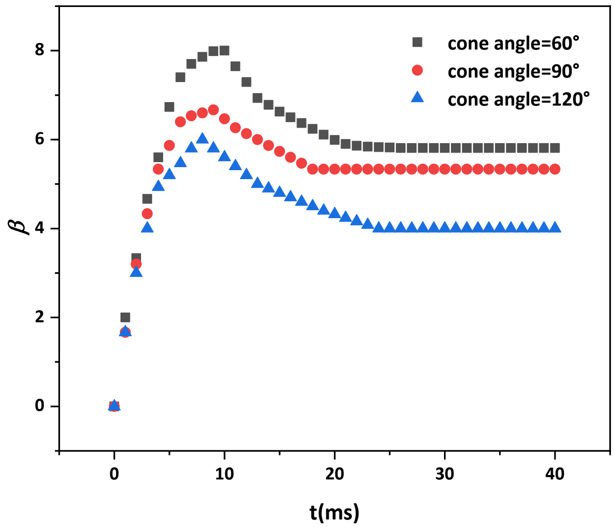

(c)

Figure 5-10 The variation of droplet spreading factor of droplet impact on a relative smooth conical structure(Ra=0.2μm) with different Weber number as a function of time;(a) We = 16, (b) We=258,(c) We=501.

Fig.5-11 shows the effect of surface roughness R_a on the β for water droplet impact on a conical structure with different R_a and cone angle =60°. The maximum spreading factor β_{max} of droplet impact on a smooth surface is larger than those that impact on a rough surface for all case in Fig.11. A larger R_a results in a smaller β_{max}. In addition, the retraction amplitude is weakened at rough surface when the We reaches 258 and 501. As Fig.5-11(b)(c) shows, the curve of evolution of droplet spreading factor of droplet impact on a smooth surface is steeper than those that impact on a rough surface after the spreading stage. During the spreading stage, the friction increases as the R_a increases, which hinders the motion of the contact line resulting in more energy loss and decreasing the maximum spreading factor. For the retracting stage, the retracting liquid need to overcome the extract friction on a rough surface, leading to the decrease of retracting amplitude.

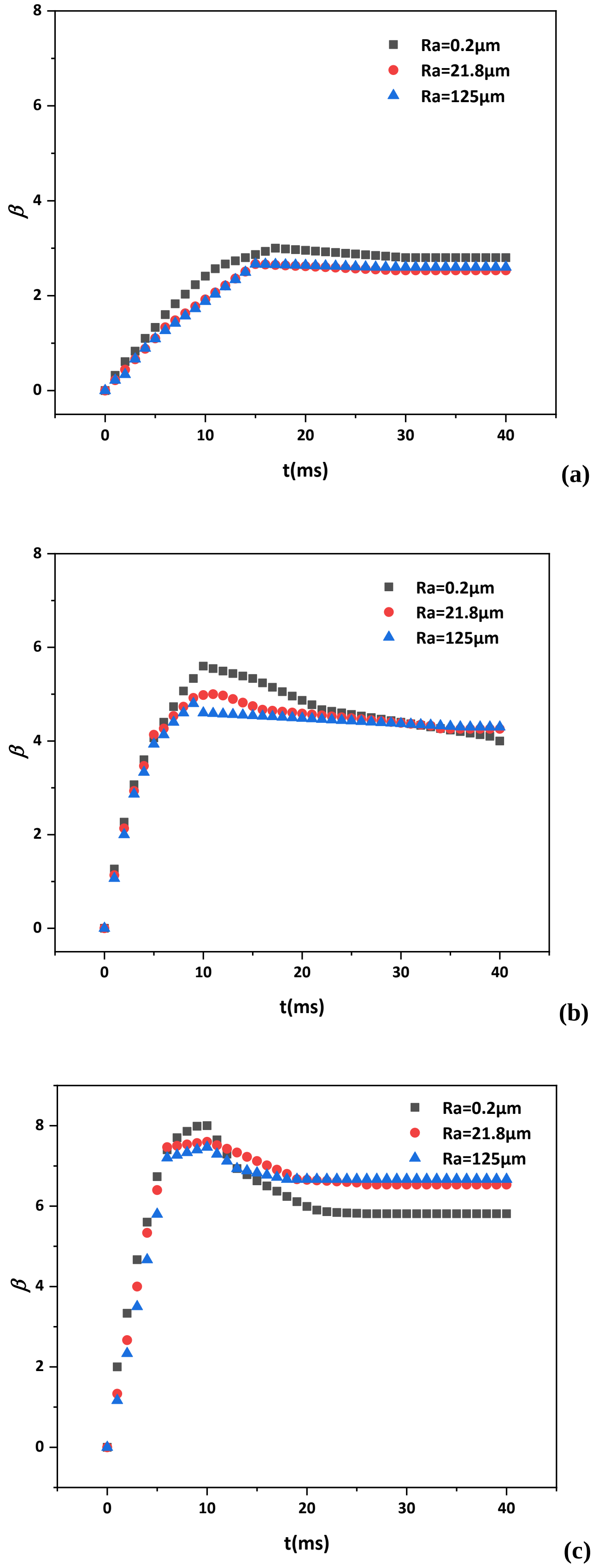

Figure 5-11 The variation of droplet spreading factor of droplet impacts on a conical structure with different R_a and cone angle =60° as a function of time;(a) We = 16, (b) We=258,(c) We=501.

5.4.2 Splashing threshold

The critical Weber number We_{cr} for the transition from spreading to splashing is one of significant importance for the spray impingement. First, the chamber walls of gasoline direct injection engines were impacted by spray, the splashing droplets that affect the mixture formation ,resulting in the emission of unburned hydrocarbon. Second, splashing affects the nucleation site generation and local film behaviours, which can enhance the heat transfer ability of spray cooling[232].

Fig. 5-12 shows We_{cr} for the transition from spreading to splashing, as a function of the roughness parameter R_a . It indicates that the splashing behaviours are strongly enhanced by the increase in surface roughness and decrease in cone angle, especially for the conical structure with R_a between the 0.2μm to 21.8μm. There are two reasons why surface roughness will enhance droplet splashing.

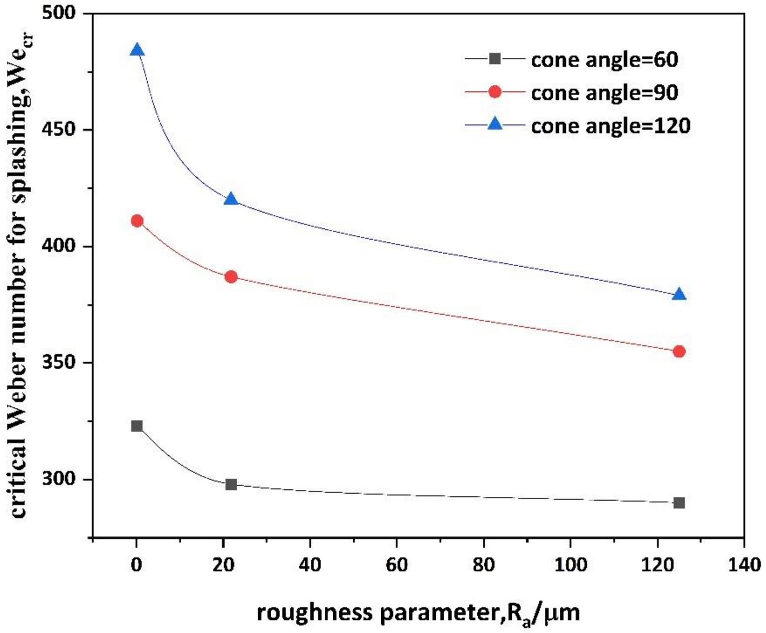

Figure 5-12 The variation of the critical Weber number for splashing, with the surface roughness parameter, R_a/µm of various cone structure with different cone angle

First, Because the roughness hinders the retracting liquid during the retracting stage, resulting in the generation of secondary droplets, promoting the splash. Fig.5-13 shows the formation of the secondary droplets. The rim liquid is still attached to the rim of the lamella when it reaches the maximum spreading radius. Subsequently, the rim of the lamella starts to retract towards the cone tip. However, some of the liquid where the thickness of the rim is larger cannot overcome the friction force and gravity, and stay static, resulting in the formation of secondary droplets.

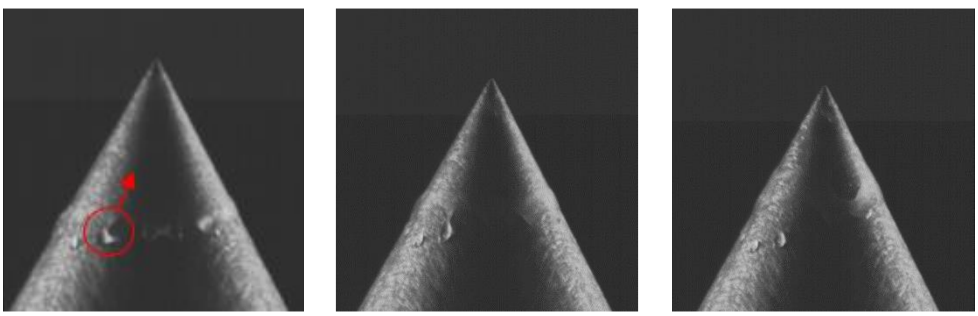

Figure 5-13 Snapshot of the formation process of secondary droplets

Second, Hao et al.[233] reported that the reduction of the wetted area promotes the water droplet splashing. As Fig.5-11 shows, the maximum spreading factor of droplets impacting the rough surface is smaller than those that impacting the smooth surface, which means the wetted area of a rough conical structure is smaller than the smooth substrate. Therefore, the increase of surface roughness decreases the wetted area resulting in the enhancement of droplet splashing.

In addition, the decreased cone angle also can promote droplet splashing. As Fig.5-12 shows, the We_{cr} reduces from 379~484 to 290~323 when the cone angle decreases from 120° to 60°. Because the vertical component of the momentum which drives the droplet spreading increases with the decrease of cone angle, resulting in larger inertia of outer rim around lamella, thus the liquid is detached more easily from the rim of the lamella and generate secondary droplets.

5.5 Summary

In the present research, the droplet impacting dynamics and evolution of droplet spreading factors on aluminum conical structures have been studied. The whole process of droplet impingement on different conical structures are recorded by high-speed camera. When the droplet contacts the cone tip, it firstly spread downwards along the side of the cone from the cone tip until it reaches maximum spreading factor β_{max}. After reaching the β_{max}, the rim liquid retracts back towards the cone tip and tends to form an annulus. In order to further analyses the droplet impacting dynamics, the variation of the droplet spreading factor β is used to quantify the spreading behaviours. The β_{max} is strongly affected by the We, surface roughness and cone angle, which increases with increasing We, and decreasing surface roughness and cone angle. At higher We, the droplet impact outcome changes from spreading to splashing. The critical Weber number We_{cr} for transition from spreading to splashing can be decreased by increase in the surface roughness and decease in the cone angle. Our findings extended the understanding of the droplet impacting on a conical structure with different cone angles and surface roughness, which provide a fundamental guide for related applications such as spray cooling.

Chapter 6 Experimental Investigation on thermal performance of PHP with MEPCM suspension

6.1 Introduction

Many research have been done to enhance the thermal performance of PHP by applying different working fluid such as mixed fluids [234][235], nano fluids[236][237][238], refrigerant[239]. Thermophysical properties of working fluids is one of the important factor affects the thermal performance of PHP. There are 2 common method to vary the thermophysical properties of working fluid, i.e., adding the mixed fluid, nanofluids. In the recently, some research explored novel cost-effective working fluids such as micro encapsulated phase change material suspension(MEPCMS). The MEPCMS can absorb and release a large amount of latent heat during its phase change process thus increase the thermophysical properties of working fluid. Wang et al.[240] proposed a novel method for improving the thermal performance of PHP by adding encapsulated phase change materials to working fluid of PHP. Their results show that the thermal performance of PHP can be improved by adding FS-39E microcapsule and Al_2O_3 nano-particle to working fluid under various conditions. The working fluid with FS-39E shows best performance when using vertical bottom heat mode and best concentration is 1 wt%. Li et al.[241] studied the anti-dry-out ability of PHP with MEPCM by using the Computational Fluid Dynamics(CFD) technique. They found that the anti-dry-out ability, start-up performance and heat transfer performance of PHP can be improved by adding MEPCM suspension within a certain phase change temperature. The optimal phase change temperature range should be selected around the evaporation section temperature when the PHP transforms from the circulating flow stage to the dry-out state. Heydarian et al.[242] used a mixture of water and paraffin nanocapsules as working fluid in their study. Their results show that The thermal performance of PHP can be increased by adding paraffin nanocapsules in all investigated orientations. The lowest thermal resistance can be obtained in a vertical orientation. Shi et al.[243] experimentally investigated the start-up and running performance with 0.5% mass concentration MEPCM suspension in a PHP. Their results show that the start-up performance of PHP charged with MEPCM suspension is unstable at lower heat input(30-90W), while the start-up runs stably when the heat input increasing to 120W. Meanwhile, the thermal performance of PHP increases with decreasing the filling ratio from 70% to 35%. At present, there are just a few visualization studies on thermal performance of PHP with MEPCM suspension, which can further explain the mechanisms of thermal conductivity enhancement in MEPCM suspension.

In this study, a guideline for the best working condition of MEPCM suspension working fluid in a pulsating heat pipe is developed based on an experimental investigation. Experiments are conducted using a glass PHP, which allow for internal flow visualization. The MEPCM suspension is selected for the working fluids, which contains paraffin micro-capsule. The thermal performance of PHP is evaluated under various heat input, filling ratio and working fluid concentration in order to observe the best working condition of the novel working fluid. Furthermore, with the aid of a high-speed camera, the bubble generation, flow pattern and the typical fluid oscillatory motion are recorded. By combining the simultaneous visual and thermal investigation is conducted to further understand the thermo-hydrodynamics involved into the operation of a PHP with microcapsule working fluid.

6.2 Experiment set up

Figure 6-8 shows the schematic of the experimental set-up. The heat pipe is fully made of Duran borosilicate 3.3 glass capillary tubes. The inner and outer diameter of the glass tube are 1.5mm and 4mm, respectively. The total length of PHP is 280mm, and the lengths of the evaporator section, the adiabatic section and the condenser section are 100mm,80mm and 100mm, respectively. The evaporator section of the PHP is heated by Nichrome Wire of which the diameter is 0.345mm and the resistance is 11.486ohm/m. It’s wrapped on the outer wall surface of the tubes. The heat input was set to 30W, 40W, 50W, 60W, 70W, 80W and 90W which is achieved by an DC power supply (KEYSIGHT AC6902A). The condenser section is cooled by a transparent cooling box which is connected to a water bath. The inlet temperature of cooling water is maintained at 20°C with ±1°C fluctuation. The motion of vapour bubbles and liquid slugs are recorded by a CCD camera (BASLER a2A1920-160uc PRO). The pressure of PHP is gauged by a Druck pressure sensor (RS PRO-7975037) and the PHP is evacuated by a vacuum pump(CPSVP8D).

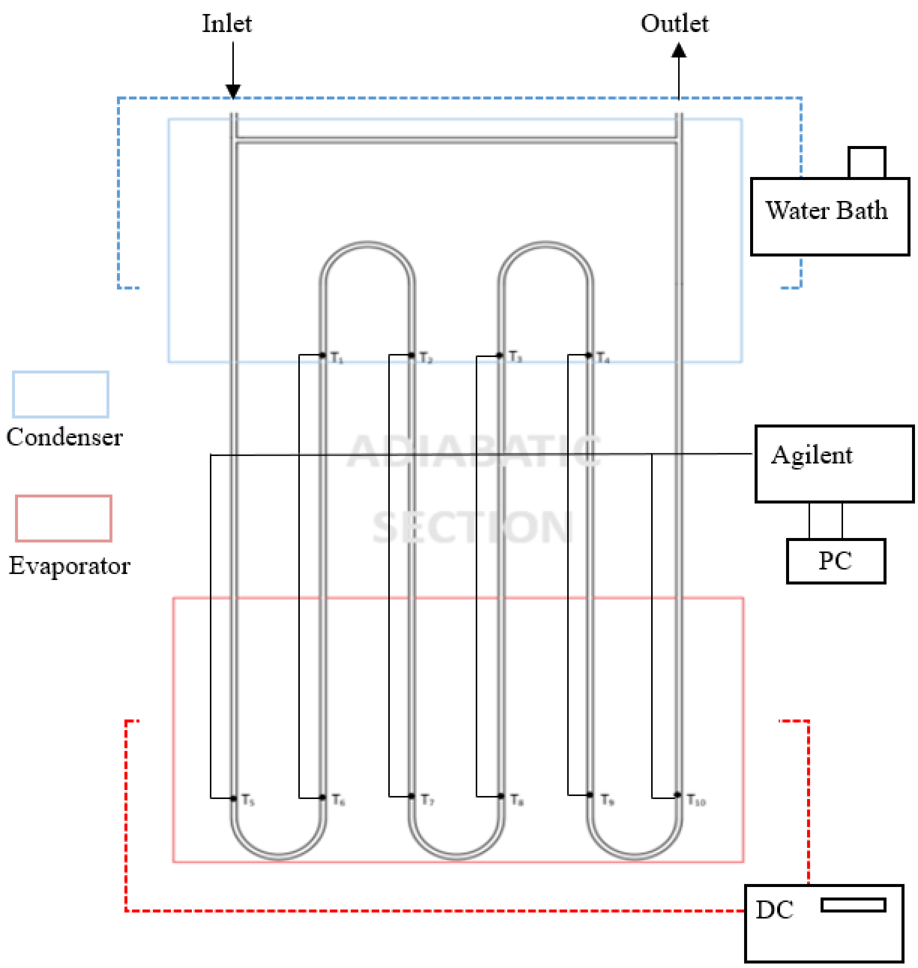

Figure 6-1 Schematic of the Experiment Set Up

There are 10 K-type thermal couples distributed as shown in Figure 6-9 to measure the temperature of the evaporator and condenser section of the PHP. Four thermocouples T_1 to T_4 are distributed in different tubes to measure the average temperature of evaporator. T_5 to T_{10} are placed in the corresponding tubes to give an average value of temperature of condenser. Additionally, there are 2 thermocouples T_{in} and T_{out} placed at the inlet and outlet of cooling box and measure the inlet and outlet temperature of water. A data acquisition instrument (Agilent 34970A) is used to record all temperature data and is connected to a PC for data monitoring and analysis. Filling ratios were 20%, 40%,60% and 80%. In order to determine the amount of working fluid to use, the total volume of the pipe is measured, which is 13ml. The vertical heating was used for all test conditions, which means the inclination angle of PHP was maintained at 90°.

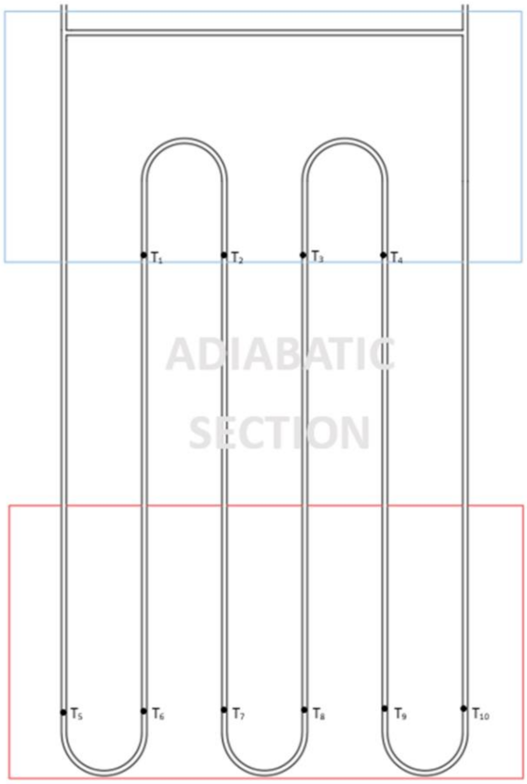

Figure 6-2 The location of thermocouples

6.3 Preparation of working fluid

In this experiment, the working fluid was deionized water (DI water) and MEPCM suspension. The MEPCM with paraffin as core and melamine as shell was prepared. The phase change temperature of MEPCM is 43°C. The MEPCM's particle size and its phase change latent heat is 20μm and 180J/g, respectively. The MEPCM were added into DI water with 5 different weight concentrations: 1wt%, 2wt% 3wt%, 4wt% and 5wt%. The dispersion process was achieved by magnetic stirrer (HYCC MX-8K) and sonicator (GEX 750). The stirring rate and ultrasonic vibration frequency was set to 300RPM and 40KHz. The stirring time was 24h and 0.2wt% Tween 80 surfactant is added into the suspension during stirring process, which can improve the dispersion stability of MEPCM suspension [244]. Then, the mixed solution is treated by ultrasonic vibration for 2h to improve its stability.

6.4.3 Viscosity measurement

The viscosity of each working fluid is determined using Ostwald Viscometer. The viscosity can be calculated by below equation:

$$\mu_2 = \frac{\rho_2 t_2}{\rho_1 t_1}\mu_1 \tag{6.1}$$

Where ρ_1 and ρ_2 represents the density of DI water and test sample, respectively. μ_1 is viscosity of water. *t* represents the time it takes for the fluid to flow through the measuring length of the viscometer. The viscosity of the working fluid is shown in table 6-1. With the increasing of the concentration of MEPCM, the viscosity of working fluid increases.

Table 6-1 Viscosity of each working fluid

Working Fluid	**Mean time(t)(Sec.)**	**Density(ρ)(g/ml)**	**Viscosity(μ)(Centipoise)**
Water	$t_1 = 4.54s$	0.997 g/ml	1.0 cp
1wt% MEPCM suspension	$t_2 = 4.72s$	0.984 g/ml	1.02 cp
2wt% MEPCM suspension	$t_2 = 4.93s$	0.975 g/ml	1.07 cp

3wt% MEPCM suspension	$t_2 = 5.23s$	0.97 g/ml	1.12 cp
4wt% MEPCM suspension	$t_2 = 5.56s$	0.964 g/ml	1.18 cp
5wt% MEPCM suspension	$t_2 = 5.73s$	0.960 g/ml	1.21 cp

6.4 Data processing

The thermal resistance R_{th} can be used to assess the thermal performance of the PHP, which can be obtained from the following equation

$$R_{th} = \frac{T_e - T_c}{Q} \tag{6.2}$$

where R is the thermal resistance of PHP; Q is the heat input; T_e and T_c are the average wall temperatures of the evaporator and condenser, respectively. T_e and T_c can be calculated by

$$T_e = \frac{1}{6}\sum_{i=1}^{6} T_i \tag{6.3}$$

$$T_c = \frac{1}{4}\sum_{i=1}^{4} T_i \tag{6.4}$$

Where T_i represents average temperature from thermocouple measuring point i of the PHP.

6.5 Uncertainty analysis

The uncertainly of the experiment mainly comes from the instrument error and measurement error. The temperature data of this experiment were measured by K-type thermocouples and its margin of error is ± 0.1 ℃. The measurement margin of error of Agilent-34980A data acquisition module is ± 0.1 ℃ and the minimum temperature is 18 ℃. The maximum temperature error can be determined by

$$\frac{\delta T}{T} = \sqrt{\left(\frac{\delta T_1}{T_{min}}\right)^2 + \left(\frac{\delta T_2}{T_{min}}\right)^2} \qquad (6.5)$$

In this work, the electric voltage and current are obtained by AC power supply, whose display accuracy is 1%. The range is 0–55 V and 0–2 A for the electric voltage and current, respectively. When the heat input is 40 W, the voltage and electric current is obtained as 34 V and 1.17A, respectively. Therefore, the uncertainty of the input power can be obtained as follows:

$$\frac{\delta Q}{Q} = \sqrt{\left(\frac{\delta U}{U}\right)^2 + \left(\frac{\delta I}{I}\right)^2} \qquad (6.6)$$

The uncertainties of the thermal resistance can by calculated by:

$$\frac{\delta R}{R} = \sqrt{\left(\frac{\delta Q}{Q}\right)^2 + \left(\frac{\delta T_C}{T_e - T_C}\right)^2 + \left(\frac{\delta T_e}{T_e - T_C}\right)^2} \qquad (6.7)$$

Table 6-2 Summary of Experimental Uncertainties

Measurement parameters	**Uncertainty**
Heat input	2.3%

Thermal resistance	2.03%
Temperature	0.78%

6.6 Experimental result analysis

In this chapter, the effects of filling ratio, concentration of working fluid and heat input on the thermal performance of PHP are investigated. The influence of the filling ratio was tested for 4 values, equaling to 20%,40%.60% and 80%. Six different working fluid were prepared, respectively 1wt%, 2wt%, 3wt%, 4wt% and 5wt% MEPCM suspension and DI water. The heat input varies in a range of 30W-90W. By changing those parameters in totally there were 168 experiments carried out. Each experiment was performed over a 20 minutes period.

The PHP failed to start-up for all condition when the heat input is 30W. Meanwhile, the directional flow does not occur regardless of working fluid type in the case of FR =20% when the heat input was high than 70W(dry-out), while the temperature was constantly increased when continuously applied heat input. For safety considering, the power supply was off when the local temperature exceeds 120°C. Therefore, the data analysis didn't contain the case of heat input equal to 30W and local temperature exceed 120°C.

6.6.1 Effect of filling ratio on thermal performance of PHP

When the PHP with a lower filling ratio, average length of liquid plug is smaller, pulsating velocity and amplitudes are higher [245] and less driving force is needed to make the working fluid oscillate in the PHP, which increase the thermal performance of PHP. Although, the thermal performance increases due to the high oscillation velocity and amplitudes and less driving force requirement, the small amount of the working fluid limits the heat transfer capability of the PHP with lower filling ratio. In the case of FR=20%(Figure 6-10), the thermal resistance has not significant decreased when the heat input higher than 60W due to the dry-out phenomenon which occur at lower filling ratio and higher heat input. The directional flow does not occur, and the temperature was constantly increasing due to all working fluid remains at the condenser section. The dry-out phenomenon limits the heat transfer performance of PHP at lower filling ratio, which is induced by the boiling heat transfer intensive at higher input power. On the contrary, more driving force was needed to oscillate the working fluid and accompanying with larger heat transfer capability at higher filling ratio. Meanwhile, the movement of the working fluid at higher filling ratio was weakened by the restriction of the generation and growth of bubbles due to the smaller vapor phase space in PHP, which limit the heat transfer performance of PHP.

The thermal resistance of PHP with various heat input in the filling ratio range of 20%-80% are shown in Figure 6-10. It could be clearly found that the thermal resistance of the PHP with DI water, 1wt% ,2wt%, 3wt%. 4wt% and 5wt% MEPCM suspension is influenced by the filling ratio. The best thermal performance of PHP was obtained when the filling ratio of the PHP was 40% for all working fluid concentration. Meanwhile, the thermal performance decreases with the increase of heat input except case of FR=20%. When the FR=40%, the liquid plug inside PHP needs smaller driving force to oscillate thus oscillates with higher velocity and amplitude than those with higher filling ratio accompanying by larger heat transfer capacity than the PHP at lower filling ratio.

For the FR=20% and FR= 60% cases, their thermal resistance is almost same when the heat input lower than 60W. When the heat input is higher than 60W, the thermal resistance of FR=60% is obvious higher than that of FR=20%. Therefore, the oscillation motion of working fluid is limited by the insufficient driving force when the heat input is lower than 60W for case of FR=60%. When the heat input is higher than 70 W, the boiling heat transfer in the evaporation section was intensive enough to make the working fluid oscillate well in the PHP and the heat was efficiently dissipated under this condition. Meanwhile, the “dry-out” phenomenon occurs at cases with 20% filling ratio and higher heat input. Although the FR=80% has the highest heat transfer capacity in this research, it shows the worst thermal performance compared with other filling ratio due to the restriction of smaller vapor phase space and higher driving force requirement.

The effect of various filling ratio on the PHP thermal resistance can be summarized as below. With the increase of filling ratio, more driving force is needed to make the working fluid oscillate in the PHP. It means that it is easier to realize the pulsating motion at the PHP with lower filling ratio under same heat input. However, the heat transfer capacity of working fluid decreases with decreasing filling ratio. Therefore, the overall influence of the filling ratio on thermal performance of PHP is the trade-off result between the required driving force and heat transfer capacity of the working fluid.

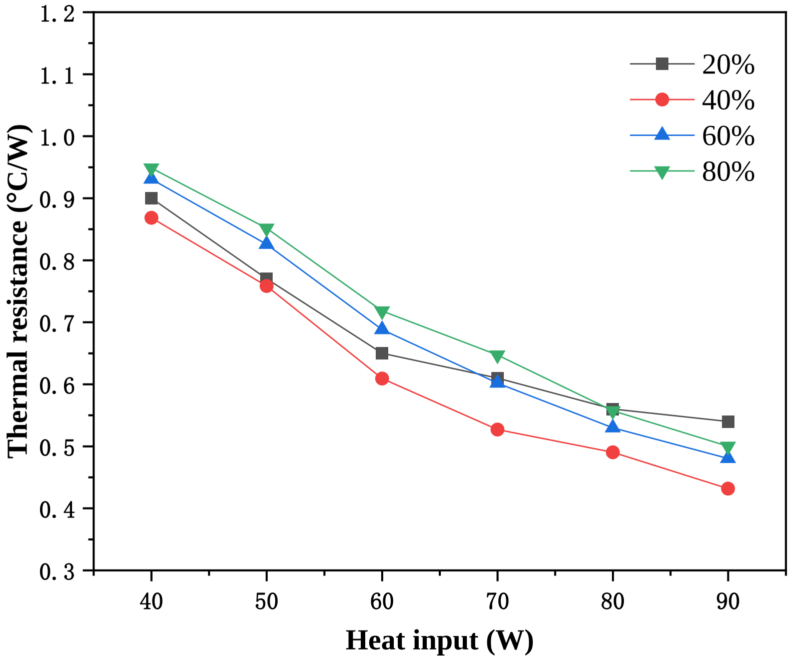
1.2
1.1
1.0
0.9
0.8
0.7
0.6
0.5
0.4
0.3
Thermal resistance (°C/W)
20%
40%
60%
80%
40
50
60
70
80
90
Heat input (W)
(a)

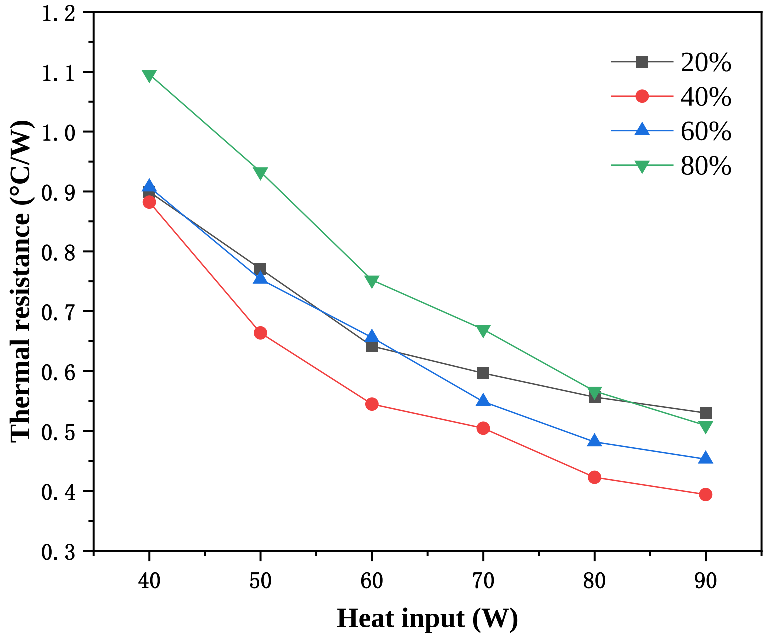
1. 2
1. 1
1. 0
0. 9
0. 8
0. 7
0. 6
0. 5
0. 4
0. 3
Thermal resistance (°C/W)
20%
40%
60%
80%
40
50
60
70
80
90
Heat input (W)

(b)

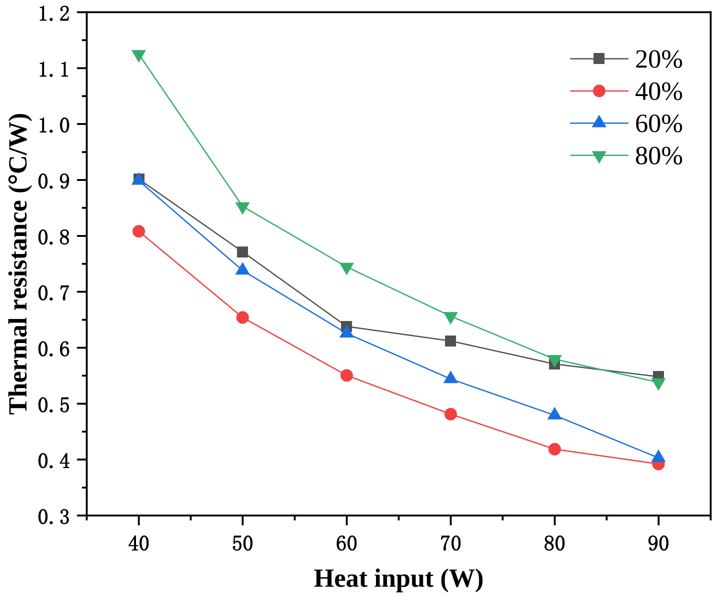
1. 2
1. 1
1. 0
0. 9
0. 8
0. 7
0. 6
0. 5
0. 4
0. 3
Thermal resistance (°C/W)
20%
40%
60%
80%
40
50
60
70
80
90
Heat input (W)

(c)

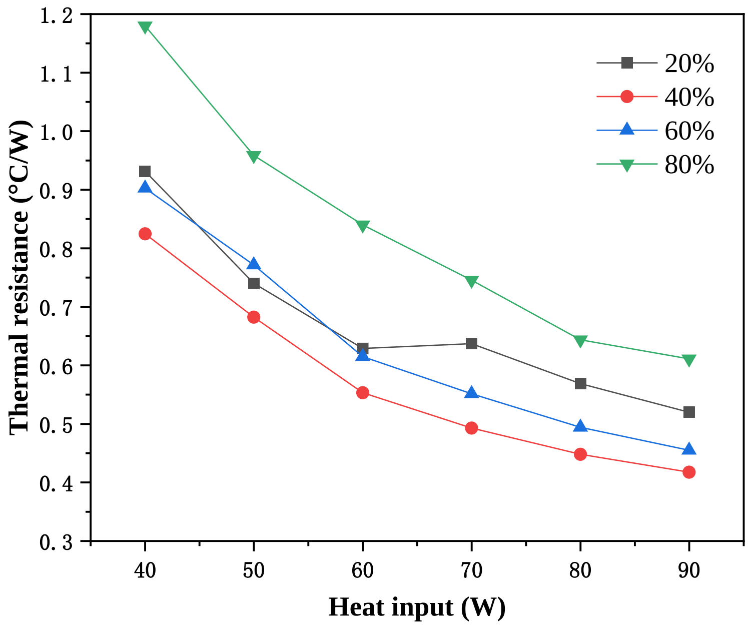

Thermal resistance (°C/W)
Heat input (W)
20%
40%
60%
80%

(d)

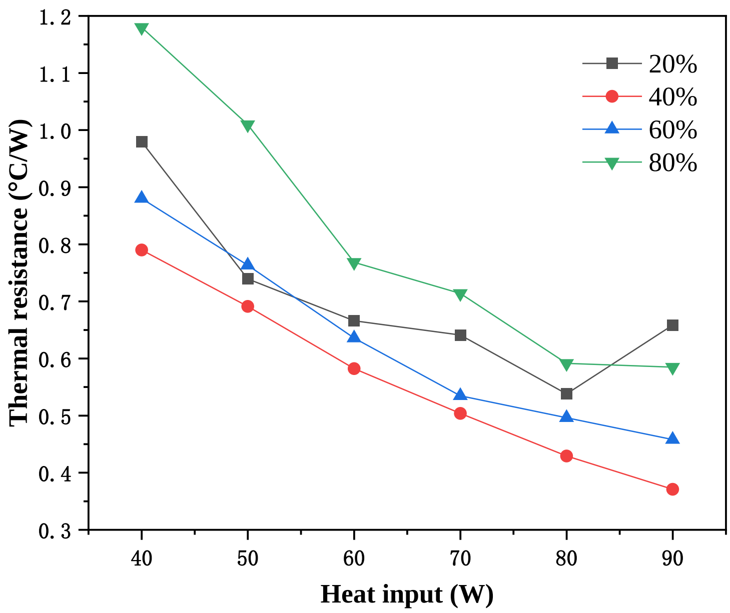

Thermal resistance (°C/W)
Heat input (W)
20%
40%
60%
80%

(e)

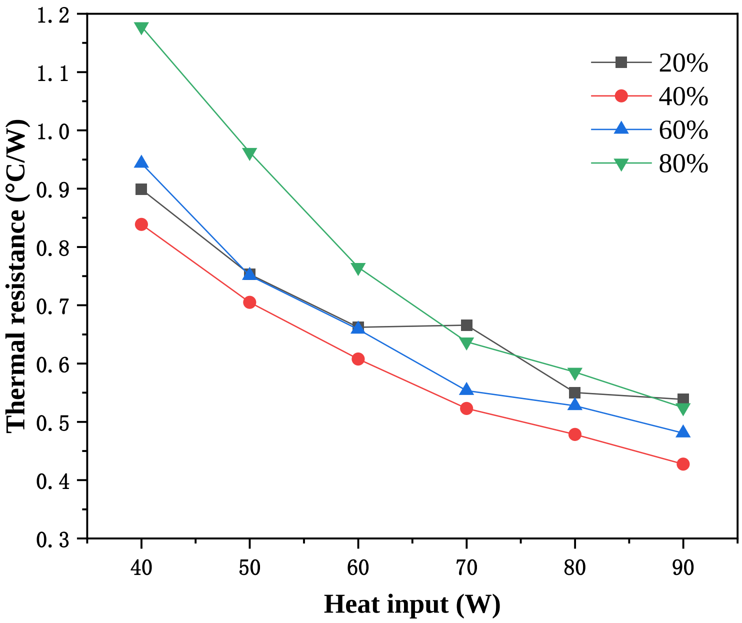

(f)

Figure 6-3 Thermal resistance at different filling ratio.(a) DI water; (b) 1 wt% MEPCM; (c) 2wt% MEPCM; (d) 3wt% MEPCM;(e)4wt% MEPCM;(f)5wt% MEPCM

6.6.2 Effect of the concentration of the MEPCMS on the PHP

This experimental study also focuses on the effects of concentrations of the MEPCM on the thermal performance of the PHP. Experiment was carried out with 0wt%, 1wt%, 2wt%, 3wt%, 4wt% and 5wt% of MEPCM suspension concentrations to observe the thermal performance of the PHP. The 0wt% represents the DI water in the experiment. The concentration of MEPCM suspension not only affects the heat transfer capacity of the PHP but also influence the viscosity of the working fluid. To show the effect of the concentration of the MEPCM suspension on the PHP thermal characteristics, the thermal resistance of PHP when the filling ratio were 20%, 40%, 60% and 80% are shown in Figure 6-11. Meanwhile, the viscosity of each working fluid is shown in section 6.4.3, the viscosity of working fluid increases with the concentration of MEPCM suspension. Therefore, higher concentration leads to higher viscosity which provides more friction force, in turn, hindering the motion of working fluid.

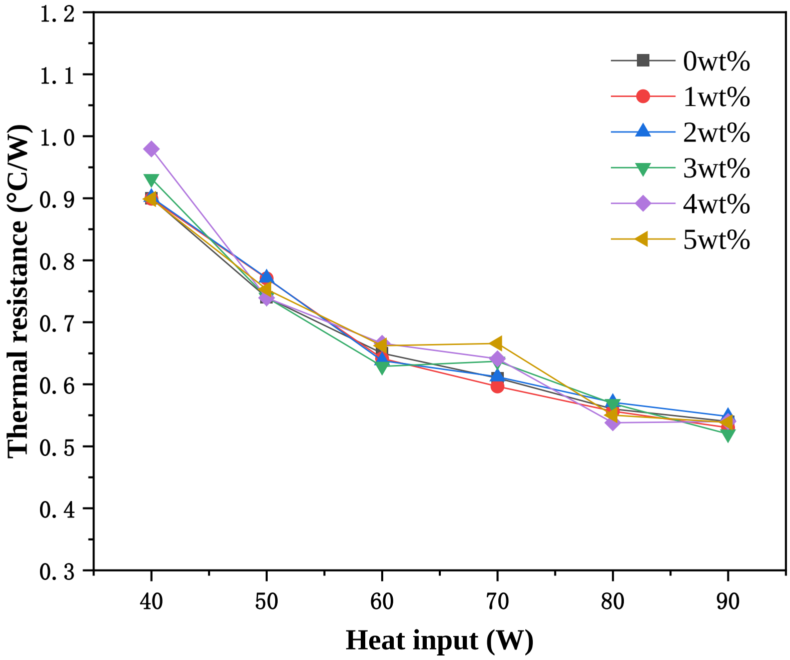

(a)

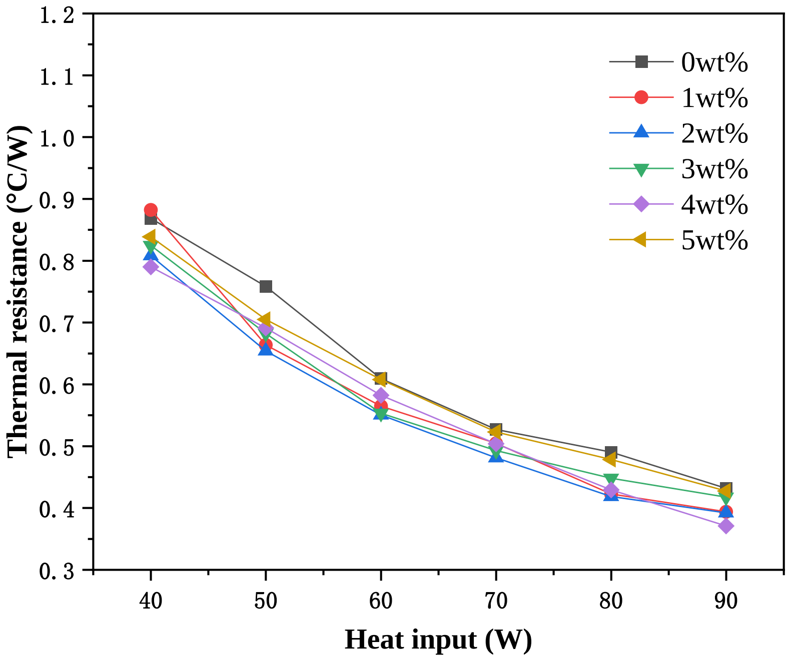

(b)

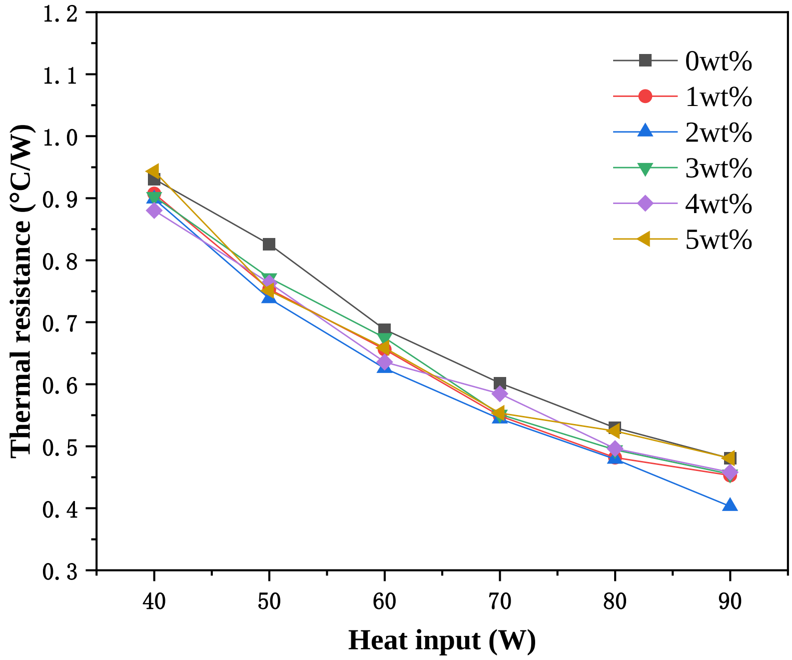

(c)

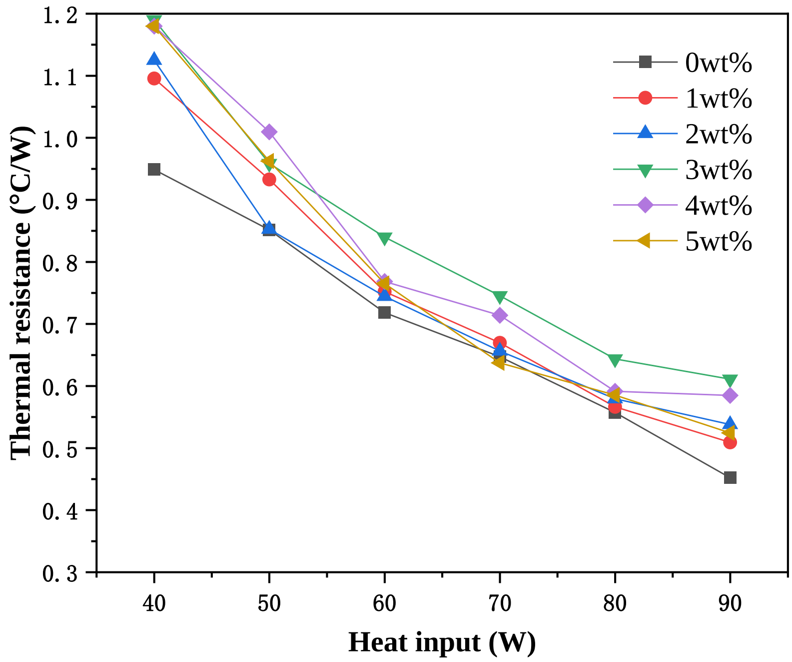

(d)

Figure 6-4 Thermal resistance of PHP at different concentration. (a)filling ratio=20% (b)filling ratio=40%; (c) filling ratio=60%; (d) filling ratio=80%

As Figure 6-11(a) shows, the concentration of the working fluid does not affect the thermal performance obviously at 20 % filling ratio. This attributed to the lower volume of working fluid due to the smaller liquid plug. When the filling ratio increases to 40% (Figure 6-11(b)), the influence of the concentration more obvious. The thermal resistance decreases rapidly when applied the MEPCM suspension. When the concentration equal to 2wt%, the PHP shows better thermal resistance than other concentration when the heat input is lower than 90W. This attributes to the relative smaller viscosity than the 3wt%, 4wt%, 5wt% suspension and higher heat transfer capacity than DI water and 1wt% suspension. With the increase of the heat input, the PHP with 4wt% solution shows better performance than the PHP with 2wt% solution, due to enough driving force supply which counteract the negative effect of the viscosity. In the case of FR=60% (Figure 6-14(c)), the thermal performance of PHP with lower concentration MEPCM suspension (1wt%, 2wt%) is better than those that with higher concentration and DI water. With the increase of heat input, the negative effect of the viscosity cannot be offset for the PHP with higher concentration MEPCM suspension(3wt%, 4wt%, 5wt%), because more driving force needed when the FR=60%. The PHP with higher concentration MEPCM suspension may shows better performance than those that with lower concentration if the heat input further increases. When the filling ratio achieves 80%, the thermal performance of PHP with DI water is higher than the PHP with MEPCM suspension at all heat input. The thermal performance of PHP decreases when applying the MEPCM suspension at 80% filling ratio compared to PHP with DI water due to much higher viscosity. In addition, the PHP failed to start-up when the concentration higher than 3wt% at 40W heat input. In this case, the heat input of evaporator section is not enough to push the liquid slugs to the condenser section. Therefore, the start-up time of PHP may be delayed, even fails to start-up when the PHP with high filling ratio and high concentration.

It could be found that the thermal performance of PHP can be enhanced by applying the MEPCM suspension in an optimal filling ratio and concentration. The experiment results can be explained as follows: the PHP with MEPCM suspension at 40% and 60% filling ratio showed better performance than the PHP with DI water mainly due to more sensible heat transferred to latent heat during the melting process of PCM and then dissipates at condenser section. However, the viscosity of the MEPCM suspension increases with the concentration, which increases the requirement of driving force to oscillate the working fluid. Besides, a relatively higher concentration of MPCM solution may hinders the start-up of PHP. Therefore, the overall influence of concentration of working fluid should consider the combined effect of the viscosity and heat transfer capacity of working fluid.

6.6.3 Summary

In this chapter, the thermal performance of the PHP with MEPCM suspension have been experimentally investigated. Meanwhile, the effects of filling and working fluid concentration also carried out in this chapter. The conclusions are shown as follow:

(1) The PHP has better thermal performance at optimum filling ratio 40% in this experiment. The filling ratio affects the heat transfer capacity of working fluid

and required driving force to make the pulsating motion of working fluid. For obtaining an optimum filling ratio, both effects of heat transfer capacity of working fluid and required driving force on thermal performance of PHP need to be considered.

(2) The thermal performance of PHP can be enhanced by using the MEPCM suspension with optimum concentration. The overall influence of the concentration of the working fluid is affected by the combined effect of the viscosity and heat transfer capacity of the working fluid.

(3) Compare with the PHP with DI water, the best thermal performance is 0.37°C/W when the filling ratio, heat input and the concentration of the MPCM were 40%, 90W and 4wt%, respectively.

Chapter 7 Conclusion and future work

7.1 Conclusions of current work

The presented thesis not only investigated the behaviours of droplets interaction with solid surfaces but also applied a novel working fluid to enhance the thermal performance of the PHP. Both experimental studies were carried out for each part. The main conclusions can be summarized as follows:

In Chapter 3 and Charter 4, two strategies for controlling the distribution of deposit patterns have been experimentally investigated. First, the effects of substrate roughness on deposit pattern are investigated. On the smooth surface, the contact angle of droplet increases as the roughness decreases. On the rough surface, the contact angle increases as the roughness increases. With contact angle decreasing, the evaporation rate at the boundary increases leading to the particles at the boundary easily sedimentate. Moreover, the capillary flow is hindered by increasing the substrate roughness, while the Marangoni flow remains constant, resulting in more particles remain in the centre of the droplet on the rough surface. To sum up, the coffee-ring formation is suppressed by increasing the substrate roughness on a copper substrate at 40 ˚C temperature. Second, an experiment is presented for controlling the deposit patterns with different substrate temperature ranging from 15 ˚C to 70 ˚C. The deposit patterns transit from uniformity, ring-like structure to dual ring patterns with substrate temperature increasing. The coffee ring shape easily forms at high temperature substrate, due to the outward flow is strengthen by increased substrate temperature. In addition, a secondary ring forms at gap area of the deposit pattern when the droplet evaporates at high temperature substrate, due to the collision between the Marangoni flow and outward flow when evaporation is almost completed.

In Chapter 5, the behaviours of droplets impacting on the conical structure with different surface roughness (125μm,21.8μm and 0.2μm) and cone angle (60°, 90° and 120°) were investigated experimentally. The effect of Weber number and the surface roughness and cone angle of conical structure are investigated in detail. The results show that the impacting droplet firstly spreads downwards along the side of the cone from the cone tip until it reaches its maximum spreading factor β_{max}. Subsequently, the rim of lamella starts to retract towards the cone tip and tend to form an annulus after reaching β_{max}. The droplet splashing can be observed at higher We(We=501). The β_{max} increases as the We increases and the increase in the surface roughness, and the increase in cone angle reduces β_{max}. The splashing can be promoted by increasing the surface roughness and cone angle, which is characterized by critical Weber number We_{cr} for the transition from spreading to splashing.

In Chapter 6, the thermal performance of PHP using MEPCM suspension were carried out. Experimental results show that the heat transfer performance of PHP can be enhanced by applying the MEPCM suspension dependent on the filling ratio and concentration of MEPCM suspension. With the increase of filling ratio, the heat transfer capacity of working fluid increases while increases the required driving force to make the pulsating motion of working fluid. The PHP with 40% filling ratio shows better thermal performance than those with other filling ratio in this experiment. For the concentration of MEPCM suspension, the heat transfer capacity of working fluid increases with increasing concentration. The increasing concentration of MEPCM suspension also increases the viscosity of working fluid which hinders the pulsating motion of working fluid. The overall influence of the concentration of the working fluid is affected by the combined effect of the viscosity and heat transfer capacity of the working fluid. In this experiment, the best thermal performance of PHP is $0.37\ ℃/W$ when the filling ratio, heat input and the concentration of the MEPCM suspension was 40%, 90W and 4wt%, respectively.

7.2 Suggestions for Future work

Apart from conducting an extensive investigation in the current study, new questions have arisen that need to be addressed in the future to fill the gap in the knowledge of pulsating heat pipe and droplet behaviours, which are recommended based on current work as follows:

- For droplet evaporation, more temperature points need to be investigated, for instance, 5°C and over 70°C. In this way, the effect of both Marangoni flow and Capillary flow on saline droplet will be more comprehensive understanding. The evaporation of different droplet also can be investigated such as nanofluids. The evaporation behaviours and deposition pattern of nanofluids droplet may be different from the saline droplets.
- In terms of droplet impingement on solid substrate, this thesis focuses on the effect of surface roughness, cone angle and Weber number. The impact behaviours are strongly affected by these factors. Different working fluid can be applied in the experiment, such as saline droplet and nanofluid. In addition, the droplet impact on heated cone substrate also need to study in the future, which is poor understanding and few study observe this situation at present.
- The present experimental studies the thermal performance of pulsating heat pipe adding the MEPCM suspension. Although the thermal performance of PHP enhances by adding the MEPCM suspension, the reason and mechanism are not well known. Therefore, more visualization study and numerical study need to conduct in the future to further reveal the interaction between the fluid in the PHP and MEPCM suspension.

Reference

[1] Soltman D, Subramanian V. Inkjet-printed line morphologies and temperature control of the coffee ring effect[J]. Langmuir, 2008, 24(5): 2224-2231.

[2] Yu Y, Zhu H, Frantz J M, et al. Evaporation and coverage area of pesticide droplets on hairy and waxy leaves[J]. biosystems engineering, 2009, 104(3): 324-334.

[3] Trantum J R, Baglia M L, Eagleton Z E, et al. Biosensor design based on Marangoni flow in an evaporating drop[J]. Lab on a Chip, 2014, 14(2): 315-324.

[4] Ramaswamy S, Golub T R. DNA microarrays in clinical oncology[J]. Journal of clinical oncology, 2002, 20(7): 1932-1941.

[5] Deegan R D. Pattern formation in drying drops[J]. Physical review E, 2000, 61(1): 475.

[6] Tripathy A, Sen P, Su B, et al. Advances in colloid and interface science[J]. Adv Colloid Interface Sci, 2017, 248: 85-104.

[7] Hu H, Larson R G. Evaporation of a sessile droplet on a substrate[J]. The Journal of Physical Chemistry B, 2002, 106(6): 1334-1344.

[8] Deegan R D, Bakajin O, Dupont T F, et al. Capillary flow as the cause of ring stains from dried liquid drops[J]. Nature, 1997, 389(6653): 827-829.

[9] Song M, Hu D, Zheng X, et al. Enhancing droplet deposition on wired and curved superhydrophobic leaves[J]. ACS nano, 2019, 13(7): 7966-7974

[10] Breitenbach J, Roisman I V, Tropea C. Heat transfer in the film boiling regime: Single drop impact and spray cooling[J]. International Journal of Heat and Mass Transfer, 2017, 110: 34-42.

[11] Zhang C, Kalulu M, Sun S, et al. Environmentally safe, durable and transparent superhydrophobic coating prepared by one-step spraying[J]. Colloids and Surfaces A: Physicochemical and Engineering Aspects, 2019, 570: 147-155.

[12] Zhang Y, Dong Z, Li C, et al. Continuous 3D printing from one single droplet[J]. Nature communications, 2020, 11(1): 1-10.

[13] A.M. Worthington, 1908. A Study of Splashes. London: Longmans, Green. 129 pp

[14] Rioboo R, Marengo M, Tropea C. Time evolution of liquid drop impact onto solid, dry surfaces[J]. Experiments in fluids, 2002, 33(1): 112-124.

[15] Good R J. Contact angle, wetting, and adhesion: a critical review[J]. Journal of adhesion science and technology, 1992, 6(12): 1269-1302.

[16] Chen X, Ma R, Li J, et al. Evaporation of droplets on superhydrophobic surfaces: Surface roughness and small droplet size effects[J]. Physical review letters, 2012, 109(11): 116101.

[17] Mangel Jr R F, Baer E. The evaporation of water drops from a “Teflon” surface[J]. Chemical Engineering Science, 1962, 17(9): 705-706.

[18] Brutin D, Starov V. Recent advances in droplet wetting and evaporation[J]. Chemical Society Reviews, 2018, 47(2): 558-585.

[19] López-Solís R, Salinas-Toro D, López D, et al. Stratification of tear components during tear microdesiccation on vertical glass surfaces: a novel approach in tear fluid assessment[J]. Cornea, 2015, 34(8): 959-966.

[20] Ravera F, Loglio G, Kovalchuk V I. Interfacial dilational rheology by oscillating bubble/drop methods[J]. Current Opinion in Colloid & Interface Science, 2010, 15(4): 217-228.

[21] Zang D, Tarafdar S, Tarasevich Y Y, et al. Evaporation of a Droplet: From physics to applications[J]. Physics Reports, 2019, 804: 1-56.

[22] Choi W, Tuteja A, Mabry J M, et al. A modified Cassie–Baxter relationship to explain contact angle hysteresis and anisotropy on non-wetting textured surfaces[J]. Journal of colloid and interface science, 2009, 339(1): 208-216.

[23] Moon J H, Cho M, Lee S H. Dynamic contact angle and liquid displacement of a droplet impinging on heated textured surfaces[J]. Experimental Thermal and Fluid Science, 2019, 101: 128-135.

[24] Song J W, Fan L W. Temperature dependence of the contact angle of water: a review of research progress, theoretical understanding, and implications for boiling heat transfer[J]. Advances in Colloid and Interface Science, 2021, 288: 102339.

[25] De Gennes P G. Wetting: statics and dynamics[J]. Reviews of modern physics, 1985, 57(3): 827.

[26] Ceyhan U, Tiktaş A, Özdoğan M. Pinning and depinning of Wenzel-state droplets around inclined steps[J]. Colloid and Interface Science Communications, 2020, 35: 100238.

[27] Lafuma A, Quéré D. Superhydrophobic states[J]. Nature materials, 2003, 2(7): 457-460.

[28] Ceyhan U, Tiktaş A, Özdoğan M. Pinning and depinning of Wenzel-state droplets around inclined steps[J]. Colloid and Interface Science Communications, 2020, 35: 100238.

[29] Lee J, Hwang S H, Yoon S S, et al. Evaporation characteristics of water droplets in Cassie, Wenzel, and mixed states on superhydrophobic pillared Si surface[J]. Colloids and Surfaces A: Physicochemical and Engineering Aspects, 2019, 562: 304-309.

[30] Ren H, Yang F, Li C, et al. Controllable dewetting transition on graphene based nanotextured surfaces[J]. Applied Surface Science, 2020, 520: 146374.

[31] Smyth K M. Wetting hysteresis and droplet roll off behaviour on superhydrophobic surfaces by Katherine Marie Smyth[D]. Massachusetts Institute of Technology, 2010.

[32] Picknett R G, Bexon R. The evaporation of sessile or pendant drops in still air[J]. Journal of colloid and Interface Science, 1977, 61(2): 336-350.

[33] Birdi K S, Vu D T. Wettability and the evaporation rates of fluids from solid surfaces[J]. Journal of adhesion science and technology, 1993, 7(6): 485-493.

[34] Rowan S M, Newton M I, McHale G. Evaporation of microdroplets and the wetting of solid surfaces[J]. The journal of physical chemistry, 1995, 99(35): 13268-13271.

[35] Erbil H Y, McHale G, Newton M I. Drop evaporation on solid surfaces: constant contact angle mode[J]. Langmuir, 2002, 18(7): 2636-2641.

[36] Shanahan M E R, Bourges C. Effects of evaporation on contact angles on polymer surfaces[J]. International journal of adhesion and adhesives, 1994, 14(3): 201-205.

[37] Gatapova E Y, Semenov A A, Zaitsev D V, et al. Evaporation of a sessile water drop on a heated surface with controlled wettability[J]. Colloids and Surfaces A: Physicochemical and Engineering Aspects, 2014, 441: 776-785.

[38] Lin T S, Zeng Y H, Tsay R Y, et al. Roughness-induced strong pinning for drops evaporating from polymeric surfaces[J]. Journal of the Taiwan Institute of Chemical Engineers, 2016, 62: 54-59.

[39] Camarinha Lopes M. The influence of substrate's elasticity and thermal properties on drop evaporation[J].

[40] Amini A, Homsy G M. Evaporation of liquid droplets on solid substrates. I. Flat substrate with pinned or moving contact line[J]. Physical Review Fluids, 2017, 2(4): 043603.

[41] Karpitschka S, Liebig F, Riegler H. Marangoni contraction of evaporating sessile droplets of binary mixtures[J]. Langmuir, 2017, 33(19): 4682-4687.

[42] Takhistov P, Chang H C. Complex stain morphologies[J]. Industrial & engineering chemistry research, 2002, 41(25): 6256-6269.

[43] Girard F, Antoni M, Sefiane K. Infrared thermography investigation of an evaporating sessile water droplet on heated substrates[J]. Langmuir, 2010, 26(7): 4576-4580.

[44] Kim H, Boulogne F, Um E, et al. Controlled uniform coating from the interplay of Marangoni flows and surface-adsorbed macromolecules[J]. Physical review letters, 2016, 116(12): 124501.

[45] Still T, Yunker P J, Yodh A G. Surfactant-induced Marangoni eddies alter the coffee-rings of evaporating colloidal drops[J]. Langmuir, 2012, 28(11): 4984-4988.

[46] Deegan R D, Bakajin O, Dupont T F, et al. Capillary flow as the cause of ring stains from dried liquid drops[J]. Nature, 1997, 389(6653): 827-829.

[47] Hu H, Larson R G. Marangoni effect reverses coffee-ring depositions[J]. The Journal of Physical Chemistry B, 2006, 110(14): 7090-7094.

[48] Zang D, Tarafdar S, Tarasevich Y Y, et al. Evaporation of a Droplet: From physics to applications[J]. Physics Reports, 2019, 804: 1-56.

[49] Thokchom A K, Zhou Q, Kim D J, et al. Characterizing self-assembly and deposition behaviour of nanoparticles in inkjet-printed evaporating droplets[J]. Sensors and Actuators B: Chemical, 2017, 252: 1063-1070.

[50] Uno K, Hayashi K, Hayashi T, et al. Particle adsorption in evaporating droplets of polymer latex dispersions on hydrophilic and hydrophobic surfaces[J]. Colloid and polymer science, 1998, 276(9): 810-815.

[51] Wu J, Xia J, Lei W, et al. Generation of the smallest coffee-ring structures by solute crystallization reaction on a hydrophobic surface[J]. RSC advances, 2013, 3(16): 5328-5331.

[52] Zhong X, Crivoi A, Duan F. Sessile nanofluid droplet drying[J]. Advances in colloid and interface science, 2015, 217: 13-30.

[53] Adachi E, Dimitrov A S, Nagayama K. Stripe patterns formed on a glass surface during droplet evaporation[J]. Langmuir, 1995, 11(4): 1057-1060.

[54] Moffat J R, Sefiane K, Shanahan M E R. Effect of TiO2 nanoparticles on contact line stick−slip behaviour of volatile drops[J]. The Journal of Physical Chemistry B, 2009, 113(26): 8860-8866.

[55] Gorr H M, Zueger J M, McAdams D R, et al. Salt-induced pattern formation in evaporating droplets of lysozyme solutions[J]. Colloids and Surfaces B: Biointerfaces, 2013, 103: 59-66.

[56] Yakhno T A, Kazakov V V, Sanina O A, et al. Drops of biological fluids drying on a hard substrate: Variation of the morphology, weight, temperature, and mechanical properties[J]. Technical Physics, 2010, 55(7): 929-935.

[57] Choudhury M D, Dutta T, Tarafdar S. Growth kinetics of NaCl crystals in a drying drop of gelatin: transition from faceted to dendritic growth[J]. Soft Matter, 2015, 11(35): 6938-6947.

[58] Buzoverya M E, Shcherbak Y P, Shishpor I V, et al. Microstructural analysis of biological fluids[J]. Technical physics, 2012, 57(7): 1019-1024.

[59] Buzoverya M E, Shcherbak Y P, Shishpor I V. Experimental investigation of the serum albumin fascia microstructure[J]. Technical Physics, 2012, 57(9): 1270-1276.

[60] Chen R, Zhang L, Zang D, et al. Wetting and drying of colloidal droplets: Physics and pattern formation[J]. Advances in Colloid Science, 2016: 3-25.

[61] Hu H, Larson R G. Analysis of the microfluid flow in an evaporating sessile droplet[J]. Langmuir, 2005, 21(9): 3963-3971.

[62] van Gaalen R T, Diddens C, Wijshoff H M A, et al. Marangoni circulation in evaporating droplets in the presence of soluble surfactants[J]. Journal of colloid and interface science, 2021, 584: 622-633.

[63] Still T, Yunker P J, Yodh A G. Surfactant-induced Marangoni eddies alter the coffee-rings of evaporating colloidal drops[J]. Langmuir, 2012, 28(11): 4984-4988.

[64] Sempels W, De Dier R, Mizuno H, et al. Auto-production of biosurfactants reverses the coffee ring effect in a bacterial system[J]. Nature communications, 2013, 4(1): 1-8.

[65] Seo C, Jang D, Chae J, et al. Altering the coffee-ring effect by adding a surfactant-like viscous polymer solution[J]. Scientific reports, 2017, 7(1): 1-9.

[66] Kajiya T, Kobayashi W, Okuzono T, et al. Controlling the drying and film formation processes of polymer solution droplets with addition of small amount of surfactants[J]. The Journal of Physical Chemistry B, 2009, 113(47): 15460-15466.

[67] Anyfantakis M, Geng Z, Morel M, et al. Modulation of the coffee-ring effect in particle/surfactant mixtures: the importance of particle–interface interactions[J]. Langmuir, 2015, 31(14): 4113-4120.

[68] Osman A, Shahidzadeh N, Stitt H, et al. Morphological transformations during drying of surfactant-nanofluid droplets[J]. Journal of Industrial and Engineering Chemistry, 2018, 67: 92-98. (2018) http://dx.doi.org/10.1016/j.jiec.2018.06.019.

[69] Sempels W, De Dier R, Mizuno H, et al. Auto-production of biosurfactants reverses the coffee ring effect in a bacterial system[J]. Nature communications, 2013, 4(1): 1-8.

[70] De Dier R, Sempels W, Hofkens J, et al. Thermocapillary fingering in surfactant-laden water droplets[J]. Langmuir, 2014, 30(44): 13338-13344.

[71] Kamyshny A, Ben‐Moshe M, Aviezer S, et al. Ink‐jet printing of metallic nanoparticles and microemulsions[J]. Macromolecular Rapid Communications, 2005, 26(4): 281-288..

[72] Small W R, Walton C D, Loos J, et al. Carbon nanotube network formation from evaporating sessile drops[J]. The Journal of Physical Chemistry B, 2006, 110(26): 13029-13036.

[73] Crivoi A, Duan F. Effect of surfactant on the drying patterns of graphite nanofluid droplets[J]. The Journal of Physical Chemistry B, 2013, 117(19): 5932-5938.

[74] Sefiane K. On the formation of regular patterns from drying droplets and their potential use for bio-medical applications[J]. Journal of Bionic Engineering, 2010, 7(4): S82-S93.

[75] Govor L V, Reiter G, Bauer G H, et al. Nanoparticle ring formation in evaporating micron-size droplets[J]. Applied physics letters, 2004, 84(23): 4774-4776.

[76] Brutin D. Influence of relative humidity and nano-particle concentration on pattern formation and evaporation rate of pinned drying drops of nanofluids[J].

Colloids and Surfaces A: Physicochemical and Engineering Aspects, 2013, 429: 112-120.

[77] Takhistov P, Chang H C. Complex stain morphologies[J]. Industrial & engineering chemistry research, 2002, 41(25): 6256-6269.

[78] Kočišová E, Petr M, Šípová H, et al. Drop coating deposition of a liposome suspension on surfaces with different wettabilities:"coffee ring" formation and suspension preconcentration[J]. Physical Chemistry Chemical Physics, 2017, 19(1): 388-393.

[79] Cuk T, Troian S M, Hong C M, et al. Using convective flow splitting for the direct printing of fine copper lines[J]. MRS Online Proceedings Library (OPL), 2000, 624.

[80] Eral H B, t Mannetje D, Oh J M. Contact angle hysteresis: a review of fundamentals and applications[J]. Colloid and polymer science, 2013, 291(2): 247-260.

[81] Li Y F, Sheng Y J, Tsao H K. Evaporation stains: suppressing the coffee ring effect by contact angle hysteresis[J]. Langmuir, 2013, 29(25): 7802-7811.

[82] Yang X, Li C Y, Sun Y. From multi-ring to spider web and radial spoke: competition between the receding contact line and particle deposition in a drying colloidal drop[J]. Soft Matter, 2014, 10(25): 4458-4463.

[83] Patil N D, Bange P G, Bhardwaj R, et al. Effects of substrate heating and wettability on evaporation dynamics and deposition patterns for a sessile water droplet containing colloidal particles[J]. Langmuir, 2016, 32(45): 11958-11972.

[84] Lee H H, Fu S C, Tso C Y, et al. Study of residue patterns of aqueous nanofluid droplets with different particle sizes and concentrations on different substrates[J]. International Journal of Heat and Mass Transfer, 2017, 105: 230-236.

[85] Askounis A, Sefiane K, Koutsos V, et al. The effect of evaporation kinetics on nanoparticle structuring within contact line deposits of volatile drops[J]. Colloids and Surfaces A: Physicochemical and Engineering Aspects, 2014, 441: 855-866.

[86] Brutin D. Influence of relative humidity and nano-particle concentration on pattern formation and evaporation rate of pinned drying drops of nanofluids[J]. Colloids and Surfaces A: Physicochemical and Engineering Aspects, 2013, 429: 112-120.

[87] Chhasatia V H, Joshi A S, Sun Y. Effect of relative humidity on contact angle and particle deposition morphology of an evaporating colloidal drop[J]. Applied Physics Letters, 2010, 97(23): 231909.

[88] Chon C H, Paik S, Tipton J B, et al. Effect of nanoparticle sizes and number densities on the evaporation and dryout characteristics for strongly pinned nanofluid droplets[J]. Langmuir, 2007, 23(6): 2953-2960.

[89] Jung J Y, Kim Y W, Yoo J Y. Behaviour of particles in an evaporating disperse colloid droplet on a hydrophilic surface[J]. Analytical chemistry, 2009, 81(19): 8256-8259.

[90] Thoroddsen S T, Etoh T G, Takehara K. High-speed imaging of drops and bubbles[J]. Annu. Rev. Fluid Mech., 2008, 40: 257-285.

[91] Joung Y S, Buie C R. Aerosol generation by raindrop impact on soil[J]. Nature communications, 2015, 6(1): 1-9.

[92] Rioboo R, Tropea C, Marengo M. Outcomes from a drop impact on solid surfaces[J]. Atomization and sprays, 2001, 11(2).

[93] Yang J, Long F, Wang R, et al. Design of mechanical robust superhydrophobic Cu coatings with excellent corrosion resistance and self cleaning performance inspired by lotus leaf[J]. Colloids and Surfaces A: Physicochemical and Engineering Aspects, 2021, 627: 127154.

[94] Shen Y, Wu X, Tao J, et al. Icephobic materials: Fundamentals, performance evaluation, and applications[J]. Progress in Materials Science, 2019, 103: 509-557.

[95] Zhu P, Wang Y, Chu H, et al. Superhydrophobicity preventing surface contamination as a novel strategy against COVID-19[J]. Journal of Colloid and Interface Science, 2021, 600: 613-619.

[96] Singh R K, Mandal D K. Air-assisted impact of water drops on a surface[J]. Acta Mechanica, 2019, 230(9): 3171-3182.

[97] Lin S, Zhao B, Zou S, et al. Impact of viscous droplets on different wettable surfaces: Impact phenomena, the maximum spreading factor, spreading time and post-impact oscillation[J]. Journal of colloid and interface science, 2018, 516: 86-97.

[98] Josserand C, Thoroddsen S T. Drop impact on a solid surface[J]. Annual review of fluid mechanics, 2016, 48(1): 365-391.

[99] Scheller B L, Bousfield D W. Newtonian drop impact with a solid surface[J]. AIChE Journal, 1995, 41(6): 1357-1367.

[100] Clanet C, Béguin C, Richard D, et al. Maximal deformation of an impacting drop[J]. Journal of Fluid Mechanics, 2004, 517: 199-208.

[101] Roisman I V, Berberović E, Tropea C. Inertia dominated drop collisions. I. On the universal flow in the lamella[J]. Physics of fluids, 2009, 21(5): 052103.

[102] Sen S, Vaikuntanathan V, Sivakumar D. Experimental investigation of biofuel drop impact on stainless steel surface[J]. Experimental thermal and fluid science, 2014, 54: 38-46.

[103]Thoroddsen S T, Sakakibara J. Evolution of the fingering pattern of an impacting drop[J]. Physics of fluids, 1998, 10(6): 1359-1374.

[104] Stow C D, Hadfield M G. An experimental investigation of fluid flow resulting from the impact of a water drop with an unyielding dry surface[J]. 158Proceedings of the Royal Society of London. A. Mathematical and Physical Sciences, 1981, 373(1755): 419-441.

[105] Mundo C H R, Sommerfeld M, Tropea C. Droplet-wall collisions: experimental studies of the deformation and breakup process[J]. International journal of multiphase flow, 1995, 21(2): 151-173.

[106] Range K, Feuillebois F. Influence of surface roughness on liquid drop impact[J]. Journal of colloid and interface science, 1998, 203(1): 16-30.

[107] Bird J C, Tsai S S H, Stone H A. Inclined to splash: triggering and inhibiting a splash with tangential velocity[J]. New Journal of Physics, 2009, 11(6): 063017.

[108] Wal R L V, Berger G M, Mozes S D. The splash/non-splash boundary upon a dry surface and thin fluid film[J]. Experiments in fluids, 2006, 40(1): 53-59.

[109] Xu L, Zhang W W, Nagel S R. Drop splashing on a dry smooth surface[J]. Physical review letters, 2005, 94(18): 184505.

[110] Stevens C S, Latka A, Nagel S R. Comparison of splashing in high-and low-viscosity liquids[J]. Physical Review E, 2014, 89(6): 063006.

[111] Moreira A L N, Moita A S, Panao M R. Advances and challenges in explaining fuel spray impingement: How much of single droplet impact research is useful?[J]. Progress in energy and combustion science, 2010, 36(5): 554-580.

[112] Marengo M, Antonini C, Roisman I V, et al. Drop collisions with simple and complex surfaces[J]. Current Opinion in Colloid & Interface Science, 2011, 16(4): 292-302.

[113] Roisman I V, Lembach A, Tropea C. Drop splashing induced by target roughness and porosity: The size plays no role[J]. Advances in colloid and interface science, 2015, 222: 615-621.

[114] Palacios J, Hernández J, Gómez P, et al. Experimental study of splashing patterns and the splashing/deposition threshold in drop impacts onto dry smooth solid surfaces[J]. Experimental Thermal and Fluid Science, 2013, 44: 571-582.

[115] Richard D, Clanet C, Quéré D. Contact time of a bouncing drop[J]. Nature, 2002, 417(6891): 811-811.

[116] Bird J C, Dhiman R, Kwon H M, et al. Reducing the contact time of a bouncing drop[J]. Nature, 2013, 503(7476): 385-388.

[117] Shen Y, Liu S, Zhu C, et al. Bouncing dynamics of impact droplets on the convex superhydrophobic surfaces[J]. Applied Physics Letters, 2017, 110(22): 221601.

[118] Hu Z, Ding S, Zhang X, et al. Dynamic behaviour and maximum width of impact droplets on single-pillar superhydrophobic surfaces[J]. Colloids and Surfaces A: Physicochemical and Engineering Aspects, 2022: 129355.

[119] Juarez G, Gastopoulos T, Zhang Y, et al. Splash control of drop impacts with geometric targets[J]. Physical Review E, 2012, 85(2): 026319.

[120]Bird J C, Dhiman R, Kwon H M, et al. Reducing the contact time of a bouncing drop[J]. Nature, 2013, 503(7476): 385-388.

[121] Luo J, Chu F, Ni Z, et al. Dynamics of droplet impacting on a cone[J]. Physics of Fluids, 2021, 33(11): 112116.

[122] Shen Y, Liu S, Zhu C, et al. Bouncing dynamics of impact droplets on the convex superhydrophobic surfaces[J]. Applied Physics Letters, 2017, 110(22): 221601.

[123] Liu X, Zhang X, Min J. Maximum spreading of droplets impacting spherical surfaces[J]. Physics of Fluids, 2019, 31(9): 092102.

[124] Chen S, Bertola V. Drop impact on spherical soft surfaces[J]. Physics of Fluids, 2017, 29(8): 082106.

[125] Luo J, Chu F, Ni Z, et al. Dynamics of droplet impacting on a cone[J]. Physics of Fluids, 2021, 33(11): 112116.

[126] Guo C, Sun J, Sun Y, et al. Droplet impact on cross-scale cylindrical superhydrophobic surfaces[J]. Applied Physics Letters, 2018, 112(26): 263702.161

[127] Andrew M, Liu Y, Yeomans J M. Variation of the contact time of droplets bouncing on cylindrical ridges with ridge size[J]. Langmuir, 2017, 33(30): 7583-7587.

[128] Stow C D, Hadfield M G. An experimental investigation of fluid flow resulting from the impact of a water drop with an unyielding dry surface[J]. Proceedings of the Royal Society of London. A. Mathematical and Physical Sciences, 1981, 373(1755): 419-441.

[129]Mundo, C., Sommerfeld, M., Tropea, C., 1995. Droplet-wall collisions: Experimental studies of the deformation and breakup process. Int. J. Multiph. Flow 21, 151 173. https://doi.org/10.1016/0301-9322(94)00069-V.

[130] Range K, Feuillebois F. Influence of surface roughness on liquid drop impact[J]. Journal of colloid and interface science, 1998, 203(1): 16-30.

[131] Cossali G E, Coghe A, Marengo M. The impact of a single drop on a wetted solid surface[J]. Experiments in fluids, 1997, 22(6): 463-472.

[132] Roisman I V, Lembach A, Tropea C. Drop splashing induced by target roughness and porosity: The size plays no role[J]. Advances in colloid and interface science, 2015, 222: 615-621.

[133] Quetzeri-Santiago M A, Castrejón-Pita A A, Castrejón-Pita J R. The effect of surface roughness on the contact line and splashing dynamics of impacting droplets[J]. Scientific reports, 2019, 9(1): 1-10.

[134] Tang C, Qin M, Weng X, et al. Dynamics of droplet impact on solid surface with different roughness[J]. International Journal of Multiphase Flow, 2017, 96: 56-69.

[135] Wang Q, Lin X, Lin Y, et al. Effects of surface roughness on splashing characteristics of large droplets with digital inline holographic imaging[J]. Cold Regions Science and Technology, 2021, 191: 103373.

[136] Xu Y, Xue Y, Qi H, et al. Experimental study on heat transfer performance of pulsating heat pipes with hybrid working fluids[J]. International Journal of Heat and Mass Transfer, 2020, 157: 119727.

[137] Li S F, Liu Z. Parametric study of rotating heat pipe performance: A review[J]. Renewable and Sustainable Energy Reviews, 2020, 117: 109482.

[138] Akachi H. Structure of heat pipe[J]. United States patent, Patent No. 4921041, 1990.

[139] Lu L, Liu Z H, Xiao H S. Thermal performance of an open thermosyphon using nanofluids for high-temperature evacuated tubular solar collectors: Part 1: Indoor experiment[J]. Solar energy, 2011, 85(2): 379-387.

[140] Clement J, Wang X. Experimental investigation of pulsating heat pipe performance with regard to fuel cell cooling application[J]. Applied Thermal Engineering, 2013, 50(1): 268-274.

[141] Dmitrin V I, Maidanik Y F, Pastukhov V G. Development and investigation of compact cooler using a pulsating heat pipe[J]. High Temperature, 2010, 48(4): 565-571.

[142] Torresin D, Agostini F, Mularczyk A, et al. Double condenser pulsating heat pipe cooler[J]. Applied Thermal Engineering, 2017, 126: 1051-1057.

[143] Faghri A. Review and advances in heat pipe science and technology[J]. Journal of heat transfer, 2012, 134(12).

[144] Takawale A, Abraham S, Sielaff A, et al. A comparative study of flow regimes and thermal performance between flat plate pulsating heat pipe and capillary tube pulsating heat pipe[J]. Applied Thermal Engineering, 2019, 149: 613-624.

[145] Khandekar S. Pulsating heat pipe based heat exchangers[C]//Proc. Of the 21st Int. Symposium on Transport Phenomena, Kaohsiung City, Taiwan. 2010: 2-5.

[146] Bastakoti D, Zhang H, Li D, et al. An overview on the developing trendof pulsating heat pipe and its performance[J]. Applied Thermal Engineering, 2018,141: 305-332.

[147] Pouryoussefi S M, Zhang Y. Analysis of chaotic flow in a 2D multi-turn closed-loop pulsating heat pipe[J]. Applied Thermal Engineering, 2017, 126: 1069-1076.

[148] Rahman M L, Nawrin S, Sultan R A, et al. Effect of fin and insert on the performance characteristics of close loop pulsating heat pipe (CLPHP)[J]. Procedia Engineering, 2015, 105: 129-136.

[149] Mameli M, Araneo L, Filippeschi S, et al. Thermal response of a closed loop pulsating heat pipe under a varying gravity force[J]. International Journal of Thermal Sciences, 2014, 80: 11-22.

[150] Akachi H, Polasek F, Stulc P. Pulsating heat pipes // Proceeding of 5 th international heat pipe symposium[J]. Melbourne, Australia, 1996.

[151] Charoensawan P, Terdtoon P. Thermal performance correlation of horizontal closed-loop oscillating heat pipes[C]//2007 9th Electronics Packaging Technology Conference. IEEE, 2007: 906-909.

[152] Wang J, Ma H, Zhu Q. Effects of the evaporator and condenser length on the performance of pulsating heat pipes[J]. Applied Thermal Engineering, 2015, 91: 1018-1025.

[153] Rahman M L, Saha P K, Mir F, et al. Experimental investigation on heat transfer characteristics of an Open Loop Pulsating Heat Pipe (OLPHP) with fin[J]. Procedia Engineering, 2015, 105: 113-120.

[154] Kim J, Kim S J. Experimental investigation on the effect of the condenser length on the thermal performance of a micro pulsating heat pipe[J]. Applied Thermal Engineering, 2018, 130: 439-448.

[155] Gamit H, More V, Mukund B, et al. Experimental investigations on pulsating heat pipe[J]. Energy Procedia, 2015, 75: 3186-3191.

[156] Rahman M L, Chowdhury M, Islam N A, et al. Effect of filling ratio and orientation on the thermal performance of closed loop pulsating heat pipe using ethanol[C]//AIP Conference Proceedings. AIP Publishing LLC, 2016, 1754(1): 050011.

[157] Bastakoti D, Zhang H, Cai W, et al. An experimental investigation of thermal performance of pulsating heat pipe with alcohols and surfactant

[158] Rahman M L, Afrose T, Tahmina H K, et al. Effect of using acetone and distilled water on the performance of open loop pulsating heat pipe (OLPHP) with different filling ratios[C]//AIP Conference Proceedings. AIP Publishing LLC, 2016, 1754(1): 050015.

[159] Kim J, Kim S J. Experimental investigation on working fluid selection in a micro pulsating heat pipe[J]. Energy Conversion and Management, 2020, 205: 112462.

[160] Hao T, Ma H, Ma X. Heat transfer performance of polytetrafluoroethylene oscillating heat pipe with water, ethanol, and acetone as working fluids[J]. International Journal of Heat and Mass Transfer, 2019, 131: 109-120.

[161] Kim B, Li L, Kim J, et al. A study on thermal performance of parallel connected pulsating heat pipe[J]. Applied Thermal Engineering, 2017, 126: 1063-1068.

[162] Miura M, Nagasaki T, Ito Y. Experimental investigation of heat transport with oscillating liquid column in pulsating heat pipe using forced oscillation system[J]. International Journal of Heat and Mass Transfer, 2017, 106: 997-1004.

[163] Xu R, Zhang C, Chen H, et al. Heat transfer performance of pulsating heat pipe with zeotropic immiscible binary mixtures[J]. International Journal of Heat and Mass Transfer, 2019, 137: 31-41.

[164] Zhu Y, Cui X, Han H, et al. The study on the difference of the start-up and heat-transfer performance of the pulsating heat pipe with water – acetone mixtures[J]. International Journal of Heat and Mass Transfer, 2014, 77: 834- 842.

[165] Xu Y, Xue Y, Qi H, et al. Experimental study on heat transfer performance of pulsating heat pipes with hybrid working fluids[J]. International Journal of Heat and Mass Transfer, 2020, 157: 119727.

[166] Nazari M A, Ghasempour R, Ahmadi M H, et al. Experimental investigation of graphene oxide nanofluid on heat transfer enhancement of pulsating heat pipe[J]. International Communications in Heat and Mass Transfer, 2018, 91: 90-94.

[167] Qu J, Wu H, Cheng P. Thermal performance of an oscillating heat pipe with Al2O3–water nanofluids[J]. International Communications in Heat and Mass Transfer, 2010, 37(2): 111-115.

[168] Patel V M, Mehta H B. Start up mechanism of pulsating heat pipe[C]//Proceedings of the national Conference on Thermal Fluid Science and Tribo Application TFSTA2016. 2017.

[169] Wang X H, Zheng H C, Si M Q, et al. Experimental investigation of the influence of surfactant on the heat transfer performance of pulsating heat pipe[J]. International Journal of Heat and Mass Transfer, 2015, 83: 586-590.

[170] Z.H Xue, W.Qu, international journal of heat and mass transfer 106(2017) 149-16

[171] Mehta B, Khandekar S. Taylor bubble-train flows and heat transfer in the context of pulsating heat pipes[J]. International Journal of Heat and Mass Transfer, 2014, 79: 279-290.

[172] Hosoda M, Nishio S, Shirakashi R. Meandering closed-loop heattransport tube (propagation phenomena of vapor plug)[R]. Univ. of Tokyo (JP), 1999.

[173] Sun Q, Qu J, Li X, et al. Experimental investigation of thermohydrodynamic behaviour in a closed loop oscillating heat pipe[J]. Experimental Thermal and Fluid Science, 2017, 82: 450-458.

[174] Senjaya R, Inoue T. Bubble generation in oscillating heat pipe[J]. Applied thermal engineering, 2013, 60(1-2): 251-255.

[175] Vo D T, Kim H T, Ko J, et al. An experiment and three-dimensional numerical simulation of pulsating heat pipes[J]. International Journal of Heat and Mass Transfer, 2020, 150: 119317.

[176] Kim W, Kim S J. Effect of a flow behaviour on the thermal performance of closed-loop and closed-end pulsating heat pipes[J]. International Journal of Heat and Mass Transfer, 2020, 149: 119251.

[177] Ahmad H, Kim S K, Jung S Y. Analysis of thermally driven flow behaviours for two-turn closed-loop pulsating heat pipe in ambient conditions: An experimental approach[J]. International Journal of Heat and Mass Transfer, 2020, 150: 119245.

[178] Patel V M, Mehta H B. Channel wise displacement-velocity-frequency analysis in acetone charged multi-turn Closed Loop Pulsating Heat Pipe[J]. Energy Conversion and Management, 2019, 195: 367-383.

[179] Xu R, Zhang C, Chen H, et al. Heat transfer performance of pulsating heat pipe with zeotropic immiscible binary mixtures[J]. International Journal of Heat and Mass Transfer, 2019, 137: 31-41.

[180] Gandomkar A, Kalan K, Vandadi M, et al. Investigation and visualization of surfactant effect on flow pattern and performance of pulsating heat pipe[J]. Journal of Thermal Analysis and Calorimetry, 2020, 139(3): 2099-2107.

[181] Zhang D, He Z, Guan J, et al. Heat transfer and flow visualization of pulsating heat pipe with silica nanofluid: An experimental study[J]. International Journal of Heat and Mass Transfer, 2022, 183: 122100.

[182] Gandomkar A, Saidi M H, Shafii M B, et al. Visualization and comparative investigations of pulsating ferro-fluid heat pipe[J]. Applied Thermal Engineering, 2017, 116: 56-65.

[183] Xu Y, Xue Y, Qi H, et al. An updated review on working fluids, operation mechanisms, and applications of pulsating heat pipes[J]. Renewable and Sustainable Energy Reviews, 2021, 144: 110995.

[184] Soltman D, Subramanian V. Inkjet-printed line morphologies and temperature control of the coffee ring effect[J]. Langmuir, 2008, 24(5): 2224-2231.

[185] Bhattacharya P, Samanta A N, Chakraborty S. Spray evaporative cooling to achieve ultra fast cooling in runout table[J]. International journal of thermal sciences, 2009, 48(9): 1741-1747.

[186] Zeng H, Kristiansen K, Wang P, et al. Surface-induced patterns from evaporating droplets of aqueous carbon nanotube dispersions[J]. Langmuir, 2011, 27(11): 7163-7167.

[187] Pirrung M C. How to make a DNA chip[J]. Angewandte Chemie International Edition, 2002, 41(8): 1276-1289.

[188] Parisse F, Allain C. Shape changes of colloidal suspension droplets during drying[J]. Journal de Physique II, 1996, 6(7): 1111-1119.

[189] Deegan R D, Bakajin O, Dupont T F, et al. Capillary flow as the cause of ring stains from dried liquid drops[J]. Nature, 1997, 389(6653): 827-829.

[190] Mampallil D, Eral H B. A review on suppression and utilization of the coffee-ring effect[J]. Advances in colloid and interface science, 2018, 252: 38-54.

[191] Parisse F, Allain C. Drying of colloidal suspension droplets: experimental study and profile renormalization[J]. Langmuir, 1997, 13(14): 3598-3602.

[192] Marin A G, Gelderblom H, Lohse D, et al. Order-to-disorder transition in ring-shaped colloidal stains[J]. Physical review letters, 2011, 107(8): 085502.

[193] Davis S H. Thermocapillary instabilities[J]. Annual Review of Fluid Mechanics, 1987, 19(1): 403-435.

[194] Hu H, Larson R G. Marangoni effect reverses coffee-ring depositions[J]. The Journal of Physical Chemistry B, 2006, 110(14): 7090-7094.

[195] Bhardwaj R, Fang X, Somasundaran P, et al. Self-assembly of colloidal particles from evaporating droplets: role of DLVO interactions and proposition of a phase diagram[J]. Langmuir, 2010, 26(11): 7833-7842.

[196] Yunker P J, Lohr M A, Still T, et al. Effects of particle shape on growth dynamics at edges of evaporating drops of colloidal suspensions[J]. Physical review letters, 2013, 110(3): 035501.

[197] Ristenpart W D, Kim P G, Domingues C, et al. Influence of substrate conductivity on circulation reversal in evaporating drops[J]. Physical review letters, 2007, 99(23): 234502.

[198] Kosmulski M. The pH-dependent surface charging and the points of zero charge[J]. Journal of Colloid and interface Science, 2002, 253(1): 77-87.

[199] Kim H, Boulogne F, Um E, et al. Controlled uniform coating from the interplay of Marangoni flows and surface-adsorbed macromolecules[J]. Physical review letters, 2016, 116(12): 124501.

[200] Mampallil D, Eral H B, Van Den Ende D, et al. Control of evaporating complex fluids through electrowetting[J]. Soft Matter, 2012, 8(41): 10614-10617.

[201] Chon C H, Paik S, Tipton J B, et al. Effect of nanoparticle sizes and number densities on the evaporation and dryout characteristics for strongly pinned nanofluid droplets[J]. Langmuir, 2007, 23(6): 2953-2960.

[202] Zhang Y, Chen X, Liu F, et al. Enhanced coffee-ring effect via substrate roughness in evaporation of colloidal droplets[J]. Advances in Condensed Matter Physics, 2018, 2018.

[203] Gong W, Yan Y, Chen S, et al. Numerical study of wetting transitions on biomimetic surfaces using a lattice Boltzmann approach with large density ratio[J]. Journal of Bionic Engineering, 2017, 14(3): 486-496.

[204] Zu Y Q, Yan Y Y, Li J Q, et al. Wetting behaviours of a single droplet on biomimetic micro structured surfaces[J]. Journal of Bionic Engineering, 2010, 7(2): 191-198.

[205] Bormashenko E, Musin A, Zinigrad M. Evaporation of droplets on strongly and weakly pinning surfaces and dynamics of the triple line[J]. Colloids and Surfaces A: Physicochemical and Engineering Aspects, 2011, 385(1-3): 235-240.

[206] Pittoni P G, Chang C C, Yu T S, et al. Evaporation of water drops on polymer surfaces: Pinning, depinning and dynamics of the triple line[J]. Colloids and Surfaces A: Physicochemical and Engineering Aspects, 2013, 432: 89-98.

[207] Li Y F, Sheng Y J, Tsao H K. Evaporation stains: suppressing the coffeering effect bycontact angle hysteresis[J]. Langmuir, 2013, 29(25): 7802-7811.

[208] Eral H B, t Mannetje D, Oh J M. Contact angle hysteresis: a review of fundamentals andapplications[J]. Colloid and polymer science, 2013, 291(2): 247-260.

[209] Kovalchuk N M, Trybala A, Starov V M. Evaporation of sessile droplets[J]. CurrentOpinion in Colloid & Interface Science, 2014, 19(4): 336-342.

[210] Pham T, Kumar S. Imbibition and evaporation of droplets of colloidal suspensions on permeable substrates[J]. Physical Review Fluids, 2019, 4(3): 034004.

[211] Pham T, Kumar S. Drying of droplets of colloidal suspensions on rough substrates[J]. Langmuir, 2017, 33(38): 10061-10076.

[212] Zhang Y, Qian Y, Liu Z, et al. Surface wrinkling and cracking dynamics in the drying of colloidal droplets[J]. The European Physical Journal E, 2014, 37(9): 1-7.

[213] Lohani D, Sarkar S. Nanoscale topographical fluctuations: A key factor for evaporative colloidal self-assembly[J]. Langmuir, 2018, 34(43): 12751-12758.

[214] Smith M I, Sharp J S. Effects of substrate constraint on crack pattern formation in thin films of colloidal polystyrene particles[J]. Langmuir, 2011, 27(13): 8009-8017.

[215] Krishna Darbha G, Fischer C, Michler A, et al. Deposition of latex colloids at rough mineral surfaces: An analogue study using nanopatterned surfaces[J]. Langmuir, 2012, 28(16): 6606-6617.

[216] Chen X, Ma R, Li J, et al. Evaporation of droplets on superhydrophobic surfaces: Surface roughness and small droplet size effects[J]. Physical review letters, 2012, 109(11): 116101.

[217] Worthington A M. XXVIII. On the forms assumed by drops of liquids falling vertically on a horizontal plate[J]. Proceedings of the royal society of London, 1877, 25(171-178): 261-272.

[218] Kim J. Spray cooling heat transfer: The state of the art[J]. International Journal of Heat and Fluid Flow, 2007, 28(4): 753-767.

[219] Kang C W, Ng H W. Splat morphology and spreading behaviour due to oblique impact of droplets onto substrates in plasma spray coating process[J]. Surface and Coatings Technology, 2006, 200(18-19): 5462-5477.

[220] Liang G, Mudawar I. Review of drop impact on heated walls[J]. International Journal of Heat and Mass Transfer, 2017, 106: 103-126.

[221] Hall D D, Mudawar I. Experimental and numerical study of quenching complex-shaped metallic alloys with multiple, overlapping sprays[J]. International journal of heat and mass transfer, 1995, 38(7): 1201-1216.

[222] Luxford G. Experimental and modelling investigation of the deformation, drag and break-up of drizzle droplets subjected to strong aerodynamics forces in relation to SLD aircraft icing[J]. 2005

[223] Pasandideh-Fard M, Qiao Y M, Chandra S, et al. Capillary effects during droplet impact on a solid surface[J]. Physics of fluids, 1996, 8(3): 650-659.

[224] Ukiwe C, Kwok D Y. On the maximum spreading diameter of impacting droplets on well-prepared solid surfaces[J]. Langmuir, 2005, 21(2): 666-673.

[225] Eggers J, Fontelos M A, Josserand C, et al. Drop dynamics after impact on a solid wall: theory and simulations[J]. Physics of fluids, 2010, 22(6): 062101.

[226] Silk E A, Kim J, Kiger K. Investigation of enhanced surface spray cooling[C]//ASME International Mechanical Engineering Congress and Exposition. 2004, 4711: 685-690.

[227] Sehmbey M S, Pais M R, Chow L C. Effect of surface material properties and surface characteristics inevaporative spray cooling[J]. Journal of thermophysics and heat transfer, 1992, 6(3): 505-512.

[228]Sharp, D. H. 1984 An overview of Rayleigh – Taylor instability, Physica 12D, 3 – 18.

[229]Clanet, Christophe, et al. "Maximal deformation of an impacting drop." Journal of Fluid Mechanics 517 (2004): 199-208.

[230]Roisman, Ilia V., Romain Rioboo, and Cameron Tropea. "Normal impact of a liquid drop on a dry surface: model for spreading and receding." Proceedings of the Royal Society of London. Series A: Mathematical, Physical and Engineering Sciences 458.2022 (2002): 1411-1430.

[231]Yarin, Alexander L. "Drop impact dynamics: splashing, spreading, receding, bouncing." Annual review of fluid mechanics 38.1 (2006): 159-192.

[232] Yonemoto Y, Yamashita M, Tashiro K, et al. Estimating the number of fingers and size of ejected droplets in droplet impingement processes on solid substrates[J]. Colloid and Interface Science Communications, 2022, 50: 100651.

[233]Hao, Ji guang. "Effect of surface roughness on droplet splashing." Physics of Fluids 29.12 (2017): 122105.

[234]Cui X, Qiu Z, Weng J, et al. Heat transfer performance of closed loop pulsating heat pipes with methanol-based binary mixtures[J]. Experimental Thermal and Fluid Science, 2016, 76: 253-263.

[235] Xu R, Zhang C, Chen H, et al. Heat transfer performance of pulsating heat pipe with zeotropic immiscible binary mixtures[J]. International Journal of Heat and Mass Transfer, 2019, 137: 31-41.

[236] Lin Y H, Kang S W, Chen H L. Effect of silver nano-fluid on pulsating heat pipe thermal performance[J]. Applied thermal engineering, 2008, 28(11-12): 1312-1317.

[237] Yang L, Xu J, Du K, et al. Recent developments on viscosity and thermal conductivity of nanofluids[J]. Powder Technology, 2017, 317: 348-369.

[238] Akilu S, Sharma K V, Baheta A T, et al. A review of thermophysical properties of water based composite nanofluids[J]. Renewable and Sustainable Energy Reviews, 2016, 66: 654-678.

[239] Wu L, Chen J, Wang S. Experimental study on thermal performance of a pulsating heat pipe using R1233zd (E) as working fluid[J]. International Communications in Heat and Mass Transfer, 2022, 135: 106152.

[240] Wang S, Lin Z, Zhang W, et al. Experimental study on pulsating heat pipe with functional thermal fluids[J]. International Journal of Heat and Mass Transfer, 2009, 52(21-22): 5276-5279.

[241] Li Q, Wang Y, Lian C, et al. Effect of micro encapsulated phase change material on the anti-dry-out ability of pulsating heat pipes[J]. Applied Thermal Engineering, 2019, 159: 113854.

[242] Heydarian R, Shafii M B, Rezaee Shirin-Abadi A, et al. Experimental investigation of paraffin nano-encapsulated phase change material on heat transfer enhancement of pulsating heat pipe[J]. Journal of Thermal Analysis and Calorimetry, 2019, 137(5): 1603-1613.

[243] Shi W, Chen H, Pan L, et al. Starting and running performance of a pulsating heat pipe with micro encapsulated phase change material suspension[J]. Applied Thermal Engineering, 2022, 212: 118626.

[244] Niu X, Xia R, Dong H, et al. Dispersion stability and thermophysical properties of microencapsulated phase change material slurry for liquid desiccant dehumidification[J]. Energy and Buildings, 2021, 240: 110870.

[245] Ma H B, Borgmeyer B, Cheng P, et al. Heat transport capability in an oscillating heat pipe[J]. 2008